

Simulating Arctic Mixed-Phase Clouds and their Sensitivity to Ice Nucleation

Diploma Thesis in Meteorology

Submitted by
Marco Paukert
in January 2013

Referee: Prof. Dr. C. Hoose
Second Examiner: Prof. Dr. T. Leisner

Simulation arktischer Mischphasenwolken und ihrer Sensitivität bezüglich der Eiskernung

Diplomarbeit im Fach Meteorologie vorgelegt von Marco Paukert

Referentin: Prof. Dr. C. Hoose

Korreferent: Prof. Dr. T. Leisner

Zusammenfassung

Anders als in nichtpolaren Gebieten ist der wolkeninduzierte bodennahe Netto-Strahlungsantrieb in der Arktis überwiegend durch den langwelligen Anteil der elektromagnetischen Strahlung bestimmt (Shupe und Intrieri, 2004). Weiterhin sind dort mit großer Auftretenswahrscheinlichkeit Stratocumulus-Schichten aus Eispartikeln oder als Mischwolken vorzufinden (Shupe et al., 2011; Shupe, 2011). Zusätzlich ist bekannt, dass die langwellige Strahlungsemission der Atmosphäre stark davon abhängt, ob und in welchem Maß Flüssigwasser in der Wolke vorhanden ist (z.B. Garrett und Zhao, 2006).

Für die Modellierung des atmosphärischen Zustands und der Auswirkungen auf den Erdboden ist es daher erstrebenswert, die korrekte Zusammensetzung einer Wolke aus Flüssigwasser und Eis simulieren zu können. Ziel dieser Arbeit ist deshalb, die heterogene Eiskondensation in einer arktischen Mischwolke zu untersuchen und die Parametrisierung im verwendeten COSMO-Modell (CONsortium for Small-scale MOdeling) zu erweitern. Die Datengrundlage für die durchgeführten Simulationen bildet der Messflug 31 vom 26. April 2008, der im Rahmen der ISDAC-Kampagne (Indirect and Semi-Direct Aerosol Campaign) im Norden Alaskas durchgeführt wurde.

Der erste Schritt dieser Arbeit war die Teilnahme an einem Modell-Vergleich unter Verwendung der erweiterten COSMO-Version COSMO-ART (Vogel et al., 2009) mit Zweimomenten-Formulierung der wolkenmikrophysikalischen Vorgänge (Seifert und Beheng, 2006). Die hier verwendete Konfiguration gleicht einem LES-Modell (Large Eddy Simulation), um die kleinskaligen Prozesse erfassen zu können, wodurch insbesondere die Vertikalbewegungen innerhalb der Wolke aufgelöst werden. Zusätzlich wurde ein Strahlungsschema implementiert, welches die thermische Abkühlrate der Wolke als Funktion des vertikal integrierten Flüssigwassergehalts berechnet. Da die Parameter des Schemas auf Grundlage der Messungen angepasst sind, wird angenommen, dass hiermit die vorliegende Situation besser erfasst wird als unter Verwendung des COSMO-Strahlungsschemas, welches ca. doppelt so hohe Abkühlraten ausgibt. Weiterhin wurden einige mikrophysikalische Parameter angepasst, um einerseits die Wolkenpartikeleigenschaften für den gegebenen Fall zu optimieren, und um andererseits konsistente Formulierungen unter den am Vergleich teilnehmenden Modellen herzustellen.

Die Ergebnisse im Vergleich zu weiteren Modellen zeigen, dass COSMO die Situation gut genug erfassen kann, um in dieser Konfiguration weitere Untersuchungen zu erlauben. Es traten Unterschiede in der Aufteilung des Gesamtwassergehalts zwischen der festen und der flüssigen Phase auf, welche umso größer waren, je mehr Eiskristalle innerhalb der Schichtwolke existierten. Dieser Unterschied konnte auf unterschiedliche Annahmen über die Form der Eispartikel-Größenverteilung zurückgeführt werden, da den Parametern der Verteilungsdichtefunktionen in einer Zweimomenten-Formulierung kon-

stante Werte zugewiesen werden, welche sich zwischen den Modellen unterscheiden. Ein Spezifikum von COSMO, dessen Ursachenfindung noch weiterer Arbeit bedarf, sind die generell kleineren erreichten maximalen Vertikalgeschwindigkeiten. Diese haben über Rückkopplungsmechanismen sowohl weniger Flüssigwasser- als auch Eisgehalt zur Folge. Da COSMO in seiner vorwiegenden Funktion als Wettervorhersagemodell auf größeren Skalen optimiert ist, können Unterschiede in der Turbulenzparametrisierung und in numerischen Behandlungen als mögliche Ursachen in Betracht gezogen werden.

Im zweiten Teil der Arbeit stand die heterogene Eisnukleation innerhalb der Wolke im Mittelpunkt. Statt wie im Rahmen des Modellvergleichs eine konstante Eiskristall-Anzahldichte vorzuschreiben, wurde nunmehr die Auswirkung von verschiedenen Parametrisierungen auf die zeitliche Entwicklung der Wolke analysiert. Der einzig aktive Mechanismus war hierfür das Immersionsgefrieren von Mineralstaub und Bakterien.

Zuerst erfolgte eine Erweiterung des Modells, welche das mehrfache Gefrieren einzelner Eiskeime verhindert. Hierfür diente eine zusätzliche prognostische Variable, die aktivierte Eiskeime repräsentiert. Neben der Nukleation, die den Quellterm bildet, unterliegt die Variable dem Transport durch Advektion und turbulente Diffusion, welche in der vorliegenden Stratocumulus-Wolke insbesondere für die vertikale Durchmischung der Eiskeime von Bedeutung sind. Diese Durchmischung stellt sicher, dass die Eisneubildung dauerhaft aufrecht erhalten werden kann. Im Gegensatz zur Behandlung im unveränderten Nukleationsschema, bei dem die Anzahldichte aktivierter Eiskeime mit den vorhandenen Eispartikeln gleichgesetzt wird, ergeben sich mit der zusätzlichen Variable generell geringere Eispartikel-Anzahlkonzentrationen unter sonst gleichen Bedingungen. Dieser Unterschied ergibt sich aus dem Effekt der Eiskristall-Sedimentation, welcher im Originalschema aufgrund der Divergenz des Sedimentationsflusses in den obersten Wolkenschichten zu einer kontinuierlichen Eisneubildung führt, da in diesem Schema eine direkte Kopplung zwischen den beiden Prozessen besteht. Dies ist der Grund dafür, dass sich die Wolke unter Verwendung des Originalschemas bei kleineren Aerosolkonzentrationen auflöst als mit der Modellerweiterung, weil höhere Eiskristall-Konzentrationen einen effektiveren Wegener-Bergeron-Findeisen-Prozess zur Folge haben. Demzufolge wird mehr Flüssigwasser zugunsten der Eisphase aufgezehrt, was bei dieser Wolkenart die turbulenten Bewegungen schwächt, und überhalb einer kritischen Eiskonzentration ganz zum Erliegen bringt. In einer solchen Situation ist auch die Neubildung von Flüssigtröpfchen ausgeschlossen, sodass nach dem Sedimentieren der verbliebenen Eiskristalle die Wolke ganz verschwindet.

Aufbauend auf der Singulären Hypothese, die die heterogene Nukleation als zeitunabhängiges, instantanes Ereignis beschreibt, wurden zwei Parametrisierungen in COSMO implementiert, um das Immersionsgefrieren von natürlichem Mineralstaub und eisnukleations-aktiver Bakterien auf die vorliegende Situation anzuwenden. Beide werden nach dem Ansatz von eisnukleations-aktiven Stellen berechnet, die sich auf der Oberfläche von Aerosolen in einer bestimmten Dichte bezüglich der Fläche befinden (engl. "ice nucleation active surface site density"). Eine Reihe von Sensitivitätsstudien mit verschiedenen Kombinationen aus Mineralstaub- und Bakterien-Eiskeimkonzentrationen führte zu einer Abschätzung,

welche Konzentrationen benötigt würden, um unter den gegebenen Bedingungen eine zeitlich stabile Wolke zu erlangen. Diese Bedingung wurde zurückgeführt auf den zeitlichen Verlauf von vertikal integriertem Flüssigwasser- und Eisgehalt. Da bei wenigen Eiskristallen die Wolkenschicht in ihrer vertikalen Ausdehnung wächst und bei vielen Eiskristallen in ihrer Ausdehnung abnimmt, gibt es nur einen bestimmten Bereich von Aerosolkonzentrationen, der die Stabilitätsbedingung erfüllt.

Generell sind die benötigten Aerosolkonzentrationen im "stabilen" Bereich höher als die abgeschätzten Basiskonzentrationen von Mineralstaub und Bakterien, wobei der Unterschied mehrere Größenordnungen betragen kann. Um die während ISDAC beobachteten Eiskristall-Anzahldichten zu erklären, muss daher in Betracht gezogen werden, ob es im simulierten Fall weitere relevante Eiskeim-Spezies gibt und welche Rolle zusätzliche Nukleations-Mechanismen neben dem Immersionsgefrieren spielen.

Contents

1	Introduction	1
1.1	Radiative Forcing of Arctic Boundary Layer Clouds	1
1.2	Modeling Efforts	4
1.3	Objective	6
2	From Physical Processes to Parameterizations	7
2.1	Formation of Ice Crystals	7
2.1.1	The Stochastic Process of Homogeneous Freezing	7
2.1.2	The Singular Hypothesis for Heterogeneous Nucleation	9
2.1.3	Distinction Between Heterogeneous Ice Nucleation Modes	12
2.1.4	Cloud Microphysics and Ice Nucleation in COSMO	13
2.2	Model Extensions for Ice Nucleation	19
2.2.1	Immersion Freezing of Dust Particles: Niemand et al. (2012)	19
2.2.2	Immersion Freezing of Bacteria	20
2.2.3	IN Depletion due to Activation	23
2.2.4	Threshold for Immersion Freezing	27
2.3	Further Important Model Details	28
2.3.1	Depositional Growth of Ice Crystals in the Presence of Supercooled Water	28
2.3.2	Sedimentation	32
2.3.3	Cloud Top Radiative Cooling	33
3	COSMO's Performance in a Cloud Resolving Configuration	37
3.1	Model Setup for LES Simulations	37
3.1.1	Model Domain, Boundary Conditions and Initialization	38
3.2	Results of COSMO	42
3.2.1	Development of a Liquid-Only-Cloud: "Ice0"	42
3.2.2	Development of a Mixed-Phase Cloud: "Ice1", "Ice4"	44
3.3	Discussion of Results in the Context of the Model Intercomparison	46
3.3.1	Liquid Water Dissipation	46
3.3.2	Vertical Velocities	50
3.3.3	Relative Importance of Vertical Velocities and WBF	52

4	Sensitivity to the Treatment of Ice Nucleation	55
4.1	Concentrations Applied for Sensitivity Tests	55
4.2	Model setup	58
4.3	Treatment of Ice Initialization	59
4.4	Comparison of Default Nucleation Scheme and IN Depletion Scheme	61
4.5	Depleted Ice Nuclei with and without Transport	64
4.6	Comparison of Phillips et al. (2008) and Niemand et al. (2012)	66
4.7	Dust vs. Bacteria as IN species	69
4.8	Dust vs. Bacteria at Colder Temperatures	74
4.9	Sensitivity to Cloud Top Radiative Cooling	78
5	Summary and Outlook	81
6	List of Model Settings, Acronyms and Symbols	85
A	Bibliography	89

1. Introduction

In the Earth's atmosphere, clouds play multiple roles. They occur in different shapes, at different altitudes with varying vertical extents, in different temperature regimes, consisting either of water in the liquid phase, of ice, or of both concurrently. Various shapes and sizes of cloud particles are possible, ranging from some micrometers up to millimeters for liquid droplets and an even larger range exists for ice particles. Their shapes comprise dendritic crystals with low density to highly dense spheres and irregular-shaped hail stones with diameters possibly reaching more than 10cm (Pruppacher and Klett, 1997). Thus, it can be expected that clouds' properties can differ considerably among the various types.

1.1. Radiative Forcing of Arctic Boundary Layer Clouds

One of the clouds' interesting properties is their ability to modify the radiation budget on the ground. In general, clouds make opposing contributions to surface temperatures. On the one hand, downwelling solar radiation is reflected backwards into space. On the other hand, the earth itself emits longwave radiation which can be absorbed by clouds. According to Kirchhoff's law, longwave absorption simultaneously results in longwave emission, which in turn is absorbed by the ground, leading to a weakened surface cooling. It is therefore interesting which one of both effects weighs more - warming or cooling. However, each cloud type behaves specifically in this question.

In order to quantify the effect on surface temperatures, the surface cloud radiative forcing, CF , can be applied (e.g. Shupe and Intrieri, 2004). It is the difference between all-sky and clear-sky net surface radiative fluxes, consisting of a longwave contribution CF_{LW} and a shortwave contribution CF_{SW} . Therefore, positive values correspond to a net surface warming.

Low-level stratus and stratocumulus often cover large areas, especially over subtropical oceans (Twohy et al., 2005). Residing at low altitudes, their temperature difference relative to the ground is not very high. Therefore, their modification of the net surface longwave radiation budget is only small. Furthermore, they are optically thick with high shortwave albedo, reflecting much of the insolation. This effect is particularly high over dark oceans which have a low albedo. All in all, the effect of marine stratocumulus clouds is a net cooling of the surface with dominating negative values of CF_{SW} .

Compared to lower latitudes, Arctic regions were found to behave differently. In polar regions, the longwave forcing dominates in most periods of the year (Shupe and Intrieri, 2004), which can be related to two aspects. First, the solar zenith angle is generally high, causing low shortwave radiative flux densities. Second, the bright surface reduces the sensitivity to insolation additionally.

Shupe and Intrieri (2004), whose findings are based on the SHEBA campaign found that the shortwave radiative cloud forcing was only dominant for some weeks during the whole year, corresponding to the period of the lowest zenith angles. Analyzing the effect of liquid-containing clouds, the annual mean values for the same campaign calculated by Intrieri et al. (2002) were $CF_{LW} = +38 \frac{W}{m^2}$ for the longwave cloud forcing and $CF_{SW} = -9 \frac{W}{m^2}$ for the shortwave cloud forcing, respectively. Hence, a net warming effect was found.

Based on the Stefan-Boltzmann law, the thermal emission flux of a cloud can be characterized by the relation

$$F_{LW} = \left(1 - e^{-k \cdot LWP}\right) \sigma_{SB} T_c^4, \quad [1.1]$$

depending on the liquid water path (LWP), a representative cloud temperature T_c and a factor k which includes the information on the cloud droplet size and wave length (Garrett and Zhao, 2006). σ_{SB} is the Stefan-Boltzmann constant. Therefore, the cloud is a grey body with an emissivity less than one. With increasing LWP, the prefactor approaches unity, causing the cloud to emit like a black body. This implies that the cloud is sensitive to changes in LWP only below a threshold value.

Sun and Shine (1994) point out the importance of distinguishing between the water phases to calculate the radiation transfer of mixed-phase clouds, whereas equation 1.1 states the radiation flux to be dependent on liquid water only, neglecting contributions of ice. A detailed analysis of observational data was done by Shupe and Intrieri (2004), deriving the longwave radiation cloud forcing for clouds containing liquid water and ice-only clouds. It was shown that the cloud phase is a determining factor. Annual mean values are given as $+52 \frac{W}{m^2}$ for liquid-containing clouds and $+16 \frac{W}{m^2}$ for ice-only clouds with an estimated uncertainty of $6 \frac{W}{m^2}$. Hence, the total surface cloud forcing is mostly determined by the presence of liquid water, which is additionally supported by a 10 day analysis of SHEBA data by Zuidema et al. (2005). They report a time-mean positive net cloud forcing of $41 \frac{W}{m^2}$ primarily due to optically thick clouds.

Owing to the importance of liquid water, eq. 1.1 is especially interesting for Arctic conditions, since Arctic stratus clouds are either supercooled mixed-phase layers or ice-only clouds. Since their LWPs are generally low and the two states may change between each other quickly (e.g. Morrison et al., 2011a), these clouds' influence on CF is particularly high. Based on the SHEBA experiment, Shupe and Intrieri (2004) found the "critical" value of the LWP to be $30 gm^{-2}$, below which the clouds' CF_{LW} showed significant sensitivity to the LWP. Their analyses show a probability density function for the LWP to be highest within this critical range and generally lower LWPs during winter. Also the LWPs found in the Arctic Stratus Experiment in the Beaufort Sea during June 1980 (Herman and Curry, 1984; Curry, 1986; Tsay and Jayaweera, 1984) covered a range from $11 gm^{-2}$ to $117 gm^{-2}$ for low clouds and from $7 gm^{-2}$ to $15 gm^{-2}$ for middle clouds (Curry et al., 1996).

Another aspect that increases the effectiveness of the longwave radiation forcing in the Arctic is given by the low amount of water vapor relative to midlatitudes. Because the dry atmosphere yields low

CF_{LW} for clear-sky conditions, the difference between clear-sky and a sky covered with liquid-containing clouds is particularly high in the Arctic (Shupe and Intrieri, 2004).

Significant contributions to long term mean values of CF_{LW} can only be made by clouds with high frequencies of occurrence. Shupe et al. (2011) and Shupe (2011) found high percentages of liquid-containing clouds when analyzing ground-based observational data collected at six sites (fig. 1.1). The persistence was longer than 100 hours for 5% of all cloud systems. The most persistent 5% of the liquid clouds were able to remain 30 to 70 hours, depending on the season. Furthermore, Shupe (2011) finds that liquid water occurs during 56% of the time at Barrow and during SHEBA.

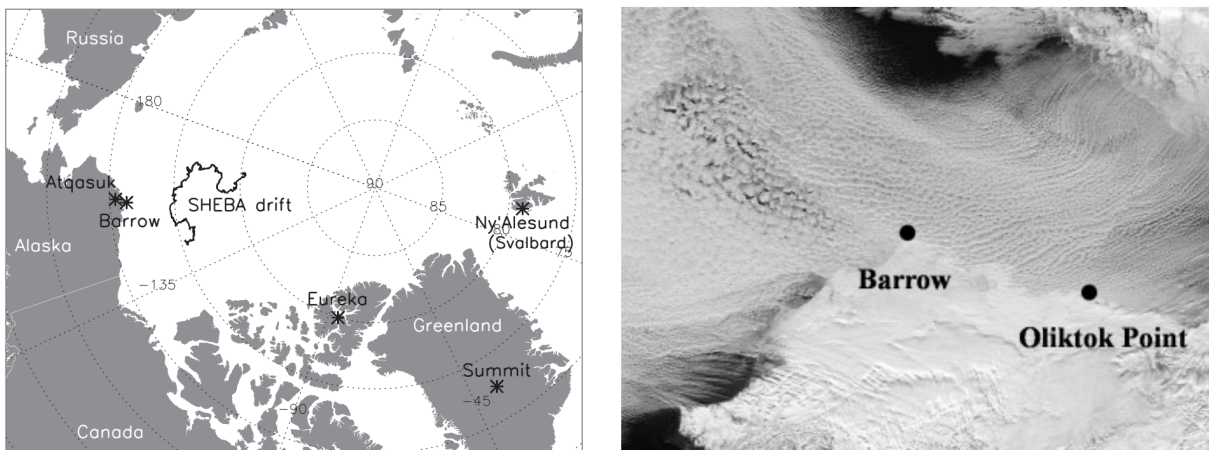


Fig. 1.1.: Left: Map of the Arctic region with measurement sites analyzed by Shupe et al. (2011). Barrow is the location of the ISDAC campaign, on which the simulations of this work are based (see section 1.3). Right: Satellite image of clouds observed during M-PACE on 8 October 2004 (Klein et al., 2009), when north-easterly flow comes from the sea (upper right corner) ice towards the open ocean.

1.2. Modeling Efforts

Due to the high sensitivity of surface temperatures to thin liquid-containing layer clouds, with high frequencies of occurrence of the relevant conditions in nature, there is a need to correctly represent these clouds in models (e.g. Morrison et al., 2011a; Shupe and Intrieri, 2004; Curry et al., 1996). Only this enables them to simulate temperatures on longer timescales correctly, so that it is possible to draw conclusions on the development of Arctic climate.

Based on the SHEBA measurements, Morrison et al. (2011a) estimate that only a 5% shift in a modeled frequency of occurrence could result in a bias of the net surface longwave radiation budget as much as 1.5 to $2.0 \frac{W}{m^2}$, since differences between the ice-only and mixed-phase state typically accounted for 30 to $40 \frac{W}{m^2}$.

As candidates responsible for discrepancies in large scale models, Randall et al. (1998) point out the sea-ice submodels as well as the parameterized cloud physics and boundary layer processes. To evaluate models, some intercomparison studies of general circulation models exist (e.g. Tao et al., 1996; Chen et al., 1995; Walsh et al., 2002), pointing at a lacking accuracy in the cloud-radiation relationship (Shupe and Intrieri, 2004).

Hence, efforts were made to improve the data basis of Arctic measurements. Besides the possibility to learn about basic processes, the measurement campaigns provided data needed to drive and evaluate models on several scales, from the local scale up to the global scale.

A campaign extensively used as data basis is the Surface Heat Budget of the Arctic Ocean (SHEBA) program from October 1997 to October 1998 (Uttal et al., 2002). For one whole year, a ship was drifting along with the pack ice movements passively to gain data (see fig. 1.1). In spring 1998 from April to July, these measurements were combined with data gained by aircraft measurements in the frame of the First ISCCP Regional Experiment Arctic Clouds Experiment (FIRE-ACE), providing even more detailed data (Curry et al., 2000) which were used for testing various model configurations.

First modeling results building up on the FIRE-ACE project are reported by Curry et al. (2000). All of the three models used in this study underestimated the liquid water path (9 to $22 gm^{-2}$) compared to observations ($43 gm^{-2}$), therefore yielding too high downwelling shortwave radiation and too low longwave radiation fluxes. Using a single column model with one-moment cloud microphysics parameterizations, Morrison et al. (2003) could not reproduce an accurate partitioning between liquid water and ice. Results with better agreement were achieved using two-moment cloud microphysics schemes (Morrison and Pinto, 2005, 2006), pointing out the critical dependence of the clouds' properties on ice nucleation. Since simulated ice crystal concentrations are often too low compared to observations, when accounting for removal of activated ice nuclei (IN) (e.g. Harrington and Olsson, 2001, based on REFLEX II (Kottmeier et al., 1994)), sensitivity tests with varying complexities with respect to the treatment of IN were conducted by Morrison et al. (2005b) and Fridlind et al. (2012).

Also related to the SHEBA/FIRE-ACE case, an intercomparison study was coordinated by Morrison et al. (2011b), using six cloud-resolving and large-eddy simulation models. Specifying constant ice crystal concentrations yielded qualitatively reasonable results with most of the models being able to simulate a persistent mixed-phase cloud. Morrison et al. (2011b) found a high sensitivity to the ice number concentrations.

Furthermore, the Mixed-Phase Arctic Cloud Experiment (M-PACE) was conducted in fall 2004 from September to October (Verlinde et al., 2007). Due to the autumnal conditions, the ocean was not covered with ice, therefore providing a source of latent and sensible heat. The location was at the North Slope of Alaska, which includes the region around Barrow as shown in fig. 1.1.

For this case, two model intercomparison studies exist. First, a single layer cloud was modeled by 17 single-column models and 9 cloud-resolving models (Klein et al., 2009). In this study, the interaction between the liquid and the ice-phase is highlighted, which is represented by different degrees of complexity among the models. In general, the LWP is underestimated. Only a part of the models could capture both LWP and IWP comparable to observations. However, considerable scatter occurred in the simulated ice number concentrations, covering five orders of magnitude.

The second intercomparison case investigates the more complex interactions of a multilayer cloud (Morrison et al., 2009). However, it shall not be discussed here since this work is based on a single-layer case.

A more recent campaign – which is related to this work – is named ISDAC (McFarquhar et al., 2011). The Indirect and Semi-Direct Aerosol Campaign was conducted during April 2008 at Barrow, Alaska with the aim to highlight differences between the fall conditions of M-PACE and the spring conditions of ISDAC. Investigations were related to the occurrence of aerosols as well as their feedback on cloud microphysical properties and radiation. Therefore, in addition to the long-term measurements at the Barrow site, in-situ data are available from aircraft measurements.

Besides several studies on cloud modeling (e.g. Fan et al., 2011; Ovchinnikov et al., 2011; Solomon et al., 2011), on radiative properties depending on aerosol loadings (Earle et al., 2011), on the variability of aerosols (Shantz et al., 2012) and aerosol compositions (Zelenyuk et al., 2010), a model intercomparison is among the ongoing projects (Ovchinnikov et al., 2012). For many studies, Flight 31 on April 26 was used as basis, described as a “golden day case” (Fan et al., 2011), since the observed cloud was a simple-structured single-layer mixed-phase cloud with dynamics driven by cloud-top radiative cooling and negligible surface fluxes of latent and sensible heat (Ovchinnikov et al., 2012). Flight 31 is characterized as a “clean case” with a total aerosol number concentration of approximately 250cm^{-3} , in contrast to a “polluted case” on April 8 with aerosol number concentrations greater than 500cm^{-3} (Earle et al., 2011). The in-situ measurements were obtained north-east of Barrow over the ice-covered Arctic ocean. The synoptic situation influenced by a high pressure system caused a weak easterly flow on April 26 (McFarquhar et al., 2011).

1.3. Objective

To sum up, not only simulations on a global scale show a wide spread in some aspects due to their high degree of parameterizing small-scale processes. Also on the cloud resolving scale, model intercomparisons show high sensitivities to partly small variations in ice number concentrations. A primary cause was found to be the interaction between the liquid phase and ice, therefore showing a critical sensitivity to primary ice formation. Motivated by these findings, the major topic of this work concerns the modeling of ice nucleation, based on ISDAC Flight 31 on April 26 in 2008. For simulating this case, the COSMO model (Doms, 2011; Doms et al., 2011) is used, including the COSMO-ART aerosol module (Vogel et al., 2009) and a two-moment cloud microphysics module originally presented by Seifert and Beheng (2006). To capture small-scale processes, the model is configured as a large eddy simulation (LES).

Chapter 2 provides the physical background of the most important processes involved, as well as the description of how they are represented in COSMO. Since some details in the existing parts of the model were modified, and additional parameterizations for ice nucleation and radiation were implemented, these changes will also be described in chapter 2.

A good opportunity to evaluate the model's performance are model intercomparisons as described above. Taking part in the ongoing ISDAC intercomparison is part of this work. Therefore, results of COSMO for this effort will be presented in chapter 3.

Chapter 4 contains the results of ice nucleation parameterizations and the effect of IN depletion. Two species of ice nuclei will be tested with respect to their influence on the ISDAC flight 31 mixed-phase cloud. In the end, an assessment of the possible roles of bacteria and natural dust acting as IN will be discussed.

2. From Physical Processes to Parameterizations

Based on the introduction of ice nucleation mechanisms in section 2.1, possibilities to parameterize them for modeling will be shown. After that, section 2.2 will describe the model extensions made as part of this work. Besides ice nucleation, additional details in the model were modified as a basis for the ISDAC model intercomparison. These model details will be presented in section 2.3.

2.1. Formation of Ice Crystals

One major attribute observed in the Earth's atmosphere is that clouds do not consist of frozen water droplets stringently, but stay in a liquid state above a threshold temperature well below 0°C. According to Wegener (1911) this is known since 1724 when Fahrenheit discovered supercooled clouds. The lowest temperatures measured in supercooled, possibly mixed-phase clouds reported up to Wegener's time is -20°C, observed from a balloon by Berson (Abmann and Berson, 1900).

The reason for water not to freeze instantaneously at subzero temperatures is summarized in chapter 2.1.1, followed by the description of enhancing mechanisms by ice nuclei and current possibilities for parameterization.

2.1.1. The Stochastic Process of Homogeneous Freezing

When a bulk mass of liquid water is cooled to temperatures below 0°C, small clusters of water molecules begin to form, called ice embryos (Pruppacher and Klett, 1997). They fluctuate in size, since small binding energies cause water molecules to attach to and detach from an embryo. The cluster will stabilize in case that a critical size is reached, typically containing an order of 10 to 100 water molecules (Pruppacher and Klett, 1997). It is then called an ice germ which is able to continue growing and form macroscopic ice. The challenge is therefore to reach germ size by passing an energy barrier through fluctuations of temperature and density in time and space (Pruppacher and Klett, 1997).

For the freezing of supercooled water, there is a need for "molecular reorientation involving the breaking of water-to-water bonds and the formation of water-to-ice bonds" (Pruppacher and Klett, 1997). It can be expressed by the molar Gibbs free energy of activation for diffusion of water molecules across the water-ice boundary, Δg^+ , or in short the molar activation energy. In contrast, for deposition nucleation only the work of ice germ formation ΔF_g has to be known, depending on the surface tension between water and ice $\sigma_{i/w}$ and on the ice germ radius $a_{i,g}$.

$$\Delta F_g = \frac{4\pi a_{i,g}^3 \sigma_{i/w}}{3} \quad [2.1]$$

The nucleation rate at constant temperature in the freezing mode is a function of Δg^+ and ΔF_g :

$$J(T) = fct(\Delta g^+, \Delta F_g) \propto \exp \left[-\frac{\Delta g^+}{RT} - \frac{\Delta F_g}{k_B T} \right] \quad [2.2]$$

with the universal gas constant R , the Boltzmann constant k_B and the temperature T . Thus, its magnitude strongly decreases at higher temperatures. Δg^+ cannot be derived theoretically, but can be calculated from the complete equation 2.2 provided that observed nucleation rates are available (Pruppacher and Klett, 1997). Another way was shown by Zobrist et al. (2007) who based the parameterization of Δg^+ on measurements of the diffusivity.

Assuming an array of equal sized water drops with droplet volume V_d at constant temperature T , the number of unfrozen and frozen droplets N_u and $N_f = N_{tot} - N_u$ is given as

$$N_u = N_{tot} e^{-V_d J(T) t} \quad [2.3]$$

where N_{tot} is the total number of droplets. Two points become apparent: First, there is a dependence on droplet volume, because for a larger amount of bulk water the chance for reaching a germ size is enhanced compared to small droplets with less water molecules. Second, the number of frozen droplets is time dependent. Therefore, it can be seen as a stochastic process (Pruppacher and Klett, 1997). For non-constant temperature, also the cooling rate $\gamma_c = -\frac{dT}{dt}$ has an influence on the time evolution of N_u . Qualitatively, this means a higher supercooling is possible for high cooling rates, since ‘‘matching’’ fluctuations within a short time interval are more unlikely than within a longer interval.

Bigg (1953b) reports that investigations on the volume dependence of nucleation rates did not start before the middle of the 20th century. Today, the homogeneous freezing temperature for pure water is well known to be in the range between -35°C and -40°C depending on the factors introduced above. Koop (2004) give a compilation of $J(T)$ for different cooling rates and droplet volumes based on a parameterization of Pruppacher (1995) shown in fig. 2.1. The freezing temperature can be defined as the temperature for which half of the droplets of an array are frozen when cooling begins at 0°C , which is the median freezing temperature (Koop, 2004).

Besides the process of homogeneous nucleation, heterogeneous nucleation occurs in the atmosphere. The former describes the phase change of a pure substance, whereas the latter involves additional substances acting as a catalyst for nucleation. With respect to J this means that for the same temperature, the homogeneous nucleation rate J_{hom} is less than the heterogeneous one J_{het} . To apply a formulation analogously to eq. 2.2, the heterogeneous work for ice germ formation can be expressed by

$$\Delta F_{g,het} = \Delta F_{g,hom} \cdot f(m); \quad m \equiv \cos(\theta) \quad [2.4]$$

where $f(m)$ is a prefactor depending on the contact angle between a spherical-shaped ice germ and its substrate, i.e. the ice nucleus (Chen et al., 2008). Since $f(m) \leq 1$, the nucleus lowers the energy barrier to form the critical ice germ. θ is an empirical property as a measure for the nucleation ability of a

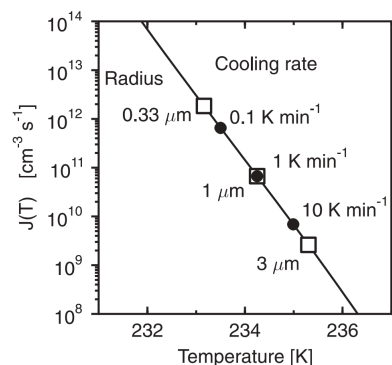


Fig. 2.1.: Parameterization of Pruppacher (1995) for the temperature dependent homogeneous volume nucleation rate coefficient $J(T)$ (Koop, 2004). Squares denote constant cooling rates of 1K min^{-1} , dots denote a constant radius of $1 \mu\text{m}$. Cloud droplets with radii up to $10 \mu\text{m}$ would be shifted to warmer temperatures in this plot.

substrate. It accounts for the matching of molecular structure between ice and the substrate. However, the assumed sphericity of the germ is an approximation, since an ice germ may have a hexagonal or prismatic shape (Chen et al., 2008).

Vali (1999) furthermore distinguishes between two mechanisms, deposition and freezing. The former means that ice germs are formed from water molecules directly from the vapor phase. For atmospheric conditions, no homogeneous but only heterogeneous deposition nucleation occurs (Vali, 1999). In contrast, the freezing mechanism is relevant for both, homogeneous and heterogeneous nucleation. In these cases liquid water exists before freezing and germs form within the liquid.

2.1.2. The Singular Hypothesis for Heterogeneous Nucleation

It was already mentioned in this chapter that supercooled water and clouds in particular could be observed already some time ago, which is not surprising after introducing the homogeneous freezing temperature. However, also clouds were observed which had never been colder than -4°C , but nevertheless contained ice crystals whose origin could not have been outside the cloud (e.g. Mossop et al., 1968). Consequently, there had to be an enhancing ice formation mechanism.

Already Wegener (1911) speculated about the abilities of different materials to initiate the freezing of a water reservoir. He pointed out the surface attributes roughness, crystalline structure and insolubility of the materials. Thus, he suggested specific surface details which would initiate freezing, with lower supercooling needed for substances containing bigger areas of such specific sites upon them.

Wegener's ideas match quite well with today's basic assumptions of the singular hypothesis. Contrary to the stochastic hypothesis for heterogeneous nucleation, which can be represented by eq. 2.3 analogously (assuming every particle to have equal properties but a Poisson distributed probability of freezing with respect to time (Vali and Stansbury, 1966; Vali, 1994; Connolly et al., 2009)), it is a simplified model

of the nucleation process by neglecting the dependence on time. Hence, each potentially ice initiating part of a particle's surface, called active site, is assumed to form an ice germ as soon as a specific freezing temperature is reached by cooling, the "characteristic temperature" T_c (Vali, 1994). In this case, the cooling rate γ_c does not have an effect as freezing is assumed to happen instantaneously. The ice active surface site density n_s is the number of active sites normalized by the particle surface area.

The singular hypothesis can be derived from the more general time dependent freezing rate (Vali, 1994), starting from the assumption of a whole set of particles, where each one has its constant nucleation rate at its specific temperature, i.e. $J_c(T_c) = \text{const}$. For an array of droplets with particles immersed in the droplets, the observed freezing rate $R(T, t)$ is given as

$$R(T, t) = V_d \int_{T_{hom}}^0 J_c(T) k(T_c, t) dT_c; \quad k(T_c, t) = k(T_c, 0) - \int_0^t J_c(T) k(T_c, t) dt. \quad [2.5]$$

where V_d is the volume of a droplet containing one nucleus and $k(T_c, t)$ is the number concentration of nuclei of different characteristic temperatures, also called nucleus spectrum (Vali, 1994; Vali and Stansbury, 1966) or nucleus content (Vali, 1971). The simplifying assumption for the singular hypothesis is that every nucleus has its own specific temperature with instantaneous freezing, i.e.

$$J_c(T > T_c) = 0; \quad J_c(T \leq T_c) = \infty. \quad [2.6]$$

In this case, the time-independent concentration function, also called differential nucleus spectrum derived by Vali (1971) is applicable (Vali, 1994):

$$k(T) = \frac{1}{V_d} \frac{1}{N(T)} \frac{\delta N}{\delta T}; \quad K(T) = - \int_0^T k(T') dT'. \quad [2.7]$$

In eq. 2.7, $k(T)$ has to be interpreted as a number of drops each containing a single nucleus characterized by its own freezing temperature which freeze during cooling by the amount of 1°C . Therefore, integration gives the cumulative spectrum $K(T)$ which offers the chance to characterize a sample of particles with respect to freezing. It is the number of activated particles cooled down from 0°C to any temperature $T < 0^\circ\text{C}$. Keeping in mind the assumption of the singular hypothesis, that the most active site of all sites upon a particle becomes active at its characteristic temperature instantaneously, only this one site with highest T_c is important for the freezing.

Eq. 2.7 describes the number of frozen droplets with respect to a droplet volume V_d , thus the units are $[m^{-3}K^{-1}]$. In contrast, relating $k(T)$ and hence $K(T)$ to the total surface area of an aerosol population, it can be interpreted as a number density with respect to an area with units $[m^{-2}K^{-1}]$ and $[m^{-2}]$, respectively. Connolly et al. (2009) investigated the condensation freezing mode, using the nucleus spectrum for the definition of the ice-active surface site density $n_s(T)$:

$$n_s(T) = - \int_0^T k(T') dT' = \frac{N_i}{N_d A_p} \quad [2.8]$$

N_i is the number of frozen droplets per volume of air that formed during the cooling process and A_p is the surface area of a single particle within a monodisperse aerosol population consisting of N_d particles per volume of air. Furthermore, the implicit assumption in eq. 2.8 is that every single particle is immersed in a liquid droplet, i.e. N_d is the number of unfrozen droplets by definition. In order to derive a fraction of ice related to the number of aerosol particles, eq. 2.8 can be rewritten for a particle size category j and assuming $k(T)$ to be independent of particle sizes. When freezing occurs, the total number of droplets and ice particles $N_{tot} = N_d + N_i$ is constant, therefore

$$\left. \frac{dN_i}{dT} \right|_j = N_d A_p |_{j} \cdot k(T) = (N_{tot} - N_i) A_p |_{j} \cdot k(T) \quad [2.9]$$

and integration yields the ice fraction $(f_i)_j$ for category j for a spherical potential ice nucleus with diameter D_p .

$$f_i |_{j} \equiv \left. \frac{N_i}{N_{tot}} \right|_j = 1 - e^{-\pi D_p^2 \cdot n_s(T)} = f_i(D_p) \quad [2.10]$$

A first-order Taylor series approximation of the exponential function in eq. 2.10, i.e. $e^x \approx 1 + x$, finally results in

$$f_i(D_p) \approx \pi D_p^2 \cdot n_s(T), \quad [2.11]$$

which is applicable as long as $\pi D_p^2 \cdot n_s(T) \ll 1$ so that the neglected elements of the series are close to zero. If this is not the case, the approximation overestimates the ice fraction, possibly resulting in a fraction greater than 1, which is physically not reasonable. The exact ice fraction and the relative error introduced by the approximation are shown in fig. 2.2. Provided that eq. 2.11 is valid, an easy summation over all particle sizes is possible, so that the total fraction of ice particles can be calculated by the total

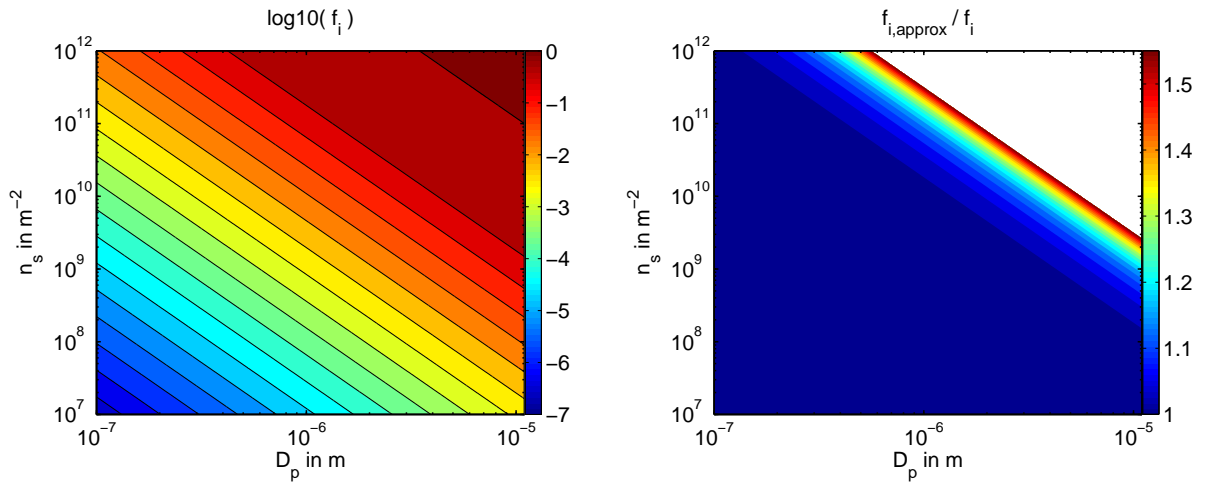


Fig. 2.2.: Left: Ice fraction depending on particle diameter and n_s . Right: Relative error of the approximation (eq. 2.11). The white area indicates unphysical results of the approximation with $f_i > 1$, i.e. it has to be hard-limited to 1 in this region if the approximation is applied. The ranges diameters and active surface site density correspond to the relevant values necessary for atmospheric modeling.

surface of an aerosol population S_{tot} , which has to be known in terms of its number size distribution $f_{NSD}(D_p)$.

$$f_{i,tot} \equiv \frac{N_{i,tot}}{N_{tot}} \approx \frac{S_{tot}}{N_{tot}} \cdot n_s(T) = \frac{1}{N_{tot}} \int_0^{\infty} \pi D_p^2 f_{NSD}(D_p) dD_p \cdot n_s(T) \quad [2.12]$$

Otherwise, the exact size dependent ice fraction can be calculated using eq. 2.10:

$$f_{i,tot} = \frac{1}{N_{tot}} \int_0^{\infty} f_i(D_p) f_{NSD}(D_p) dD_p = \frac{1}{N_{tot}} \int_0^{\infty} \left(1 - e^{-\pi D_p^2 \cdot n_s(T)}\right) f_{NSD}(D_p) dD_p \quad [2.13]$$

2.1.3. Distinction Between Heterogeneous Ice Nucleation Modes

Up to now, only the immersion freezing mechanism was mentioned, i.e. there is a particle within a liquid droplet which initiates ice germ formation. Unfortunately, notations about freezing modes are not uniform in literature. E.g. Pruppacher and Klett (1997) define the immersion freezing by a droplet which condenses on a cloud condensation nucleus (CCN) above $0^\circ C$ and then freezes at some level of supercooling. This way of definition gives a clear distinction between immersion and condensation freezing (see below). Others, for example Niedermeier et al. (2010) and Murray et al. (2012), allow the particle to act as CCN also below $0^\circ C$ which in this case is not a criterion for exclusion from the immersion freezing. Also here, after existing some time, the liquid droplet may freeze due to decreasing temperatures.

A similar freezing mode is condensation freezing. In this mode, the particle also acts as CCN, but necessarily below $0^\circ C$. The difference is that freezing happens during the process of condensation itself. Because of difficulties in a distinct separation, condensation and immersion freezing are sometimes treated as the same category (Niedermeier et al., 2010; Murray et al., 2012; Hoose and Möhler, 2012), where both involve the ice germ formation within liquid water.

For both freezing modes, the air has to be saturated with respect to water in order to activate a particle as CCN. Hence, the active surface site density approach can be adopted, where n_s is only a function of temperature (e.g. Connolly et al., 2009; Niemand et al., 2012).

In section 2.1.1, the distinction between freezing and deposition was introduced which is also valid for heterogeneous nucleation. In contrast to freezing, deposition acts below water saturation as shown in fig. 2.3. In this case, the main dependence is on the supersaturation of the air parcel with respect to ice, s_i , but also on temperature. Hence, n_s would be a function of s_i and T , respectively.

A nucleation event is called contact nucleation if it is caused by the collision between an existing liquid droplet and a single aerosol particle. This means that only interstitial particles which are neither immersed in droplets nor in ice particles can act as contact nuclei. Therefore, in addition to the nucleation ability of a particle, the collision probability has to be known depending on the sizes and relative

movements of droplet and aerosol particle, which means that the need for knowledge about the collection efficiency introduces additional uncertainty. Possible effects resulting potentially in collisions are the particles' and droplets' sedimentation velocities, but also Brownian motions of a potential contact nucleus. A further occasion for the particles' movements is thermophoresis caused by the non-uniform heating of a particle, as well as diffusiophoresis arising in a mixture of gases with concentration gradients (Pruppacher and Klett, 1997). Furthermore, the shear of a turbulent air flow is able to enhance collision probabilities.

There are some reports in literature estimating the effectiveness as relatively high compared to immersion freezing (Pruppacher and Klett, 1997; Vali, 1999). However, the analysis of experiments is difficult because of the collection efficiency mentioned above.

2.1.4. Cloud Microphysics and Ice Nucleation in COSMO

Ahead of the description of the ice nucleation which is already available in the two-moment cloud microphysics scheme, the two-moment scheme itself is introduced in this section. Besides ice processes, it contains the description of liquid water particles as well as the interactions between particles of different classes.

As indicated in section 2.1.2, different assumptions can be made for the heterogeneous ice nucleation, leading to more or less complex descriptions and the need of data input in order to get an output as result, namely an ice number concentration for a certain thermodynamic situation within a model's gridbox. In COSMO's two-moment formulation, there is a number of different possibilities to choose, which will be summarized afterwards.

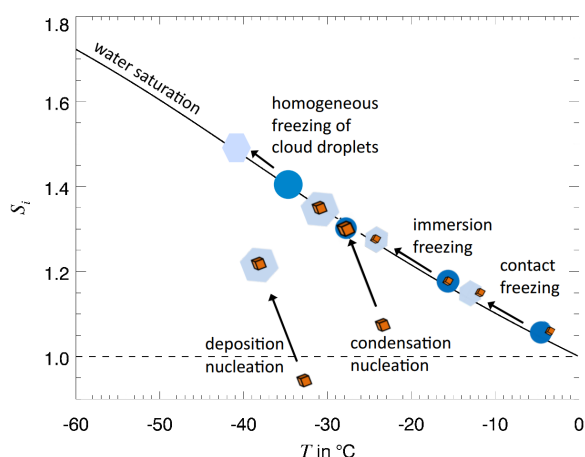


Fig. 2.3.: Illustration of freezing modes for droplets without soluble material. The dashed line denotes the vapor pressure equal to the saturation vapor pressure over ice, orange particles symbolize ice nuclei. (Hoose and Möhler, 2012, with changes)

Two-Moment Cloud Microphysics Representation

There are several possibilities with different degrees of complexity and computational costs to implement cloud microphysical processes into a model. The scheme available in COSMO which is used for operational weather forecast is a one-moment scheme, only calculating mass mixing ratios prognostically. In this case, number mixing ratios of hydrometeors are prescribed as constant values. This standard scheme is based on a formulation of Kessler (1969), grouping hydrometeors in classes depending on particle size thresholds (Schättler et al., 2009). In contrast to Kessler's original formulation, also ice categories are included in COSMO. The weather forecast version COSMO-DE calculates five categories of hydrometeors, namely cloud water, rain water, cloud ice, snow and graupel.

However, several microphysical processes are critically dependent on number concentrations of liquid and ice hydrometeor species, determining the particle sizes for a given mass mixing ratio of water. Sizes, in turn, need to be known in order to calculate physics accurately, like sedimentation and the effects of collisions between particles. It is therefore desirable to introduce a second prognostic variable for every hydrometeor species, namely the number mixing ratios.

Since hydrometeors are not equal-sized, their size distributions must be known, called particle size distribution (PSD). The shape of density functions in general can be described by their moments. The definition of the k^{th} moment for a size distribution $f(x)$ depending on a particle mass x is

$$M^{(k)}(x) = \int_0^{\infty} x^k f(x) dx, \quad [2.14]$$

Both mass concentration and number concentration can directly be related to the moments. In the formulation of Seifert and Beheng (2006), they are calculated as mass densities L and number densities N for each species:

$$M^{(0)} = N; \quad M^{(1)} = L \quad [2.15]$$

Processes involving the vapor phase are given by condensation, deposition, evaporation and sublimation as well as nucleation of droplets and ice particles. Existing ice particles may melt and liquid particles are allowed to freeze homogeneously and heterogeneously.

Particle interactions implemented for the liquid phase are selfcollection, autoconversion, accretion and breakup of droplets. Ice phase interactions - also involving liquid droplets - consist of riming, aggregation, conversion to graupel, enhanced melting (Rutledge and Hobbs, 1984) and ice multiplication (Beheng, 1982).

Detailed information on them is available in Seifert and Beheng (2006) and Seifert (2002).

There are even more sophisticated ways to calculate cloud microphysical processes. Above, they were represented by two moments, assuming the third moment of the PSD to be constant. Dropping this constraint would result in a three-moment scheme, allowing for the prognostic prediction of a third

moment. Such a treatment was developed by Milbrandt and Yau (2005), for example. In COSMO, with a PSD as function of particle mass, $M^{(2)}$ would correspond to the radar reflectivity (Seifert, 2002).

Finally, the most accurate way to treat cloud microphysics is to discretize the PSD into several bins instead of using the bulk description depending on moments. Usually some tens of bins are used for each hydrometeor species, resulting in a large number of prognostic variables and high requirements to computers. For example, Seifert et al. (2006) conducted a comparison study, finding good agreements between bin resolved calculations and the Seifert and Beheng (2006) bulk scheme with adjusted PSD parameters. Nevertheless they recommend to include both bin and bulk microphysics schemes into models, where the bin versions can serve for validation purposes.

Stochastic Freezing of Droplets: Bigg 1953

Bigg (1953b) used a stochastic approach for the description of heterogeneous nucleation of supercooled water drops with the assumption that the presence of the particles did not disturb the stochastic nature of nucleation (Pruppacher and Klett, 1997). Based on freezing measurements of droplet arrays (Bigg, 1953b,a), a relation for the freezing probability of a single droplet of volume V for time t and supercooling T_s was derived, which corresponds to a nucleation rate $J(T_s)$ (Pruppacher and Klett, 1997):

$$\ln(1 - P) = -VtK(e^{aT_s} - 1) \quad [2.16]$$

The constants $K = 2.9 \times 10^{-8} \text{cm}^{-3} \text{s}^{-1}$ and $a = 0.82 \text{K}^{-1}$ were obtained empirically and vary with the purity of the water. Barklie and Gokhale (1959) examined water of less purity than Bigg (1953b,a) did and found $K = 2 \times 10^{-6} \text{cm}^{-3} \text{s}^{-1}$ for distilled water, $K = 2.5 \times 10^{-4} \text{cm}^{-3} \text{s}^{-1}$ for tap water and $K = 2 \times 10^{-4} \text{cm}^{-3} \text{s}^{-1}$ for rain water (Pruppacher and Klett, 1997). In COSMO, $K = 1 \times 10^{-4} \text{cm}^{-3} \text{s}^{-1}$ is implemented.

This parameterization is usually switched on by default, regardless of any other ice nucleation mechanisms being active additionally. Based on the conclusions of Vali (1994), who found the heterogeneous freezing of droplets to be a combination of both, stochastic and singular behavior, this parameterization may be interpreted as a stochastic contribution to the total nucleation rate. In COSMO, this approach is implemented for cloud and rain droplets (Seifert, 2002).

Dependence on Ice Supersaturation: Meyers 1992

The work of Meyers et al. (1992) is one of the most cited and used parameterizations. It bases on a number of investigations of that showed a dependence of nucleation mainly on the supersaturation with respect to ice S_i in % (Pruppacher and Klett, 1997). Therefore, the parameterized number of ice nuclei per liter N_{IN} is expressed by

$$N_{IN} = e^{a+b \cdot S_i} \quad [2.17]$$

with $a = -0.639$ and $b = 0.1296$, which can be interpreted as nucleation in the deposition mode as well as immersion/condensation mode, as the vapor pressure may also be at or above the saturation vapor pressure with respect to water. The relation is valid for temperatures between -7°C and -20°C , ice supersaturations between 2% and 25% and water supersaturations between -5% and $+4.5\%$.

For the contact mode, an additional relation was derived which, however, is not used in COSMO due to the difficulties arising by the determination of the collection efficiency (Seifert, 2002). Meyers et al. (1992) also ascribes only little importance to the contact mode relative to eq. 2.17 because of measurement data by Vali (1974, 1976), Cooper (1980) and Deshler (1982). These data showed a number of potential contact nuclei that was smaller by several orders compared to data by Blanchard (1957), which served as basis for the contact nucleation parameterization by Young (1974), whose fit function yielded unrealistically high numbers of contact nuclei (Meyers et al., 1992).

Like in the stochastic approach, there is only an implicit dependence on aerosols which were present during the measurements on which the fit functions are based. Therefore, this kind of parameterization relies on an average of aerosol loading being present throughout the atmosphere at every time, which is represented by a limited set of measurements. Meyers et al. (1992) assesses the relatively small number of available data by continuous flow diffusion chamber (CFDC) measurements to be a potential weakness of this parameterization. Hence, it is desirable to include an explicit dependence of ice nucleation on aerosol loadings. Nevertheless, eq. 2.17 is also applied in the Phillips et al. (2008) parameterization which are explicitly aerosol-dependent.

Dependence on Aerosols: Phillips et al. (2008)

Equivalent to Meyers et al. (1992), the parameterization by Phillips et al. (2008) is based on measurements conducted in the atmosphere, too. The basic advantages are the given dependences for the whole range of temperatures down to -60°C , the distinction between three aerosol species “dust and metallic compounds” (DM), “inorganic black carbon” (BC) and “insoluble organic aerosols” (O). For given size distributions, the number of IN is related to the total surface area of aerosol species X per volume of air, which corresponds to an active sites approach and hence to the singular hypothesis (see sec. 2.1.2). For every one of the species X , the number concentration of IN, $n_{IN,X}$, is given by eq. (9) of Phillips et al. (2008), i.e.

$$n_{IN,X} = \int_{\log(0.1\mu\text{m})}^{\infty} (1 - e^{-\mu_X}) \frac{dn_X}{d\log D_{p,X}} d\log D_{p,X} \quad [2.18]$$

$$\mu_X = \mu_X(D_{p,X}, S_i, T) = H_X(S_i, T) \cdot \xi(T) \cdot \frac{\alpha_X n_{IN,1^*}}{\Omega_{X,1^*}} \cdot \frac{d\Omega_X}{dn_X} \quad [2.19]$$

$$\approx H_X(S_i, T) \cdot \xi(T) \cdot \frac{\alpha_X n_{IN,1^*}}{\Omega_{X,1^*}} \cdot \pi D_{p,X}^2 \quad [2.20]$$

assuming lognormal distributions of aerosols, so that the total number of IN is the sum of all species. D_p denotes the particle diameter, n are number mixing ratios. Ω_X is the surface area mixing ratio of all aerosols of species X larger than $0.1\mu\text{m}$ within an air parcel, while $\Omega_{X,1^*}$ is the component for aerosols with diameters between 0.1 and $1\mu\text{m}$ in the background scenario. H_X , ξ and α_X represent empirical values. The first one is a function of temperature and ice supersaturation and may have values from 0 to 1, i.e. the ice activity of certain species can be tuned to lower values in some regimes, depending on observations. For immersion freezing, it is equal to 1. ξ has a similar meaning, but is only a function of temperature and does not depend on the aerosol species. It prevents ice formation at temperatures higher than -2°C . α_X defines the fractions of the three species. Phillips et al. (2008) assumes the dust loading to be $\frac{2}{3}$ of the total aerosol, while the rest has to be partitioned with less certainty.

The subscripted stars occurring in μ_X denote reference values obtained by the measurements. It has to be pointed out that, although temperatures between 0°C and -60°C are covered, measurements are only available below -40°C , which is common for the CFDC technique. Hence, especially higher temperatures need to be extrapolated. Phillips et al. (2008) did so by using the fit function 2.17 of the Meyers et al. (1992) parameterization and scaling it with a prefactor in a way that its magnitude at -30°C and water saturation would match with the fit to the measurements at the same temperature. The scaled Meyers-fit is then used for T higher than -25°C , i.e. also outside its originally validated range, and the remaining interval down to -35°C is calculated by interpolation, where the extrapolation of the measurement fit begins. Thus, $n_{IN,1^*}$ is not simply a constant, but a function of temperature and ice supersaturation, depending on the temperature regime of a certain gridbox, where the calculations are done. The additional subscript “1” indicates that for the measured IN, only particles smaller than $1\mu\text{m}$ were counted.

The lower limit for the integration over the distribution is justified by Phillips et al. (2008) with the observation that snow crystals' central particles are mostly found to be larger than $0.1\mu m$. The approximation of eq. 2.20 is arises due to the assumption of spherical particles.

Using eq. 2.10, eq. 2.18 can be seen as a size dependent ice fraction multiplied by the size distribution, so that μ_X can be related to an n_s value for deposition and immersion/condensation freezing, respectively:

$$n_{s,X} = H_X(S_i, T) \cdot \xi(T) \cdot \frac{\alpha_X n_{IN,1^*}}{\Omega_{X,1^*}} \quad [2.21]$$

In the two-moment version of COSMO, eq. 2.18 is used to derive the total ice fraction $f_{i,X,tot}$ for a constant reference spectrum of each species X , which is multiplied by a given number concentration n_X to calculate the total number of ice particles

$$n_i = \sum_X f_{i,X,tot} n_X. \quad [2.22]$$

Also in this scheme, contact nucleation is not implemented. Nevertheless, Phillips et al. (2008) suggests that the number of interstitial particles which are potentially active in the contact mode can be related to $n_{IN,1^*}$, to the shift to warmer temperatures $\Delta T_{CIN} \approx 4.5^\circ C$ based on Shaw et al. (2005) and the surface area of interstitial aerosol $\Omega_{X,int}$. As described before, also here a collection kernel would be needed to apply this relation, i.e. eq. (14) of Phillips et al. (2008), as well as a distinction between interstitial and immersed aerosol particles.

When using this scheme for the sensitivity tests of chapter 4, only the DM-species will be used for the calculation of IN. Contrary to the default scheme which accesses a lookup table based on the size distributions given in tab. 3 of Phillips et al. (2008), the dust size distributions obtained at northern Alaska are applied in this work (see section 4.1).

2.2. Model Extensions for Ice Nucleation

As a part of this work, the model has been extended by the immersion freezing parameterizations of two particle species, namely mineral dust and bacteria. Both are expressed by the active surface site density as functions of temperature. Furthermore, the conditions in which immersion freezing is possible have been adjusted with respect to the treatment of activated particles and by defining a physically reasonable threshold for liquid droplets which are necessary for the immersion mode.

2.2.1. Immersion Freezing of Dust Particles: Niemand et al. (2012)

On the global scale, mineral dust particles contribute significantly to ice formation in clouds by acting as ice nuclei (Hoose et al., 2010b). For the immersion freezing mode, a parameterization was recently developed by Niemand et al. (2012). In contrast to the parameterization of Phillips et al. (2008), is based on data obtained in laboratory experiments. This enables the chance to draw conclusions on single species of aerosols and differentiate between them. On the one hand, atmospheric air is always contains a mixture of different particles. On the other hand, originally pure particles may have been altered in their ice nucleation properties due to aging, i.e. modifications of their surface properties by chemical processing. One may argue that the assumption of pure dusts in the atmosphere is quite an optimistic point of view. On the other hand, an exact discrimination between processes offers the possibility to learn about the underlying processes.

For this parameterization, pure dusts from four different locations were investigated by Niemand et al. (2012). It is valid at temperatures between -12°C and -36°C and at and above water saturation when T is given in $^{\circ}\text{C}$ and $a = -0.517$, $b = 8.934$:

$$n_s(T) = e^{aT+b} [m^{-2}] \quad [2.23]$$

The comparison of this function to the parameterization of Phillips et al. (2008) at water saturation and a fit for ice activity of biological particles is shown in fig. 2.4. The exponential dependence on temperature is steeper than for the rest of the curves at temperatures between -12°C and -36°C . This causes a smaller ice activity for T warmer than -25°C and a higher ice activity for T colder than -25°C . The strong change with varying temperatures was also pointed out by Niemand et al. (2012) and the consequences will be discussed in chapter 4. Because of the low n_s for pure dust at warm temperatures, the question arises which particles have a nucleation ability that is high enough to explain IN concentrations at warm subzero temperatures. Murray et al. (2012) estimate that dust (as well as soot) is primarily responsible for ice nucleation only below about -15°C .

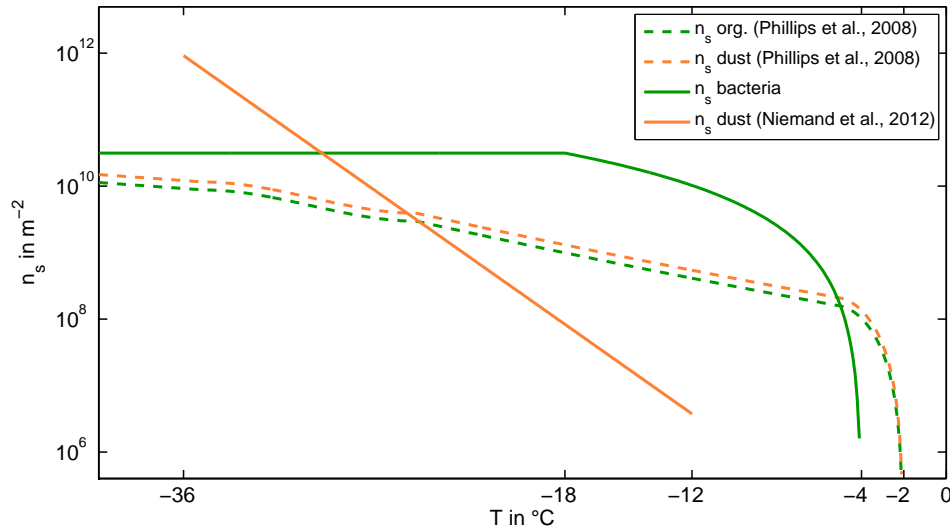


Fig. 2.4.: Active surface site parameterizations used in this work, except Phillips et al. (2008) for insoluble organics ($n_s \text{ org.}$), which is only plotted for comparison. See text for descriptions.

2.2.2. Immersion Freezing of Bacteria

According to the current knowledge about nucleation at warmer temperatures, an alternative with high ice nucleation ability are particles of biological origin (Murray et al., 2012). They are present throughout the troposphere in relevant number concentrations. Primary biological aerosol particles (PBAP) are defined by airborne aerosols directly emitted into the atmosphere by biological organisms, including microorganisms (Després et al., 2012). For a particle diameter $D_p > 0.4 \mu\text{m}$, they are estimated to contribute about 20% to the total aerosol number concentration (Murray et al., 2012). For airborne bacteria, this means typical concentrations greater than 10^{-2} cm^{-3} (Burrows et al., 2009a). This is a mean value of a global background concentration, which means that variations in space and time cannot be ruled out (Murray et al., 2012; Hoose et al., 2010a).

Some bacterial genera caused excitement in the field of atmospheric research because of their ability to nucleate ice at warm subzero temperatures. After Murray et al. (2012), bacteria are even among the most effective IN known in a temperature regime up to -2°C to -1°C (see fig. 2.5). Possible reasons which are considered to cause the high ice nucleation ability are protein complexes in the outer membrane of bacteria (Hartmann et al., 2012), enhancing the formation of ice germs by lattice match.

However, the ice nucleation ability does not only vary greatly between different kinds of bacteria, but also within a single genus. This is depicted in fig. 2.5 for *Pseudomonas syringae* (Ps) (Murray et al., 2012). In literature, the ice nucleation active fraction of bacteria relative to the total number concentration of bacteria, f_{INA} was established. For example Möhler et al. (2008) determined values for f_{INA} to be up to about 0.2 in a narrow temperature range around -8°C , but also down to an order of 10^{-4} for other temperatures, investigating the commercial Snomax™ product which consists of bacteria from the Ps

genus. Després et al. (2012) summarizes f_{INA} to be between 10^{-8} and nearly 1, while Lindemann et al. (1982) found the value for *Ps* and *Erwinia herbicola*, another common genus, to vary between 0 and 0.04 (Després et al., 2012). Phillips et al. (2008) chose for the “O” species which is mainly based on the activity of bacteria a general mean value estimation of $f_{INA} = 0.01$, so that 1% of the total bacteria loading would be ice nucleation active at all, for which parameterizations related to their surface can be derived.

For this work, an n_s -based parameterization is estimated by data published during the last decades. A compilation of n_s from several is given in fig. 2.5 by Murray et al. (2012) as well as in fig. 2.6 by Hoose and Möhler (2012). From these data, a fit-by-eye was created using a polynomial function analogous to Connolly et al. (2009), which in this case has the form

$$n_s = a(T + b)^2 \quad (-18 < T < -b); \quad [2.24]$$

$$n_s = a(-18 + b)^2 = \text{const.} \quad (T < -18). \quad [2.25]$$

T is the temperature in $^{\circ}\text{C}$ and the fit parameters $a = 1.6 \times 10^8 \text{m}^{-2}$ and $b = 4$ are chosen to fit the data points by eye, which results in the ice nucleation onset below -4°C with a steep increase above -10°C and an n_s slowly increasing with decreasing temperatures down to -18°C , below which it stays constant (fig. 2.4). The upper bound for the estimation is justified by the points given by Jayaweera and Flanagan (1982) also contained in fig. 2.6. These results are pointed out because the measurements were conducted in the Arctic, which is of special interest for this work. The maximum temperature of nucleation represented by b is also based on Jayaweera and Flanagan (1982). The constant value for colder temperatures is chosen due to observations that all of the ice nucleation active fraction of bacteria was already activated at higher temperatures (Jayaweera and Flanagan, 1982). This is also in agreement with Möhler et al. (2008) who found their specific bacteria to nucleate only in a narrow temperature range. Hartmann et al. (2012) found constant ice fractions already below -15°C , investigating ice nucleation active proteins of *Pseudomonas syringae*.

Because this $n_s(T)$ refers to the number of ice nucleation active fraction of bacteria only, the parameterized number of ice particles originating from bacteria is calculated with the prefactor f_{INA} using eq. 2.13:

$$N_i = f_{INA} \int_0^{\infty} f_i(D_p) f_{NSD}(D_p) dD_p \quad [2.26]$$

In order to apply the active surface site approach, the size distribution has to be known. In this case, a lognormal fit for measurements within the AIDA cloud chamber was used. The parameters for a unimodal number distribution fit for particles assumed to be spherical are chosen to be $D_{p,g} = 1 \mu\text{m}$ for the geometric median diameter and $\sigma = 1.34$ for the standard deviation, which means a relatively narrow peak compared to coarse mode dust (see section 4.1).

2. From Physical Processes to Parameterizations

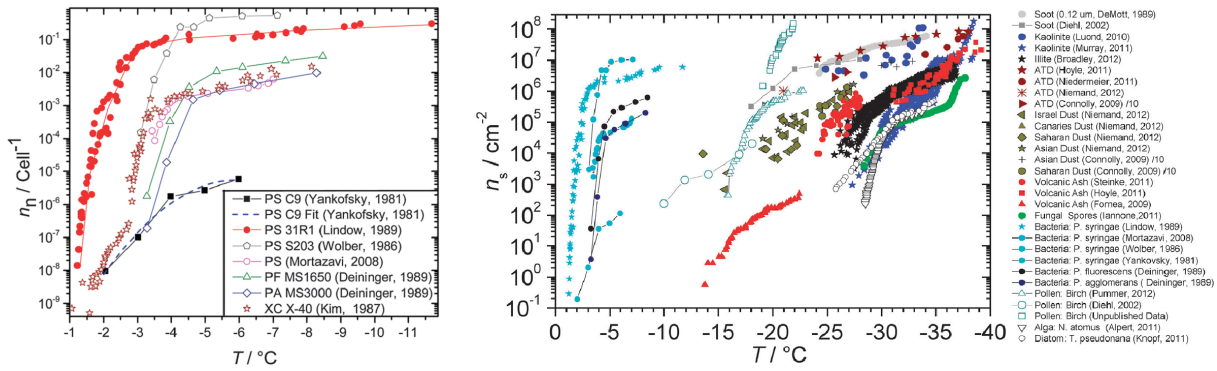


Fig. 2.5.: Left: Illustration of the ice nucleation variability of bacteria, e.g. for “*Pseudomonas syringae*” (PS). n_n is the number of active sites per cell and corresponds to the ice fraction in this case. Right: n_s compilation estimated by Murray et al. (2012), with uncertainties up to a factor of 10 arising from the calculation of surface areas. Murray et al. and Broadley et al. with smaller values of n_s because of using a gas adsorption method for the determination of surface areas which gives larger surface areas compared to mobility size measurements (Murray et al., 2012). Note the difference in n_s of factor $\times 10^4$ compared to fig. 2.6 owing to units.

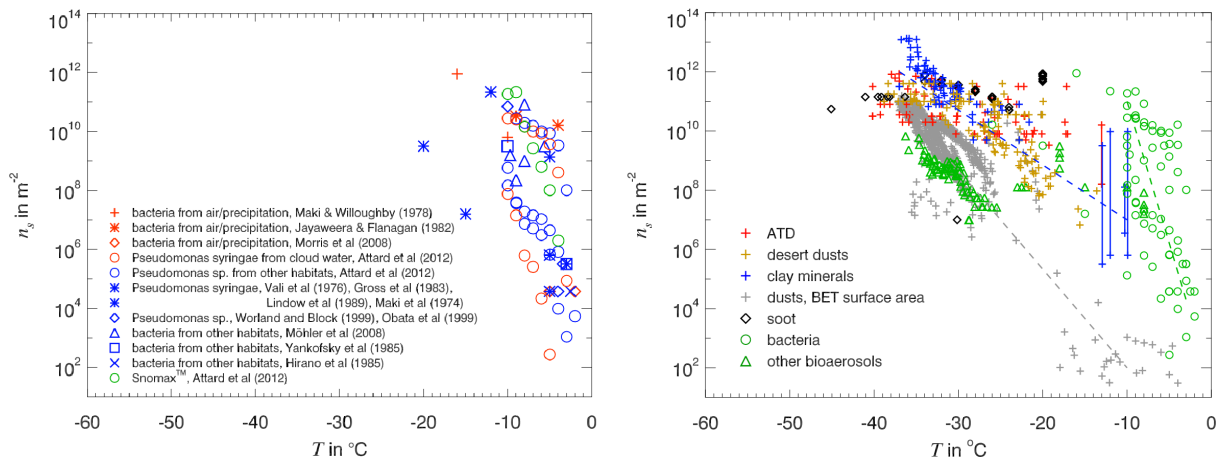


Fig. 2.6.: Left: n_s for immersion/condensation freezing and deposition at or above water saturation for bacteria (Hoose and Möhler, 2012). Right: Same as on the left, including all IN species for comparison (Hoose and Möhler, 2012). The blue line indicates mineral dusts, the green line indicates ice nucleation active biological aerosols.

2.2.3. IN Depletion due to Activation

In studies conducted during the last decade investigating Arctic Mixed-Phase Clouds (AMPC hereafter), large discrepancies have been found mainly caused by ice microphysics. One example is the model intercomparison based on the Mixed-Phase Arctic Cloud Experiment (M-PACE) during fall 2004 (Klein et al., 2009) at which 17 single-column models and nine cloud resolving models with 2D and 3D domains were compared. Although there were several models which could capture liquid and ice water paths consistent with observations, there was large scatter among different models. On the one hand, LWP was underestimated in many cases, on the other hand the variable with the largest scatter by far was found to be the ice number concentration. Because of the WBF process (see section 2.3.1), both are linked directly. Klein et al. (2009) note that not all models of the intercomparison treat the WBF process explicitly, but for the ones who do, a significant sensitivity of its efficiency arises due to assumptions about the capacitance of ice crystals and other parameters (see section 2.3.1; Pinto, 1998; Harrington et al., 1999; Jiang et al., 2000; Morrison et al., 2003; Morrison and Pinto, 2006; Prenni et al., 2007). This is why different models react differently to varying amounts of ice crystals.

However the ice number concentration itself, N_i , is probably one of the most uncertain variables, since it reflects the uncertainties and assumptions of different ways to parameterize ice nucleation. In the intercomparison of Klein et al. (2009), the spread of N_i covers five orders of magnitude for two-moment and bin microphysics schemes, which are able to prognose number concentrations (in contrast to single-moment schemes). While most of them treated the calculation of IN diagnostically, two of the models, namely DHARMA (bin scheme, see Fridlind et al. (2007)) and RAMS-CSU (bulk two-moment depending on Meyers et al. (1992)) were able to treat IN as prognostic variables. Besides differences in parameterizations, such kind of treatment, prognostic vs. diagnostic, also contributed significantly to the spread in results. Because Klein et al. (2009) estimate secondary ice production not to be of significant importance, N_i can clearly be ascribed to nucleation.

A model describes IN as prognostically, if the fraction of activated aerosol particles cannot act as IN any more in future timesteps after activation. Hence, these IN are depleted. Assuming a steady state for a simulated case without any motions of the atmosphere or changes in temperature, no further nucleation could occur with such a treatment (assuming the singular hypothesis holds with $n_s = fct(T)$ and without dependence on time so that $J \neq fct(t)$). For such a treatment, only two processes exist to nucleate ice in the proceeding model run:

- Cooling a parcel of air down to colder temperatures where a certain species of IN is more active than before, which would correspond mathematically to the integration of the differential ice nucleus spectrum over the temperature difference caused by cooling. In the simulations of AMPC, the most important cooling mechanism is the adiabatic cooling of ascending air parcels within updrafts.

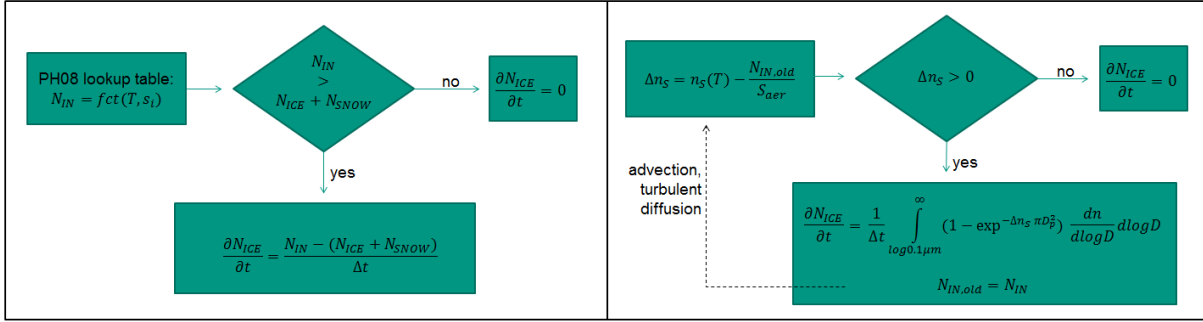


Fig. 2.7.: Left: Default treatment of ice nucleation in the two-moment scheme of COSMO, based on Phillips et al. (2008). Right: Depletion scheme using the additional prognostic variable $N_{IN,old}$ to account for activated ice nuclei.

- Assuming constant temperature for a single parcel of air, there is the possibility of advection of additional IN, which had not been depleted in the foregoing model run. For idealized runs of AMPC, where horizontal gradients are mostly close to zero, mainly vertical advection, i.e. boundary layer mixing, plays a role for this mechanism. A detailed discussion follows in chapter 4.

Of course, both cooling and mixing can occur simultaneously. Thus, a three dimensional model configuration is desirable.

The question arises what causes models not to produce infinitely high amounts of ice crystals when no prognostic treatment of IN is available. Usually, which is also true for COSMO, the number density of ice crystals – generated in previous time steps of the model run – are counted and interpreted as activated IN, since the latter are not directly known in that case. This standard implementation of the COSMO double-moment microphysics scheme is depicted on the left of fig. 2.7. In every time step, the number of IN is calculated using the Phillips et al. (2008) parameterization. All calculations described in section 2.1.4 are contained in a lookup table which returns the total ice fraction for the present situation, for size distributions specified in Phillips et al. (2008). In case that the number density of parameterized ice nuclei is greater than existing ice crystals (i.e. the sum of cloud ice and snow crystals), the difference is added in form of new cloud ice crystals specified with a minimum ice crystal mass m_{min} for freshly nucleated ice particles, for which a default value of $10^{-12}kg$ is defined.

In contrast, the depletion scheme depicted on the right of fig. 2.7 uses a subroutine containing the same physics as the lookup table used for the standard scheme based on Phillips et al. (2008). In spite of higher computational costs, it offers the possibility to directly specify different size distributions for the single aerosol species. Within this routine, the size distributions and therefore size dependent ice fractions (see eq. 2.10) are explicitly resolved. While the lookup table described above is based on calculations allowing for up to 10^4 size bins, it was found that the amount of about 50 size bins for particle diameters

between $0.1\mu\text{m}$ and $10\mu\text{m}$ is still accurate, but significantly reduces computation time. Since this scheme can also be expressed in terms of an active surface site density n_s (see section 2.1.4), this is done here for consistency with other n_s -based parameterizations (see sec. 2.2.1, 2.2.2), which can therefore be directly implemented within the existing framework. Knowing the number of depleted IN $N_{IN,old}$ which is a prognostic variable, it can be recalculated to a corresponding $n_{s,old}$, so that nucleation only occurs in case of n_s being greater than $n_{s,old}$, i.e. $\Delta n_s \equiv n_s - n_{s,old} > 0$.

$$n_{s,old} = \frac{N_{IN,old}}{\int_0^{\infty} \pi D_p^2 f_{NSD}(D_p) dD_p} \quad [2.27]$$

Besides changes in the number density of depleted IN by advection and turbulent diffusion, the only source term for $N_{IN,old}$ is the nucleation process. There are no sink terms assumed to be existent for the activated aerosols for these idealized simulations. For example, the complete evaporation of a crystal in subsaturated regions with respect to ice would correspond to the release of the activated aerosol particle and therefore would be a sink for $N_{IN,old}$. However, calculating the evaporated number density is not straightforward using the bulk microphysics of COSMO. Although the evaporation mechanism is already implemented (Seifert and Beheng, 2006), only mass densities change by evaporation, i.e. in the existing code crystals only shrink by evaporation, but do not completely disappear which would be expected in reality for the smallest fraction of crystals of a size distribution.

There are two effects resulting from the different treatments:

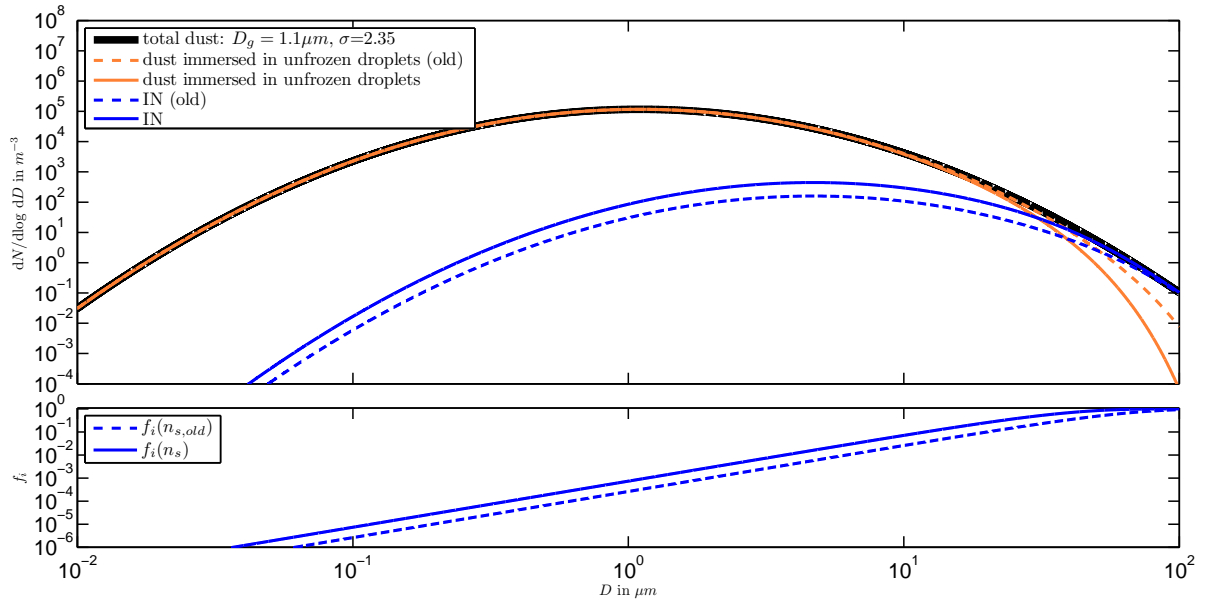


Fig. 2.8.: Cooling a parcel of air which contains a certain amount of dust from -18°C (dashed lines) to -20°C (full lines) results in an increase of N_{IN} as shown by the blue line of the upper plot, whereas a temperature change in the reverse direction would not result in freezing with the depletion scheme. The ice fractions correspond to the temperature dependence of n_s .

- First, sedimentation fluxes of cloud ice and snow crystals influence the number densities in each gridbox. Especially in regions with concentration gradients, this effect can be significant (see section 4.4). Using the default scheme connects nucleation to the presence of crystals that originate from locations different from the place where nucleation is calculated. In turn, crystals that develop in a gridbox, but leave to lower levels due to sedimentation, cannot be identified as nucleation event in their original location. In case of AMPC, the sedimentation flux divergence of ice crystals plays a role especially near cloud top, where no crystals drop downwards from above.
- Second, making nucleation dependent on existing ice crystals in the default treatment also means that secondary ice production directly influences the nucleation scheme. For example, assuming the Hallett-Mossop process to be active (Hallett and Mossop, 1974), which means that a riming ice particle can release up to one secondary ice splinter per 100 to 250 drops colliding with a crystal being rimed (Pruppacher and Klett, 1997), further nucleation would be reduced due to crystals not originating from nucleation. Obviously this kind of feedback is not physical which is avoided by counting depleted particles separately. The Hallett-Mossop ice multiplication is often assumed to be responsible for ice number concentrations being several orders higher than can be explained by nucleation alone (Pruppacher and Klett, 1997). Thus in the matching thermodynamic conditions, this kind of unphysical feedback can strongly influence parameterized ice nucleation rates.

For the AMPC discussed in this work, secondary production is not taken into account (see chapter 3, 4), so the main effect arising is the sedimentation effect. Not accounting for sedimentation of $N_{IN,old}$ implies that also aerosols do not sediment, since aerosols are the primordial cause of heterogeneous nucleation. Nevertheless it is assumed here, that this effect only plays a minor role for the LES setup, in which sedimentation velocities for aerosols are much smaller than the vertical velocity of the air flow which can be directly resolved due to the high spatial resolutions. This means that vertical advection and therefore mixing within the boundary layer is the dominating effect here, justifying neglected sedimentation.

2.2.4. Threshold for Immersion Freezing

As defined in section 2.1.3, the immersion freezing mode requires liquid droplets. Therefore, the default COSMO two-moment scheme distinguishes nucleation modes by checking for the existence of cloud water, i.e.

$$L_c > 0. \quad [2.28]$$

It was found that in some cases of this work, immersion freezing occurred below the liquid cloud layer. Possibly because of mixing and diffusion, L_c is not exactly zero below the cloud, but may have values of orders going down to $10^{-40} \frac{kg}{m^3}$ as shown in fig. 2.9, which would correspond to a droplet size of about $D = 10^{-11} \mu m$ for $N_d = 200 cm^{-3}$. To avoid such artifacts in the immersion freezing mode, the condition 2.28 was modified in this work.

Keeping in mind the minimum threshold for the mass of the smallest droplets, which is defined to be $m_{min} = 4.2 \times 10^{-15} kg$ (Seifert and Beheng, 2006) and corresponds to a diameter of $2 \mu m$, there must be a threshold greater than zero for the immersion freezing of droplets. The new condition for the cloud water mass density depending on the droplet number N_d is

$$L_c > L_{c,min} \equiv m_{min} N_d. \quad [2.29]$$

With $N_d = 200 cm^{-3}$, the threshold is $L_{c,min} = 8.4 \times 10^{-7} \frac{kg}{m^3}$, corresponding to the maximum in the color code of fig. 2.9. By the use of eq. 2.29, immersion freezing occurs above the dark red areas only.

It will be discussed in chapter 4 that especially regions close to the cloud base are important for nucleation because of entrainment of IN from below the cloud. In particular when simulating bacteria as IN, the colored region of fig. 2.9 can potentially cause errors in the ice formation.

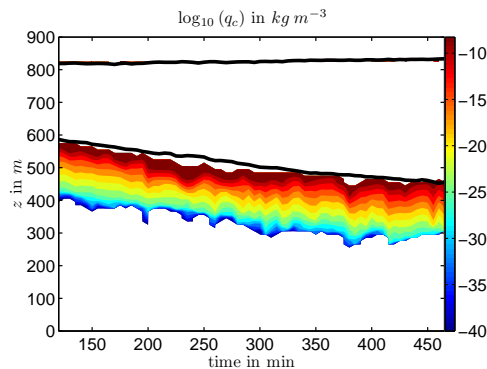


Fig. 2.9.: Liquid water content seen by the routine which decides whether to apply the immersion freezing parameterization or not. Only areas of $0 < L_c < L_{c,min}$ are colored to point out the difference between eq. 2.28 and eq. 2.29.

2.3. Further Important Model Details

In chapter 1, the interactions between liquid phase and ice were pointed out. Therefore, being the mechanism decisive for a mixed-phase cloud's persistence, describing the Wegener-Bergeron-Findeisen (WBF) process forms the first part of this section (2.3.1). Because this process is affected by the modifications to the model, an additional subsection gives a more detailed insight into the parameterization of ice crystal growth. The same applies to ice crystal sedimentation, which is described subsequently in section 2.3.2. After that, a newly implemented radiation treatment will be described in section 2.3.3, accounting for the cloud-top longwave radiative cooling of a stratocumulus cloud. It replaces the default radiation scheme for the simulations of this work. Finally, contrary to the foregoing parts, section 2.1.4 is not about modifications of the model, but is intended to give a short overview of the two-moment cloud microphysics scheme and point out its advantages compared to the simpler one-moment treatment.

2.3.1. Depositional Growth of Ice Crystals in the Presence of Supercooled Water

Below 0°C , the saturation vapor pressure over supercooled water exceeds the one of ice at the same temperature. Residing in the same environment, both liquid water and ice will have the ambition to reach their individual equilibrium state, such that water droplets will tend to yield more molecules than they take up from the vapor phase, i.e. they evaporate, while the opposite is true for the ice crystals. Thereby a gradient in water vapor concentrations evolves, inducing a diffusion flux of water molecules from water droplets towards ice crystals, which can thereby gain mass at the expense of water droplets. Mixed-phase clouds have often been reported to change from mixed-phase to ice-only on a time scale of hours (e.g. Pinto, 1998; Jiang et al., 2000).

The described process which involves coexisting ice crystals and water droplets is called Wegener-Bergeron-Findeisen (WBF) process, also denoted as Bergeron-Findeisen process in literature. It was first described by Wegener (1911, p. 80 f.):

“ Das eigentümliche und zugleich wichtige bei den Unterkühlungserscheinungen ist aber, daß, wie schon W. Thomson (1851) und Kirchhoff (1858) gezeigt haben, der maximale Dampfdruck über unterkühltem Wasser merklich größer ist als derjenige über Eis [...]. [...] Dieser Unterschied der Dampfdrucke über Eis und über unterkühltem Wasser bewirkt, daß die drei Phasen: Dampf, unterkühltes Wasser, und Eis unter keinen Umständen zu einem Gleichgewichtszustand kommen können, sofern die Temperatur aller Teile dieselbe ist. Die Folge muß dann sein, daß fortwährend Kondensation auf dem Eise stattfindet, während gleichzeitig fortwährend flüssiges Wasser verdampft, und dieser Vorgang muß so lange dauern, bis die flüssige Phase ganz aufgezehrt ist.”

However, Korolev (2007) raises concern that not in any case with both phases coexisting the WBF process is really active. This means that the distinction of three cases has to be made, depending on the actual vapor pressure e which can be below, in between, or above the saturation vapor pressure over

water e_s and ice e_i (see fig. 2.10):

- a) $e > e_s > e_i$
- b) $e_s > e > e_i$
- c) $e_s > e_i > e$

In any of the cases, e_i is below e_s , but only in *b*), the WBF process is active in the sense of evaporating liquid water and growing ice crystals. In contrast, *a*) causes growth of both droplets and ice crystals. This is a situation occurring in updrafts, when the vertical velocity w exceeds a threshold w^* (Korolev, 2007). An analytic expression for w^* was derived in Korolev and Mazin (2003), which depends on the saturation vapor pressures, the ice number density N_i , mean ice crystal radius \bar{r}_i and a coefficient η as a function of temperature and pressure:

$$w^* = \frac{e_s - e_i}{e_i} \eta N_i \bar{r}_i \quad [2.30]$$

The importance of this relation will be further discussed in 2.3.3.

In situation *c*) which is possible in downdrafts, droplets as well as ice crystals evaporate. Provided that $w < w^o$, the corresponding threshold for the evaporation regime is given as

$$w^o = \frac{e_i - e_s}{e_s} \chi N_w \bar{r}_w \quad [2.31]$$

where N_w and \bar{r}_w is the number density and mean radius of liquid droplets and χ is a coefficient depending on temperature and pressure (Korolev, 2007; Korolev and Mazin, 2003).

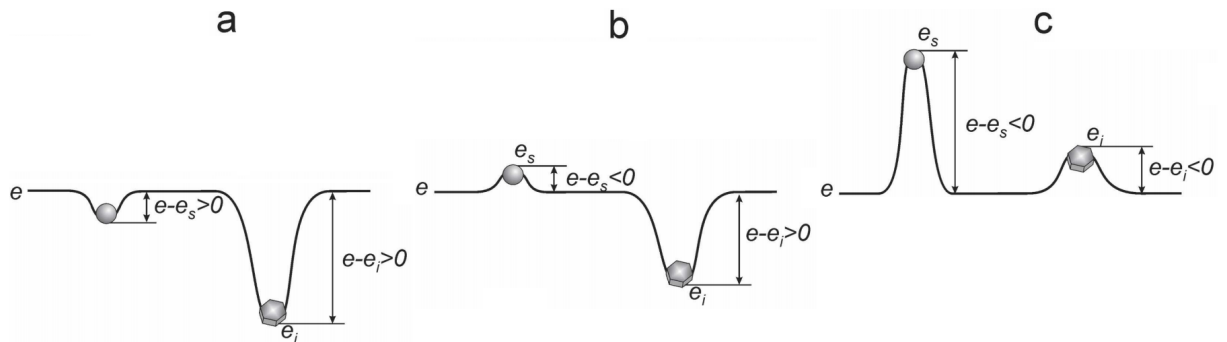


Fig. 2.10.: Illustration of three possible scenarios: a) both, liquid and ice grow when $w > w^*$. b) WBF regime. c) both evaporate when $w < w^o$ (Korolev, 2007).

Modeling the WBF process

In general, it is a challenge for the quantitative modeling of processes which involve ice crystals, since the particles can occur in a number of shapes (Pruppacher and Klett, 1997). The treatment in COSMO relies on an electrostatic analogon. This means that an ice crystal with surface temperature T_S and saturation vapor density at its surface $\rho_{v,i}$ are treated corresponding to a charged body which causes an electrostatic potential field Φ in its vicinity (Pruppacher and Klett, 1997). The result for a crystal's mass change rate without curvature and solute effects can finally be written analogously to a water droplet (Pruppacher and Klett, 1997) as

$$\left. \frac{dm}{dt} \right|_{crystal} \approx \frac{4\pi C s_i}{\frac{RT_\infty}{e_i(T_\infty)D_v^*M_W} + \frac{L_s}{k_a^*T_\infty} \left(\frac{L_s M_W}{RT_\infty} - 1 \right)}. \quad [2.32]$$

In this equation, $s_i = \frac{e}{e_i} - 1$ is the supersaturation over ice, R is the universal gas constant T_∞ is the temperature of the air surrounding the crystal, e_i is the saturation vapor pressure over a plane ice surface, D_v^* is the diffusivity of water vapor in air, M_W is the molecular weight of water, L_s is the specific latent heat of sublimation and k_a^* is the heat conductivity of air with stars denoting the correction of gas kinetic effects (Pruppacher and Klett, 1997). C is called capacitance. By assigning different values to it, ice crystal geometry can be taken into account. Assuming spherical ice particles, the radius would be used for C (Pruppacher and Klett, 1997). Throughout this work, hexagonal plates are assumed to be present in the cloud, which means in terms of the capacitance that

$$C = \frac{D}{\pi} \quad [2.33]$$

with crystal diameter D , i.e. mass growth rate is smaller than for spherical particles. Whenever D is mentioned here, the maximum Diameter of the crystal is meant, which corresponds to the diameter of an enveloping sphere.

In order to calculate C as function of particle mass, a relation between mass and diameter has to be specified. It is common to use a power law (Pruppacher and Klett, 1997) in the form

$$m = a_m D^{b_m}. \quad [2.34]$$

In order to apply consistent formulations among the models taking part in the model intercomparison, the coefficients $a_m = 44.2 \text{ kg m}^{-b_m}$ and $b_m = 3$ given by Ovchinnikov et al. (2012) are specified differently from the COSMO default values. Eq. 2.33 can be rewritten as

$$C = a_c m^{b_c} \quad [2.35]$$

where $a_c = 0.09 \text{ m kg}^{-b_c}$ and $b_c = 1/3$. Because eq. 2.32 describes a single particle, integration over the size distribution of ice crystals is necessary. In COSMO, a generalized gamma distribution with respect to particle mass m is used (Seifert and Beheng, 2006).

$$f(m) = Am^\nu e^{-\lambda m^\mu} \quad [2.36]$$

μ and ν are the parameters specifying the shape of the probability density function. In the version of COSMO used, they have the value $\mu = 1/3$ and $\nu = 0$, in contrast to the values given in Seifert and Beheng (2006) ($\mu = 1/3$, $\nu = 1$). The definition of the size distribution will have a significant influence on the glaciation of the cloud, which is discussed in chapter 3. A and λ expressed in terms of number and mass densities were calculated by Seifert (2002):

$$A = \frac{\mu N}{\Gamma(\frac{\nu+1}{\mu})} \lambda^{\frac{\nu+1}{\mu}}; \quad \lambda = \left[\frac{\Gamma(\frac{\nu+1}{\mu})}{\Gamma(\frac{\nu+2}{\mu})} \bar{m} \right]^{-\mu}; \quad \bar{m} = \frac{L_i}{N_i}. \quad [2.37]$$

Thus, the rate of change of the ice crystal mass density L_i is

$$\frac{dL_i}{dt} \approx \frac{4\pi s_i}{\frac{RT_\infty}{e_i(T_\infty)D_v^*M_W} + \frac{L_s}{k_a^*T_\infty} \left(\frac{L_s M_W}{RT_\infty} - 1 \right)} \int_{D_{min}}^{\infty} a_c m^{b_c} f(m) dm. \quad [2.38]$$

In this equation, D_{min} denotes the smallest ice crystals present in the model, i.e. the ones directly after nucleation. For an analytic evaluation of the integral it is convenient to assume a lower limit of 0 instead of D_{min} (Seifert, 2002), such that the definition of the gamma function Γ is applicable (Bronstein et al., 2008) which is calculated numerically within the model.

$$\Gamma(y) = \int_0^{\infty} x^{y-1} e^{-x} dx \quad [2.39]$$

$$\frac{dL_i}{dt} \approx \frac{4\pi s_i}{\frac{RT_\infty}{e_i(T_\infty)D_v^*M_W} + \frac{L_s}{k_a^*T_\infty} \left(\frac{L_s M_W}{RT_\infty} - 1 \right)} \frac{\Gamma(\frac{\nu+b_c+1}{\mu})}{\Gamma(\frac{\nu+1}{\mu})} \left[\frac{\Gamma(\frac{\nu+1}{\mu})}{\Gamma(\frac{\nu+2}{\mu})} \right]^{b_c} a_c \bar{m}^{b_c} N_i \quad [2.40]$$

This equation neglects ventilation effects, which are included in COSMO by default (Seifert, 2002). This is for the sake of comparability of model results in the frame of the model intercomparison (Ovchinnikov et al., 2012) described in chapter 3. In general, ventilation accounts for the air streaming past a crystal which moves in vertical direction with its sedimentation velocity (Beard and Pruppacher, 1971). This means, it is an enhancing factor for the ice crystal growth.

2.3.2. Sedimentation

Like the mass-dimension-relationship, the size or mass dependent sedimentation velocity can be parameterized by a power law. For a crystal, the relation is

$$v_i(m) = a_v m^{b_v}. \quad [2.41]$$

with parameters a_v and b_v . For the sedimentation of ice particles, the dependence on geometric shapes has to be taken into account, implying that a_v as well as b_v are only valid for a distinct shape of ice crystals, e.g. hexagonal plates. For example, dendritic crystals would sediment with lower speeds due to their lower equivalent density compared to a sphere of the same diameter.

Since the model represents size distributions of crystals, sedimentation affects both, ice number density N and mass density L . The prognostic equations for the moments $M^{(k)}$ are dependent on the flux $F^{(k)}$ of each of the moments, so their change with time can be calculated in the model by the corresponding divergence of the flux

$$F^{(k)} = \int_{m_{min}}^{\infty} v_i(m) m^k f(m) dm. \quad [2.42]$$

Analogously to section 2.3.1, integration over the whole gamma size distribution $f(m)$ with parameters μ and ν yields (Seifert, 2002):

$$F^{(k)} = a_v \frac{\Gamma(\frac{\nu+k+b_v+1}{\mu})}{\Gamma(\frac{\nu+k+1}{\mu})} \left[\frac{\Gamma(\frac{\nu+1}{\mu})}{\Gamma(\frac{\nu+2}{\mu})} \right]^k \bar{m}^{b_v} \cdot M^{(k)} \quad [2.43]$$

$$\equiv \bar{v}^{(k)}(\bar{m}) \cdot M^{(k)} \quad [2.44]$$

The divergence in vertical directions gives the prognostic relation for the moments. Evidently, eq. 2.43 depends on a_v and b_v specified for the ice crystal shape. In order apply identical assumptions in all

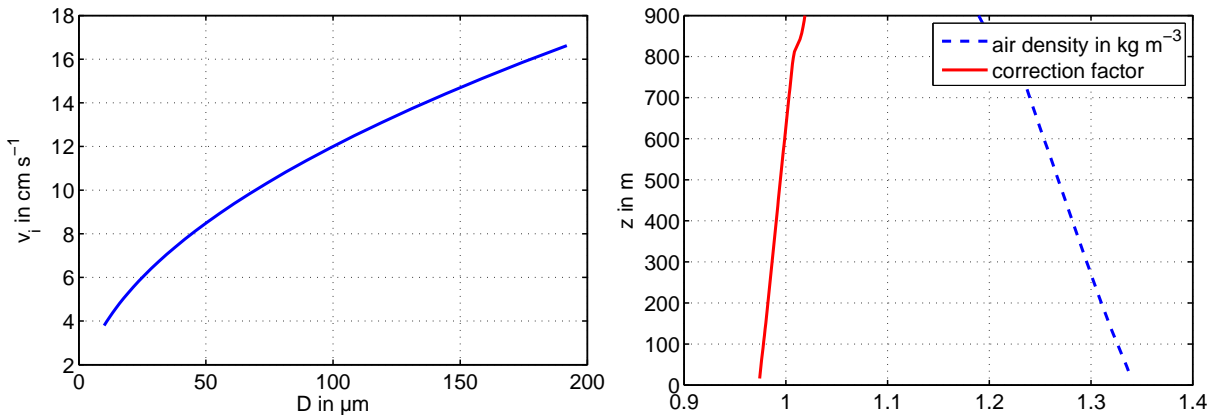


Fig. 2.11.: Left: ice crystal sedimentation velocity depending on diameter as calculated by eq. 2.45. Right: The correction factor depending on air density.

models taking part in the intercomparison (see chapter 3), they are defined differently from the model default values and adjusted to be consistent with the cloud observed during ISDAC. Ovchinnikov et al. (2012) give parameters corresponding to dendrites as function of D

$$v_i(D) = a'_v D^{b'_v} \quad [2.45]$$

with $a'_v = 12$ and $b'_v = 0.5$ so that using the mass-diameter-relation (eq. 2.34) results in $a_v = 6.39$ and $b_v = \frac{1}{6}$.

In reality, $\bar{v}^{(k)}$ is also a function of air density, resulting in higher velocities at higher altitudes due to decreasing air density with height. This correction factor is implemented by default in COSMO, but neglected for the ISDAC cloud with the same argument as used for the modified parameters. Anyway, its effect is small for the considered case, since the interesting region of the simulation is restricted to altitudes below about 850m so that its deviation from unity is within 2.6% including smallest values at ground levels (fig. 2.11). Approximately 600m over the surface it is equal to one, corresponding to a density of $1.25 \frac{g}{cm^3}$.

2.3.3. Cloud Top Radiative Cooling

Because the ground is negligible as a source of heat, which could induce a convective boundary layer and therefore be the reason for small-scale vertical motions, the most important driving force in AMPC is cloud top cooling by the emission of longwave radiation.

By default, the The THERmal Heating Rate (THHR) is calculated by COSMO using a δ -two-stream radiative transfer model (Ritter and Geleyn, 1992). Its denotation is based on the optical thickness δ and the two-stream approximation, separating radiative fluxes into the two distinct directions upward and downward. The electromagnetic spectrum is divided up into eight spectral intervals, whereas three of them are associate with the longwave components. Ritter and Geleyn (1992) point out the critical dependence of cloud radiative properties on number concentrations and size distributions of hydrometeors. Therefore, uncertainties in simulated cloud microphysical properties are also reflected in their radiative properties. To avoid such uncertainties among the models taking part in the model intercomparison, a simplified scheme was implemented in COSMO, calculating the THHR as a function of liquid water path.

The importance of liquid water for the longwave radiation emission of clouds was already pointed out in chapter 1. Stevens et al. (2005) used this connection to parameterize the net longwave radiative flux $F(z)$ depending on liquid water path and large scale subsidence only, based on sophisticated calculations using a δ -four stream model with input from observations. Within the framework of the model intercomparison (see chapter 3) and also for all of the sensitivity studies conducted for this work, only the parts of eq. 3 depending on LWP in Stevens et al. (2005) are used, neglecting the subsidence term. This is

justified by using a nudging approach for the idealized setup of the LES simulations (Ovchinnikov et al., 2012). Thus, $F(z)$ is only a function of $LWP(z)$ and the constants F_0 , F_1 and k (Ovchinnikov et al., 2012),

$$F(z) = F_0 e^{-k \cdot (LWP(z_t) - LWP(z))} + F_1 e^{-k \cdot LWP(z)} \quad [2.46]$$

where z_t denotes the cloud top height. The constants can be derived using a detailed radiation transfer model with input from observations. They are given in Ovchinnikov et al. (2012) with values of $F_0 = 72 \frac{W}{m^2}$, $F_1 = 15 \frac{W}{m^2}$ and $k = 170 \frac{m^2}{kg}$. LWP at height z is defined as the integral over a vertical column from ground level up to height z over the liquid water contained, i.e.

$$LWP(z) = \int_0^z \rho(z') q_l(z') dz' \quad [2.47]$$

with air density ρ and liquid water mixing ratio q_l . With a known radiation flux, the cloud's thermal heating rate is proportional to the flux divergence. With horizontal homogeneity, which is quite well fulfilled for liquid water in most of the simulations, the divergence can be calculated in the vertical direction only and the heating rate or cooling rate is given as

$$\frac{\partial T}{\partial t} = -\frac{1}{\rho c_p} \frac{\partial F}{\partial z}. \quad [2.48]$$

c_p denotes the specific heat capacity of dry air at constant pressure, which is very close to the value for atmospheric air containing water vapor (Pruppacher and Klett, 1997).

The resulting flux and cooling rate of this parameterization for typical conditions found during ISDAC flight 31 is shown in fig. 2.12. There is only a slight heating within the cloud, but a significant cooling in the uppermost layers of the stratocumulus. If a neutral or even stable stratification is assumed at some point in time, then the shown profile of temperature tendency will cause destabilization and finally

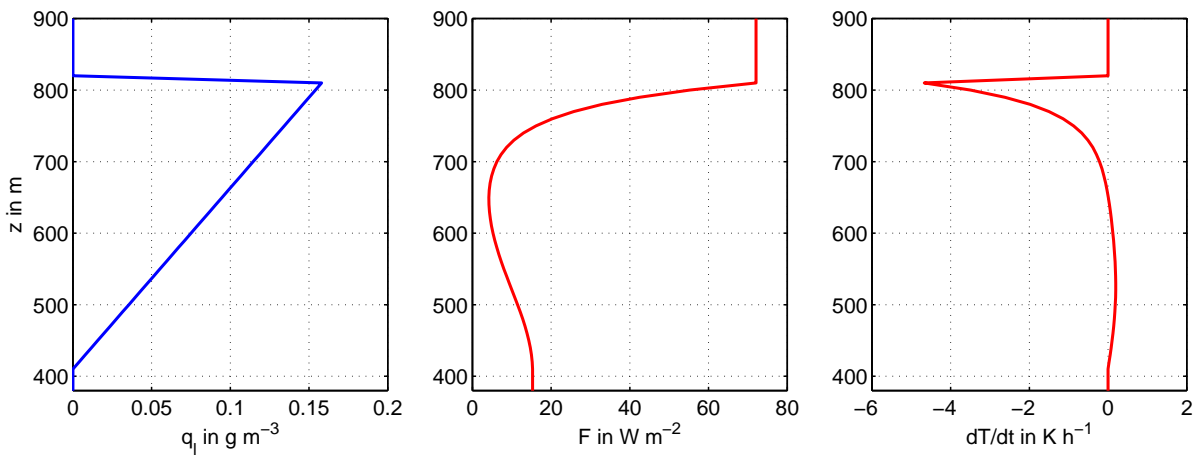


Fig. 2.12.: Cooling rate dT/dt parameterized as function of the flux divergence of longwave radiation which is dependent on the cloud's LWP and therefore liquid water content.

an unstable cloud layer, such that top layers descend and lower layers rise to higher levels. Therefore turbulence is induced within the cloud layer.

Implications for the Arctic Mixed-Phase Stratocumulus

As described in section 2.3.3, dynamics are predominantly driven by cloud top radiative cooling in this case, and therefore using equation 2.48, the amount of liquid water within a column of the atmosphere is responsible for the buoyant production of motions. It is plausible that a water vapor deposition rate onto ice crystals exceeding a critical threshold will lead to a loss of liquid water and the weakening of dynamics. For AMPC, this means that a mean deposition rate which is greater than the mean condensation rate would consume the liquid water.

From eq. 2.40 it can be seen that the change in ice mass density L_i is proportional to the number density of ice crystals N_i . Because of crystals growing from the vapor phase, this is also true for the loss of water vapor mass density. In turn, if the vertical velocity has a value between w^* and w^o , the WBF process will be active so that liquid water loss is also dependent on the number of ice crystals present.

For this case, only immersion freezing is assumed to be present, so that the nucleation of new ice particles can only take place in the presence of cloud droplets. Accordingly, a consumption of liquid water by WBF will also result in a decreasing nucleation rate. Once the liquid has disappeared completely the cloud's further development is fully predestinated. Ice crystals still sediment to the ground and leave behind clear air as there is no mechanism to reinitiate dynamics, liquid water formation as well as ice formation.

These descriptions apply to the idealized model setup with periodic boundary conditions (see section 3.1) which represents a closed system. In contrast to reality, there are no horizontal advection influences by large scale transport of temperature or moisture, for example. This is due to the small domain size commonly used for large eddy simulations. In this simulations conducted in this work, the horizontal

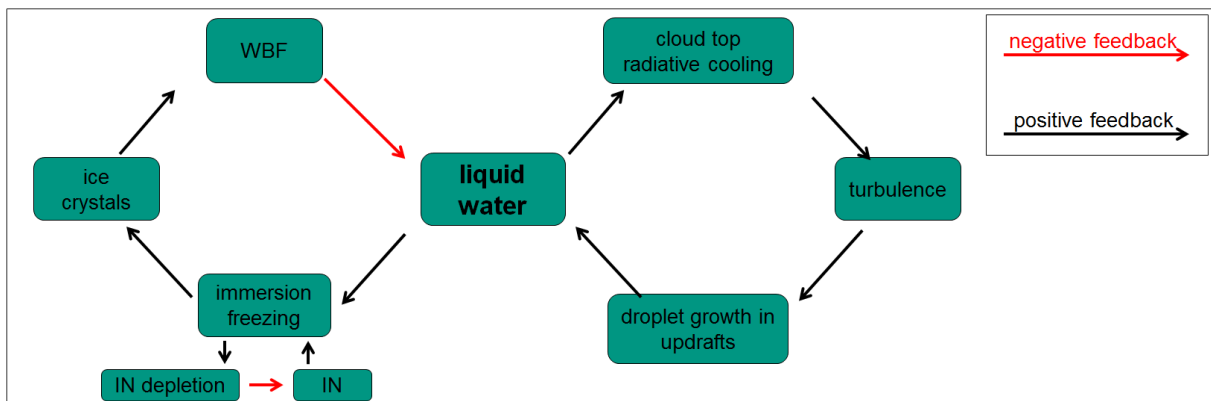


Fig. 2.13.: Subset of feedbacks which are most important in this work. Sensitivities are figured out by directly influencing WBF (chapter 3) as well as immersion freezing and IN depletion (chapter 4).

dimension is 3.2km (chapter 3) and 6.4km (chapter 4), respectively.

Furthermore, heat and mass fluxes from the ground are assumed to be negligible (section 3.1.1; Ovchinnikov et al., 2012), so the boundary layer containing the cloud layer is decoupled from the ground. Hence, it cannot serve as source for moisture.

All in all, there is a chain of positive feedbacks as shown in fig. 2.13. A more sophisticated and complete compilation of feedbacks is available in Morrison et al. (2011a), fig. 2.

3. COSMO's Performance in a Cloud Resolving Configuration

In this chapter, preliminary results of the ISDAC model intercomparison (Ovchinnikov et al., 2012) are presented, based on flight 31 on April 26 2008 of the campaign (McFarquhar et al., 2011). This intercomparison is intended to identify the source of spreads in model results gained in previous model intercomparisons which were based on SHEBA/FIRE-ACE and M-PACE (see chapter 1). In contrast to those, additional constraints in the model physics are specified in order to reduce the variability among the models. As introduced in the previous chapter, the unification of physical relations concerns the mass dependence and the dependence of sedimentation velocities of crystals on their diameter, as well as simplified ice crystal growth calculations and the parameterization of cloud-top radiative cooling.

After the description of the model setup, the results of COSMO and the sensitivity to different specified ice crystal concentrations will be discussed. After that, the variability among different models and possible reasons will be depicted. Additional sensitivity tests were performed to identify the inter-model variability.

3.1. Model Setup for LES Simulations

A feature of the COSMO model is that it is not restricted to mesoscale simulations, since dynamics are not affected by any scale approximations (Doms, 2011). Although the highest resolutions for operational weather forecast use is 2.8km covering an area of roughly 1000km^2 (COSMO-DE, Germany) and 2.2km (COSMO-2, Switzerland), this model can also be applied on a an even smaller scale.

In order to draw conclusions for single clouds, especially vertical motions induced by turbulence have to be known as accurate as possible, because they cause adiabatic cooling or warming in updrafts or downdrafts, and determine supersaturations. Thus, higher resolutions for modeling are desirable when single clouds shall be investigated, such that most of the turbulent motions which are parameterized in COSMO-DE can be calculated explicitly by integration of the Eulerian equations. This is where cloud resolving models (CRM) and large eddy simulations (LES) can benefit from going down to spatial scales of some tens of meters. The further distinction for this category of models is made due to the model domains. Klein et al. (2009), for example, refer to CRM as models with 2D domains, whereas full 3D configurations are called LES simulations. The latter can cover the three-dimensional nature of turbulence.

In nature, turbulent eddies occur also on spatial scales smaller than an LES grid, finally reaching sub-millimeter sizes where they are dissipated by viscous forces. Therefore, also an LES model should not be used completely without a parameterization of small-scale turbulence. It will be shown, however, that

the magnitude of subgrid turbulent kinetic energy (TKE) is some orders below resolved TKE. In general, it is most important near ground where shear is high, but is also present within the cloud layer. For this work, an alternative scheme different from the default setting was used (see chapter 6), which is intended to be used for LES-like simulations. A sensitivity test with subgrid turbulence being switched off will be shown in section 3.3.2.

3.1.1. Model Domain, Boundary Conditions and Initialization

It was already pointed out that AMPC critically depend on vertical motions which regulate droplet growth, ice formation and the WBF process. For the model intercomparison, the gridboxes were defined as $\Delta x = \Delta y = 50m$ in horizontal directions and $\Delta z = 10m$ in vertical direction. Because of the small spacing, it is not possible to cover areas as large as COSMO-DE does. In this case, 64 horizontal gridpoints exist in every direction, resulting in a total domain of $3.2 \times 3.2 km^2$ and a domain top of $2km$. A short summary of the model configurations is given in chapter 6.

Such relatively small domains are common for LES simulations. However, the horizontal extent is virtually infinitely big, as boundary conditions are periodic. This means that any prognostic quantity which is advected out of the domain, will simultaneously return into the domain at its opposite boundary. This is done for all of the four horizontal boundaries. Since it turned out that a total horizontal domain size twice as large did not change the results with respect to their horizontal mean values, the size chosen is considered to be appropriate. The top of the domain is set to $2000m$, which is not a constraint for this case because all of the relevant physical processes occur below $1000m$ within the boundary layer.

An implication given by periodic boundary conditions is that the domain can be interpreted as closed system in the horizontal direction. Once initialized, the further development is completely self-determined without any external boundary conditions being prescribed. Therefore, the only source or sink for heat and momentum is the ground if no nudging is applied to the model variables (see below in this section).

The timestep for integration of the prognostic equations is set to $1s$, required by the fine spatial resolution. The total time of integration is chosen to be 8 hours including two hours of model spin-up. During this period, the dynamics are assumed to fully develop by the interaction of radiative cooling and turbulence. No ice processes are switched on during spin-up, i.e. only liquid water is present for the first two hours.

In order to initialize the meteorological state of the model, idealized profiles given by Ovchinnikov et al. (2012) are used. They are based on the ISDAC campaign (see chapter 1). For the large scale state, a sounding from at Barrow is applied, whereas the mixed-phase cloud layer was sampled in more detail by the Convair aircraft. A combination of both defines vertical profiles of horizontal wind components (not shown) u and v , liquid water potential temperature θ_l and the total water content q_t (see fig. 3.1). It is the sum of all phases of water occurring in the model, i.e. water vapor, liquid water and ice water, whereas liquid water contains cloud droplets and rain water and ice water contains cloud ice, snow flakes, graupel and hail. θ_l was first defined by Betts (1973) and represents the potential temperature for an air

parcel when all of its liquid water contained evaporates during its wet adiabatic descent. It is therefore identical to the potential temperature θ if the parcel is not saturated with respect to water, i.e. $q_l = 0$. An approximate form was given by Betts (1973) where L_e is the latent heat of evaporation of liquid water:

$$\theta_l \approx \theta \left(1 - \frac{L_e}{c_p T} q_l \right). \quad [3.1]$$

Since COSMO does not operate with this variable, a combination of the given θ_l and q_l is used to determine temperature, water vapor mixing ratio and relative humidity iteratively assuming all moisture exceeding a saturation ratio of 1.0 to be liquid. In a first step, q_l is set to zero giving a temperature profile in order to calculate a first estimate of liquid water. The results after two more steps of refinement shown in fig. 3.2 presents the liquid layer with increasing q_l with height, on top being limited by the inversion capped boundary layer. It contains a liquid water path (LWP) of approximately 14gm^{-2} .

The Surface pressure is 1020hPa and surface roughness length is set to $4 \times 10^{-4}\text{m}$ based on Morrison et al. (2011b). Because the scenario is located over the ice-covered Arctic ocean and the lowermost layer is stably stratified, surface fluxes of sensible and latent heat are neglected by all of the models. Also the Coriolis force is neglected. Directly after the initialization, pseudo-random fluctuations of temperature are superimposed within the boundary layer with an amplitude of 0.1K . This helps to initiate turbulence, which can freely develop after this first impulse. For example, Ovchinnikov and Kogan (2000) found that this way of initialization yielded more realistic clouds in idealized model setups.

Further specifications concern the nudging of the atmospheric conditions towards the prescribed profiles, which generally increases in strength with height and has its largest effect above the cloud layer. This technique helps to keep the very limited model domain near its realistic state, although the influence on the simulations is only moderate because of the specification of nudging coefficients. For tempera-

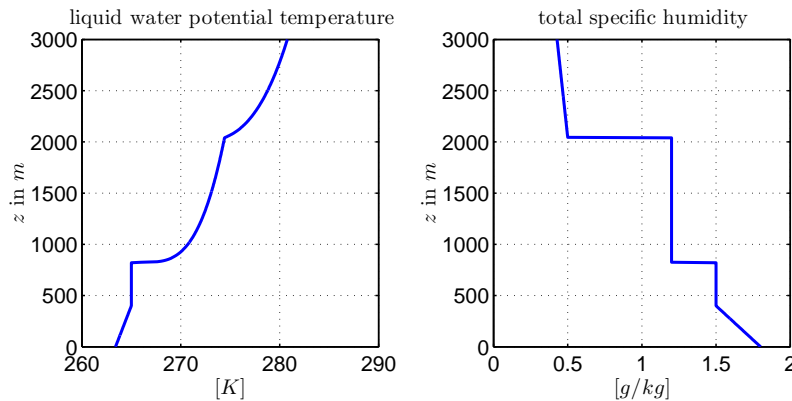


Fig. 3.1.: Vertical profiles of the liquid water potential temperature and total specific humidity derived for ISDAC flight 31 on April 8th 2008 (Ovchinnikov et al., 2012).

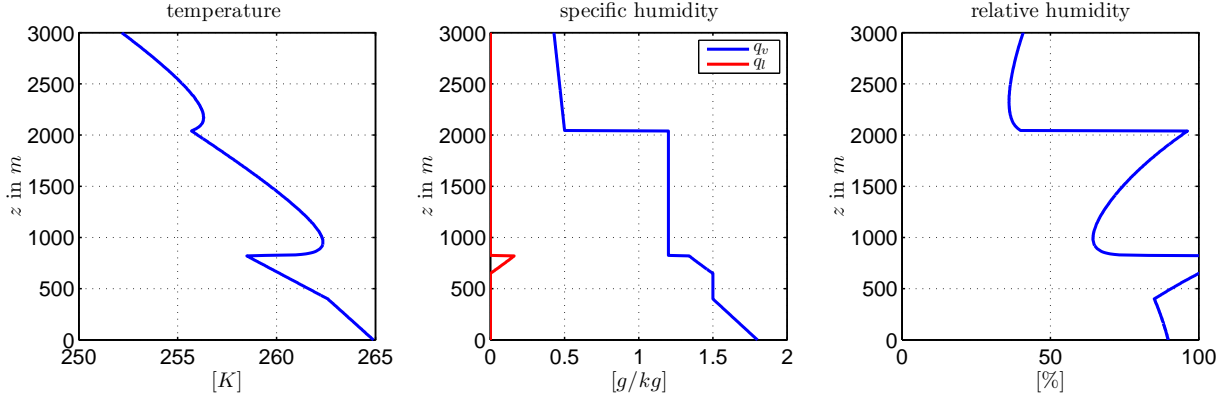


Fig. 3.2.: Profiles derived from liquid water potential temperature and total humidity.

ture and moisture, there is no nudging below 1200m such that the cloud evolution is not disturbed. The implementation is done by adding additional source terms for each of the prognostic variables ϕ , i.e.

$$\Delta\phi = -c_\phi [\phi(z) - \phi_0(z)] \Delta t \quad [3.2]$$

where c_ϕ is the nudging coefficient determining the strength. ϕ_0 is the prescribed value, i.e. the further the state of the model moves away from its prescribed state, the stronger $\Delta\phi$ will be.

Similar to nudging, an additional source term is introduced to capture the effect of atmospheric large scale subsidence w_{LS} corresponding to a high pressure system. Hence, for each prognostic variable ϕ except wind components, the subsidence term $\Delta\phi_{LS}$ is calculated:

$$\Delta\phi_{LS} = -w_{LS} \frac{\partial\phi}{\partial z} \quad [3.3]$$

The analytic expressions for the profiles are as follows (Ovchinnikov et al., 2012):

$$\theta_l(z) = \begin{cases} 265 + 0.004(z - 400) & [K] & (z < 400m) \\ 265 & [K] & (400m \leq z < 825m) \\ 266 + (z - 825)^{0.3} & [K] & (825m \leq z < 2045m) \\ 271 + (z - 2000)^{0.33} & [K] & (z \geq 2045m) \end{cases} \quad [3.4]$$

$$q_t(z) = \begin{cases} 1.5 - 0.00075(z - 400) & [g/kg] & (z < 400m) \\ 1.5 & [g/kg] & (400m \leq z < 825m) \\ 1.2 & [g/kg] & (825m \leq z < 2045m) \\ 0.5 - 0.000075(z - 2045) & [g/kg] & (z \geq 2045m) \end{cases} \quad [3.5]$$

$$\begin{aligned} u(z) &= -7 & [m/s] \\ v(z) &= -2 + 0.003 \cdot z & [m/s] \end{aligned} \quad [3.6]$$

$$c_{\theta}(z) = c_{q_t}(z) = \begin{cases} 0 & [1/s] & (z < z_1 = 1200m) \\ \frac{1}{3600} 0.5 \left[1 - \cos\left(\pi \frac{z - z_1}{z_2 - z_1}\right) \right] & [1/s] & (z_1 \leq z \leq z_2 = 1500m) \\ \frac{1}{3600} & [1/s] & (z > z_2) \end{cases} \quad [3.7]$$

$$c_u(z) = c_v(z) = \begin{cases} \frac{1}{7200} 0.5 \left[1 - \cos\left(\pi \frac{z}{z_{uv}}\right) \right] & [1/s] & (z \leq z_{uv} = 825m) \\ \frac{1}{7200} & [1/s] & (z > z_{uv}) \end{cases} \quad [3.8]$$

$$w_{LS}(z) = \begin{cases} -5 \times 10^{-5} \cdot z & [m/s] & (z < 825m) \\ -0.4125 \times 10^{-2} & [m/s] & (z \geq 825m) \end{cases} \quad [3.9]$$

The cloud microphysics are specified by droplet as well as ice number densities N_d and N_i . In contrast to the full treatment of the two moment scheme, which would calculate N_x based on prognostic equations, both are set constant for the model intercomparison. N_d is set to $200cm^{-3}$ for all of the simulations, based on measured concentrations (McFarquhar et al., 2011). Ice number concentrations serve for sensitivity tests to determine the model's behavior with respect to ice. For sensitivity tests, three simulations are conducted which are called "Ice0 / Ice1 / Ice4" corresponding to $N_{i,0} = 0 / 1 / 4l^{-1}$. Thus, one sensitivity test excludes ice particles. These number concentrations are set in regions where supersaturation with respect to ice and liquid water exists:

$$\frac{\partial N_i}{\partial t} = \max\left(0, \frac{N_{i,0} - N_i}{\Delta t}\right); \quad (S_i \geq 0.05; q_l \geq 0.001g kg^{-1}) \quad [3.10]$$

This parameterization counteracts any sinks of ice crystals. Thus, sedimented particles are immediately replaced by new ones with initial crystal sizes of $10\mu m$. The condition of q_l is specified to simulate immersion freezing only (Ovchinnikov et al., 2012). Depositional growth and sedimentation are treated as described in sections 2.3.1 and 2.3.2.

3.2. Results of COSMO

This section will describe the development of the relevant quantities in the model. The first part is for Ice0 when no ice is present, followed by the sensitivity tests Ice1 and Ice4. Figure 3.3 summarizes the model results. In all figures, the time series begins after two hours of spin-up. In colored contour plots, thick black lines mark cloud base and top, respectively, defined by liquid water thresholds of $q_l = 10^{-7} \frac{kg}{kg}$.

Except for the maximum vertical velocity w_{max} which is the maximum reached on each model layer, all of the plots show horizontal mean values of the domain. This means that in such plots no differentiation between regions of updrafts and downdrafts is made, justified by the fact that measurements conducted by aircraft also represent mostly mean values over larger spatial scales than the extent of single turbulent eddies.

3.2.1. Development of a Liquid-Only-Cloud: "Ice0"

In fig. 3.3 a) to c), the liquid water path (LWP) is shown. As mentioned in section 3.1.1, the initial atmospheric boundary layer contains roughly $14 gm^{-2}$ of LWP. This amount is increased during spin-up as turbulence develops and vertical mixing begins. Vertical mixing can clearly be seen by analyzing the water vapor content q_v which shows a reservoir of moisture near the surface in the beginning of the simulation, but is consumed with advancing time by mixing. Turbulent transport, i.e. vertical advection in updrafts brings vapor into the cloud layer where it can condense by adiabatic cooling in the updrafts. Accordingly, the growing liquid layer is directly linked to the decreasing amount of water vapor below the cloud. At some point in the temporal evolution, the boundary layer is completely mixed and vertical gradients of q_v below the cloud are close to zero which happens at about 6.5 hours of simulation time in the Ice0 case. This moment mainly depends on the strength of mixing, and hence on the cloud top cooling rate which is a function of LWP (see section 2.3.3, fig. 2.13). At this stage of mixing, also the initially strong growth of the liquid layer is decreased, since the reservoir has been dried out and cannot continue to feed the cloud. However, in cases of weaker mixing it is also possible to maintain the low level pool of q_v , which will be discussed in the next section when ice is included.

Another point visible from fig. 3.3 is the in-cloud development of q_v which decreases slightly with time. Since this layer is saturated with respect to water, the decreasing q_v is connected to the weak temperature reduction within the cloud which is especially the case at cloud top. Additionally, the large-scale subsidence defined by w_{LS} strengthens the inversion by warming the layers above the cloud. Furthermore, vertical velocities increase with time, which is directly linked to the LWP.

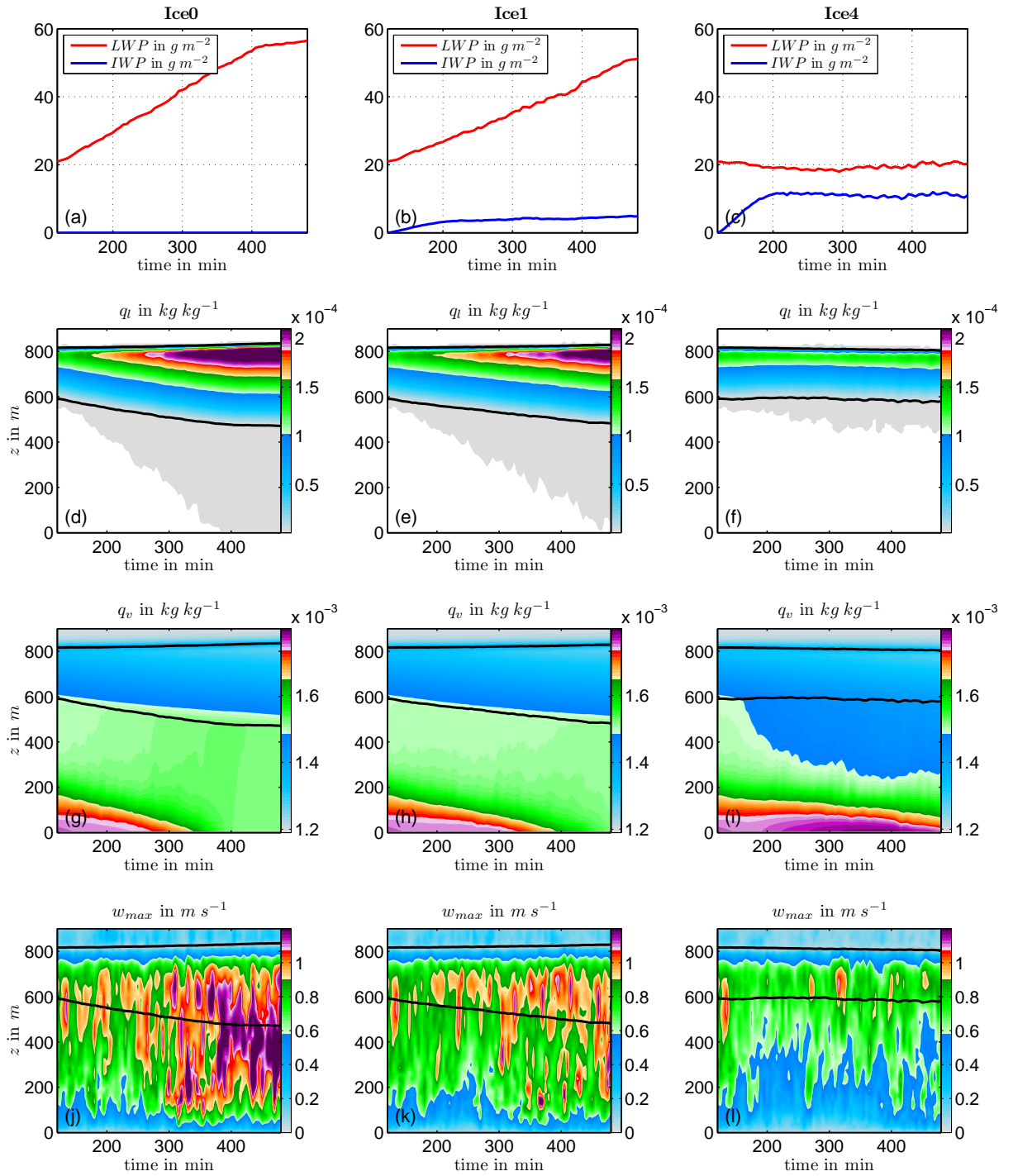


Fig. 3.3.: Time series of liquid water path (LWP), ice water path (IWP), liquid water content (q_l), water vapor content (q_v), temperature (T) and maximum vertical velocities (w_{max}). Left to right: Ice0, Ice1 and Ice4 corresponding to $N_i = 0 / 1 / 4 l^{-1}$.

3.2.2. Development of a Mixed-Phase Cloud: “Ice1”, “Ice4”

Results with ice processes are shown in columns 2 and 3 of fig. 3.3. For both sensitivity runs, the ice water path (IWP) starts at 0gm^{-2} because this is the time when ice crystals are first formed. They begin to grow by water vapor uptake, while the LWP has a smaller growth rate compared to Ice0, and stays approximately constant for Ice4. The reason for an increasing IWP is an effect of both, crystal growth and sedimentation. Initially with no ice being present below cloud, only in-cloud crystals which were formed instantaneously after spin-up contribute to IWP. With increasing time, they sediment but are replaced simultaneously within the cloud due to the prescribed ice number density (see eq. 3.10), leading to an initial growth in the vertically integrated ice crystal number concentration, called ice crystal burden hereafter. These processes, growth and sedimentation, take about 1 to 1.5 hours, then a quasi steady state is reached for Ice4, whereas for the Ice1 run IWP continues to grow very slightly. Because ice crystals can only form within the liquid layer (see eq. 3.10), this slowly increasing IWP is related to the vertical extent of the cloud, which also continues to increase.

With increasing ice number concentrations, not only LWP but also the vertical extent of the layer decreases (fig. 3.3). The Ice4 run can therefore be seen as a quasi equilibrium as it stays relatively constant with respect to most of its properties, namely LWP, IWP, cloud depth and turbulence. With higher water vapor deposition rates, dynamics are weakened which can be expected regarding the parameterization of radiative cooling. Therefore, the consumption of water vapor from the lowest level of the boundary layer is weak, subsequently keeping the moisture profile close to its initial state.

With higher ice number concentrations present, ice crystal sedimentation and snowfall rates increase which is an important factor for lower levels. In fig. 3.4, deposition rates are shown, i.e. the growth rates of ice and snow crystals. As soon as the air is subsaturated with respect to ice, crystals begin to evaporate during their descent, corresponding to negative deposition rates in fig. 3.4 e) and f). With more crystals being present, the total amount of water returning from ice into the vapor phase in lower levels also becomes more significant, which reduces the drying effect of boundary layer mixing (see section 3.2.1). That is why not only weaker dynamics, but also enhanced evaporation rates of ice crystals in low levels help to maintain the initial moisture profile.

The ice production rate (eq. 3.10) is most active in the uppermost cloud layer (see fig. 3.4). This is because at the top level, the flux divergence of sedimenting ice crystals is highest, since there is no feeding by crystals from the free atmosphere above the capping inversion. There is also enhanced ice formation at cloud base after ice initialization. The reason for this effect is the vertical advection of air into the cloud base that does not contain crystals, forcing the parameterization to adjust the prescribed number every time the mixing occurs. This enhanced cloud base ice formation declines in the continuing simulation because after some time, the air being entrained into the cloud base contains sedimenting crystals. Therefore, the entrainment does not affect the ice number concentrations within the cloud significantly.

Although ice production rates are highest at cloud top, the maximum of specific cloud ice content is located even below cloud base. This is clearly related to crystal growth during sedimentation which is positive for altitudes down to 400m for Ice4, before evaporation begins below 400m.

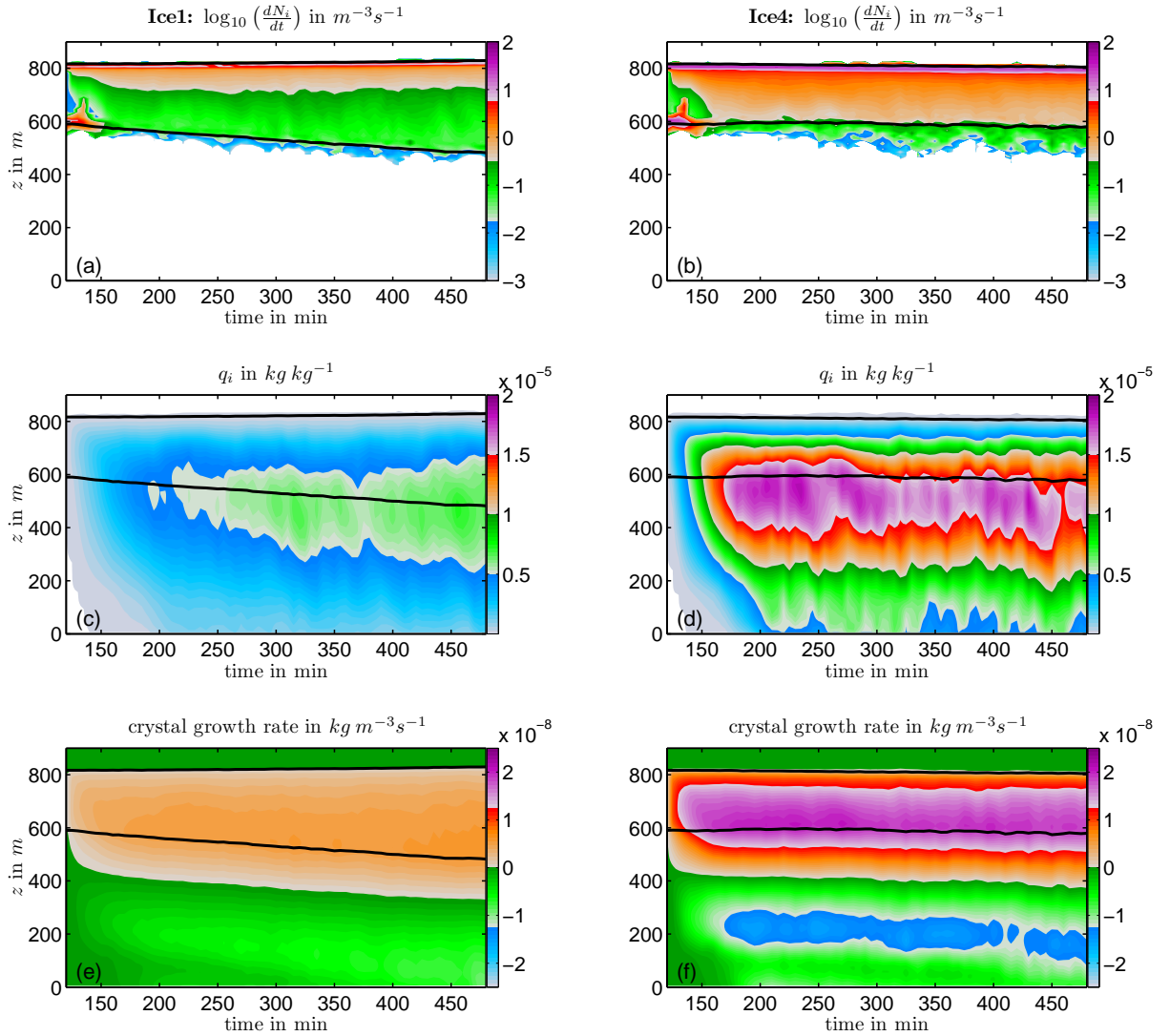


Fig. 3.4.: Time series of ice production rates ($\frac{dN_i}{dt}$), ice contents (q_i) and crystals growth rates by water vapor deposition for Ice1 run (left) and Ice4 run (right). Negative deposition corresponds to evaporating crystals.

3.3. Discussion of Results in the Context of the Model Intercomparison

In figs. 3.5 and 3.8 preliminary model results are shown in terms of LWP and IWP as well as correlations to maximal vertical velocities simulated by the models. Since these plots show a whole model run by one single data point, values are averaged over the period of 60 minutes, i.e. 12 model output time steps from hour 5 to hour 6. The discussion of COSMO's results which are shown in this section focusses on two aspects, namely the strength of liquid water consumption by ice crystal growth and the vertical velocities simulated by the models. It must be pointed out that this plot is preliminary. Therefore, no specific model names will be mentioned in this work, except that COSMO is represented by the filled dots.

3.3.1. Liquid Water Dissipation

In fig. 3.5, averaged results for the LWP and IWP are shown for several models. All except the cross symbol – which is a bin model – utilize cloud microphysics schemes based on a two-moment formulation. The three encircled symbols located close to each other use the microphysics scheme by Morrison et al. (2005a), which is a first hint that the treatment of microphysics is a dominant factor for the simulation of this case. Also with respect to dynamics, those three models do not seem to be completely different, since without ice their spread is within 2gm^{-2} . Simulatin Ice0, COSMO does not differ greatly, yielding approximately 48gm^{-2} within a total model spread between 30gm^{-2} and 52gm^{-2} . With increasing ice number concentrations, COSMO moves towards smaller LWP and greater IWP. Only the bin model calculates even more IWP, which means that there must be larger, i.e. heavier crystals since the number density is prescribed and the cloud depth has a similar extent (not shown). To verify the meaning of vapor

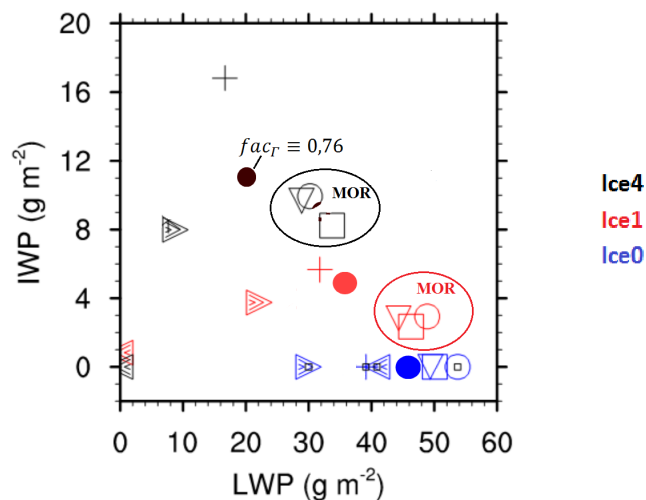


Fig. 3.5.: Preliminary model intercomparison results. Blue: Ice0. Red: Ice1. Black: Ice4. Different symbols correspond to different models. Courtesy of Mikhail Ovchinnikov, with changes.

deposition which relates crystals growth and liquid water consumption to each other, some sensitivity tests were conducted with COSMO which will give a picture of the range for a possible spread of results.

Because the amount of ice crystals being present is a major factor which controls the cloud's development, it is important to point out the specific assumptions made for the described set of simulations regarding to water vapor deposition rates (see also section 2.3.1).

Substituting eq. 2.40 with

$$\frac{dL_i}{dt} \approx \frac{4\pi s_i}{\frac{RT_\infty}{e_i(T_\infty)D_v^*M_W} + \frac{L_s}{k_a^*T_\infty} \left(\frac{L_s M_W}{RT_\infty} - 1 \right)} \cdot fac_\Gamma \cdot a_c \bar{m}^{b_c} N_i, \quad [3.11]$$

the results for a varying factor fac_Γ can be seen in fig. 3.6. In COSMO, this factor contains the information on both, size distribution and the ventilation effect that enhances ice crystal growth due to the crystals sedimentation velocity. As described, the specification for the intercomparison was to neglect ventilation, yielding a fac_Γ as shown in eq. 2.40:

$$fac_\Gamma = \frac{\Gamma\left(\frac{\nu+b_c+1}{\mu}\right)}{\Gamma\left(\frac{\nu+1}{\mu}\right)} \left[\frac{\Gamma\left(\frac{\nu+1}{\mu}\right)}{\Gamma\left(\frac{\nu+2}{\mu}\right)} \right]^{b_c}. \quad [3.12]$$

In this case, it only depends on the constant parameters of the size distribution, namely $\mu = \frac{1}{3}$ and $\nu = 0$ by default, corresponding to a factor of 0.76.

With everything else except fac_Γ being specified identical for all of the models using bulk microphysics, the spread in LWP and IWP was the reason for a closer examination of the different specifications for size distributions. Specifically, the comparison to the three models denoted by ‘‘MOR’’ in fig. 3.5 is discussed in the following, as they are results of different models using the same microphysics scheme by Morrison et al. (2005a). Same as in the scheme of Seifert and Beheng (2006) implemented in COSMO, it uses a gamma distribution, but the difference is that Morrison et al. (2005a) calculate distributions as a function of the particle diameter D , whereas Seifert and Beheng (2006) use functions of particle mass m (or rather x in their notation). The size distribution of Morrison et al. (2005a) has the form

$$f_{MOR}(D) = N_0 D^{p_c} e^{-\lambda D}. \quad [3.13]$$

Comparison shows that p_c , called the spectral index or shape factor, corresponds to ν of eq. 2.36 and $\mu \equiv 0$ here, resulting in an exponential distribution as a special case of the gamma distribution. To calculate $\frac{dL}{dt}$, integration analogous to section 2.3.1 and using the expressions for λ and N_0 given by Morrison et al. (2005a) results in the following equation, when the mass-diameter relation is given as $m = cD^d$ and $\bar{m} = \frac{q_i}{N_i}$:

$$\left. \frac{dL_i}{dt} \right|_{MOR} \approx \frac{4\pi s_i}{\frac{RT_\infty}{e_i(T_\infty)D_v^*M_W} + \frac{L_s}{k_a^*T_\infty} \left(\frac{L_s M_W}{RT_\infty} - 1 \right)} \frac{1}{\pi} \frac{\Gamma(p_c + 2)}{\Gamma(p_c + 1)} \left[\frac{\Gamma(p_c + d + 1)}{\Gamma(p_c + 1)} \right]^{-\frac{1}{d}} c^{-\frac{1}{d}} \bar{m}^{\frac{1}{d}} N_i \quad [3.14]$$

This form can be compared to eq. 2.40. With the default shape factor for ice crystals ($p_c = 0$, also used for the intercomparison), the factor arising due to the contribution of $f_{MOR}(D, p_c = 0)$ corresponds to a $fac_{\Gamma} = 0.55$ in COSMO. As shown in fig. 3.6, the LWP when using a fac_{Γ} close to 0.5 fits well to the three models using the Morrison scheme and may lead to the conclusion that COSMO's low LWP compared to most of the other models can be related to its default particle size distribution, causing higher water vapor deposition and ice crystal growth rates. In other words, COSMO simulates a more efficient WBF process.

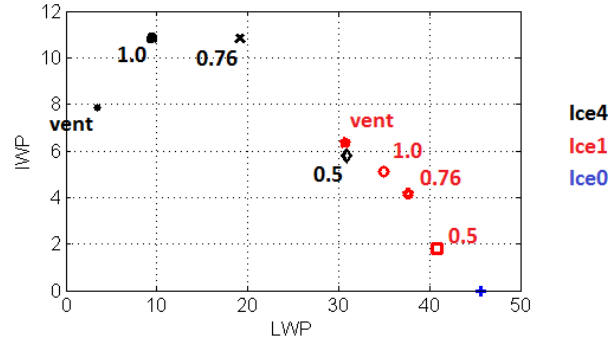


Fig. 3.6.: COSMO's sensitivity to ice concentration and fac_{Γ} . “vent” show runs with enhanced deposition by the full treatment of ventilation effects. For Ice4, ventilation leads to the complete dissipation of the cloud until the end of the simulation.

Also shown in fig. 3.6 is the data point for fac_{Γ} defined to be 1.0. For simplicity, this value will be used for all of the sensitivity tests of chapter 4. The selection of $fac_{\Gamma} = 1$ instead of $fac_{\Gamma} = 0.76$ can be justified the effect of ventilation on crystal growth. Using the full implementation for ventilation (Seifert and Beheng, 2006) based on Beard and Pruppacher (1971) leads to a fac_{Γ} that can be even greater than 1, depending on the Reynolds number and thus on crystal size and sedimentation velocity. To estimate the influence of the previously neglected enhancement, an average vertical profile of fac_{Γ} including ventilation is presented in fig. 3.7. Accordingly, value of 1.0 can be interpreted as a mean value occurring at cloud top.

Fig. 3.6 which shows the sensitivity to varying fac_{Γ} . Although fig. 3.7 shows fac_{Γ} with ventilation included to be close to 1.0 near cloud top, significant differences between “1.0” and “vent” arise. It suggests that LWP does not depend linearly on IWP in the Ice4 run for $fac_{\Gamma} > 0.76$. When it is increased from a value that does not disturb the development of the liquid layer significantly to a higher value that is still small enough to allow for cloud growth, e.g. from 0.5 to 0.76, there is a clear negative correlation between LWP and IWP, as liquid is consumed by the more effective WBF process, leading to larger ice crystals and therefore a higher IWP. However surpassing a certain critical value of fac_{Γ} that causes the reduction of cloud thickness, LWP is still reduced, but IWP does not increase due to decreasing cloud thickness and therefore less ice crystal burden. Additionally, with reduced vertical extent, residence time of a sedimenting crystal within ice supersaturated air is shortened, implying smaller ice crystals which

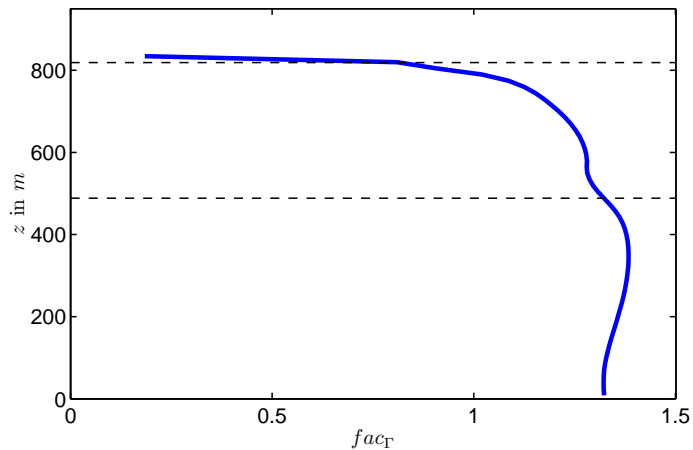


Fig. 3.7.: Typical horizontal mean fac_{Γ} including ventilation. Cloud top and base are indicated by dashed lines. The low values above the mean cloud top are due to horizontal averaging where not all of the gridpoints contain cloud ice.

in turn contribute to a reduced IWP. Consistent with the overall picture shown in fig. 3.3, $fac_{\Gamma} = 0.76$ in combination with $N_i = 4l^{-1}$ is roughly in this critical range.

To sum up, the WBF process strongly influences the results and critically depends on the assumptions on size distributions, ventilation as result of sedimentation, but also on the capacity ice particles as described in section 2.3.1.

3.3.2. Vertical Velocities

Droplet growth in mixed-phase clouds strongly depends on the strength of updrafts (section 2.3.1). Fig. 3.8 depicts that COSMO generally lies at the lower end of the scale when comparing maximum vertical velocities reached in the whole domain. A first idea to identify the reason might be the feedback between LWP and turbulence, and therefore the link to the WBF process. Based on the finding that COSMO's WBF is relatively strong, it can be expected that for the runs including ice, dynamics will be weakened because of consumed liquid water, which is indeed the case.

However, another point of view is possible, interpreting the amounts of liquid and ice as a result of simulated strength of vertical motions, rather than a reason. According to the feedbacks shown in fig. 2.13, it can be expected that with more turbulence being present, the cloud can maintain more liquid water and therefore more ice. Hence, it is interesting to examine the strength of simulated vertical velocities and to ask the question whether there is a reason that could cause a model to simulate weak updrafts, independent of ice interactions.

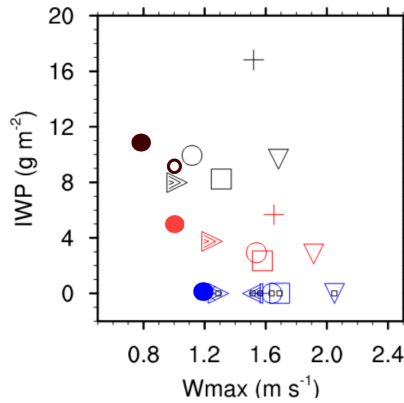


Fig. 3.8.: preliminary intercomparison results. Blue: Ice0. Red: Ice1. Black: Ice4. Different symbols correspond to different models. Courtesy of Mikhail Ovchinnikov, with changes.

According to the spread between the models for the Ice0 run (blue symbols in fig. 3.8), some differences do exist. Since no feedbacks with ice processes are possible, only the right part of fig. 2.13 is relevant, where cloud top cooling induces boundary layer mixing that leads to the growing cloud layer. The LWP cannot explain COSMO's low w_{max} , since for Ice0 it lies right in the range of the results gained by other models (fig. 3.5). Because the parameterization of cloud top radiative cooling has been unified and should be identical among the participating models, also the comparison of cooling rates (not shown) gives no hint that cloud top cooling was lower and therefore responsible for the difference in w_{max} .

Possible reasons affecting w_{max} can be the calculations of the subgrid turbulence scheme as a physical factor, but also purely numerical issues that are responsible for vertical advection, for example. Being optimized for mesoscale simulations where the grid spacing in vertical direction is smaller than in horizontal directions by a factor of 10 to 100, a special numerical treatment of vertical advection is applied in

COSMO. The modified Crank-Nicolson scheme which is an implicit vertical advection scheme (Doms, 2011) helps to save computation time without becoming unstable. Two different implementations of the implicit method are available, where differences concern interactions with the Runge-Kutta time integration scheme. The default setting is called “impl2”, a newer one is called “impl3” and acts outside the Runge-Kutta scheme.

For an LES configuration, the ratio of horizontal to vertical resolution lies below an order of 10, namely 5 in this case. In COSMO, the option to switch to explicit vertical advection with a default order of 3 is offered. This option is called “expl3”.

It was therefore interesting to conduct some further sensitivity tests which could give an idea about the source of different w_{max} . In fig. 3.9, sensitivities when using the different schemes are shown compared to the default using implicit vertical advection. It shall not be discussed here which settings are reasonable and which are not from the numerical point of view, as this is not the intention of this work. For these tests, $fac_{\Gamma} = 1$ was specified. It turns out that changing this treatment causes sensitivities of roughly 10% for both w_{max} and LWP . With ice being present, relative differences of LWP increase. In the plot shown, they are greater than 20% for the Ice4 simulation. For the Ice0 case this means, however, that the improvement relative to the rest of the models is only small, as they are mostly in a range around $1.6ms^{-1}$ compared to about $1.3ms^{-1}$ of COSMO using different numerical settings. The resulting LWP of $50gm^{-2}$ then shifts to the upper range of the model spread (see fig. 3.5).

A further test was to switch off subgrid turbulence causing more intensive updrafts, but also less diffusion of prognostic variables. It can be expected that this test leads to less realistic results with respect to turbulence and mixing. Nevertheless it can confirm the strength of updrafts being a critical parameter to droplet growth in the mixed-phase regime. Also here, the general tendency of differences is increased with ice being present.

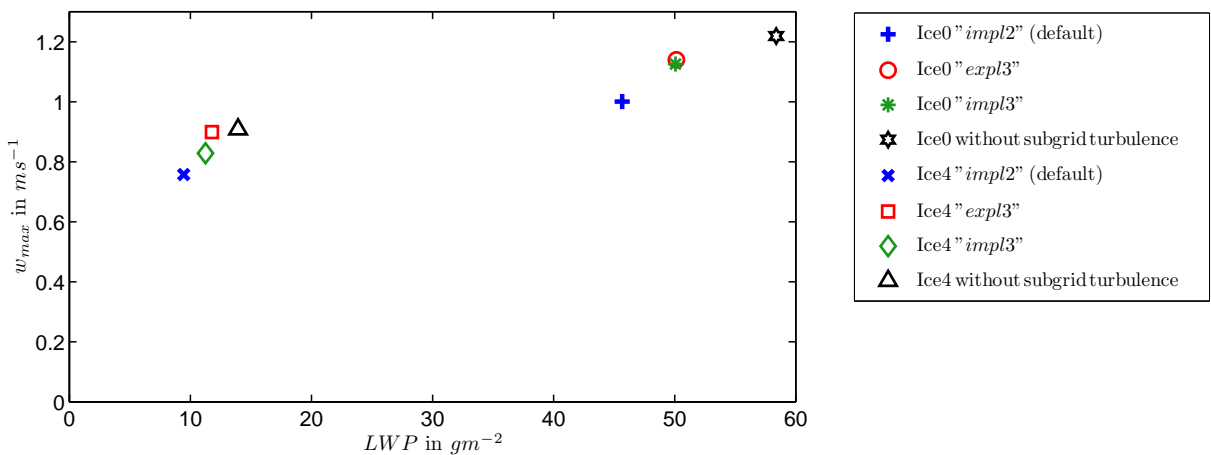


Fig. 3.9.: COSMO’s sensitivity to subgrid turbulence (black: no subgrid turbulence) and different treatments of vertical advection.

3.3.3. Relative Importance of Vertical Velocities and WBF

It was shown that using equivalent crystal size distributions, one can reproduce similar results among the models and that results strongly depend on turbulence induced mixing and vertical motions. It can now be discussed why COSMO using an equivalent fac_{Γ} can produce similar results with respect to LWP and in spite of the fact that w_{max} was found to be significantly smaller than within the three models using the Morrison et al. (2005a) microphysics scheme.

A possible explanation can be the statistical distribution of vertical velocities within the liquid cloud layer. Because in one-dimensional plots (see figs. 3.8 and 3.9) w_{max} is the maximum positive vertical velocity reached within the whole domain, it represents only a single grid point, whereas all other grid points are not taken into account.

If descending air is spatially more concentrated than ascending air, downdrafts must be stronger in order to fulfill the continuity condition. Distributions of vertical velocities in the Ice0 run are presented in fig. 3.10, which shows the asymmetry between ascents and descents. The sharp peak close to zero is most likely related to the cloud top region directly below the temperature inversion (see fig. 3.3), with a smoothly decreasing probability density function towards the strongest downdrafts. In contrast, ascents show a broader local maximum at weak updrafts, decreasing more steeply and therefore reaching lower maximum values of w . In other models, the fractionation might be different, possibly leading to a distribution decreasing more smoothly at positive vertical velocities.

In section 2.3.1, the threshold velocity w^* derived by Korolev (2007) was introduced. Fan et al. (2011) showed for the same ISDAC case as being discussed in this work, that w^* was close to zero, implying

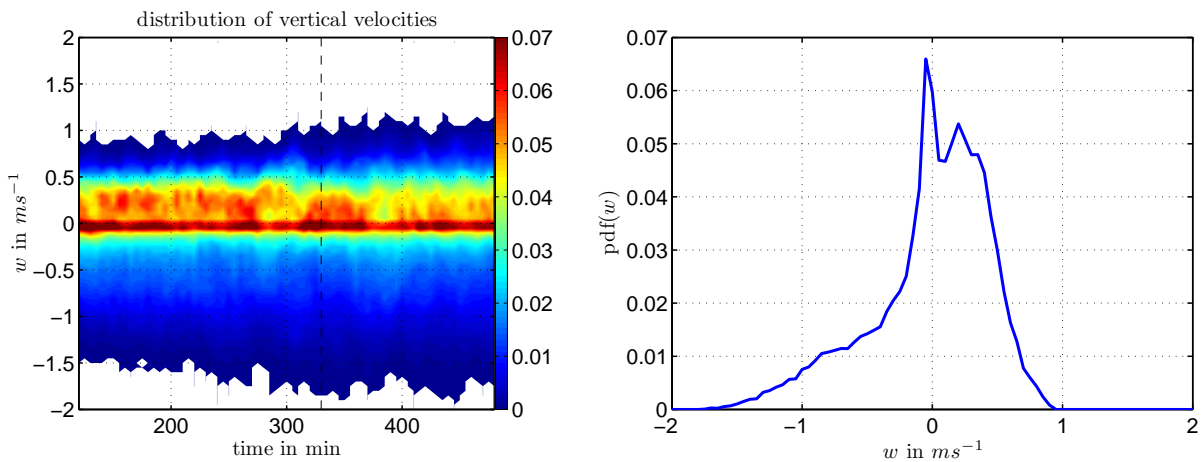


Fig. 3.10.: Probability density function for vertical velocities. For this analysis, vertical velocities of all in-cloud grid points are binned in intervals of $0.05 \frac{m}{s}$ with a total number of roughly 90000 in-cloud values directly after spin-up. The number fraction of each bin greater than 10^{-3} is shown as a time series (left) and in the middle of the averaging interval (right) which is indicated by the vertical dashed line on the left-hand side.

that already weak updrafts can deactivate the WBF process because both, droplets and ice crystals can grow in this regime (“both-grow regime”). Hence, in order to describe the model’s ability to either maintain the cloud layer or dissipate it due to the WBF process, a statistical analysis of vertical velocities occurring within the cloud would be necessary, and the intercomparison of probability density functions for velocities occurring in the models would be an interesting aspect for a further characterization of the models’ dynamics.

4. Sensitivity to the Treatment of Ice Nucleation

For simulations in the framework of the Model Intercomparison (chapter 3), ice concentrations were prescribed to be constant regardless of temperature, provided that a certain amount of liquid water as well as moderate supersaturation with respect to ice is present (see eq. 3.10). This idealization shall now be dropped in order to get an idea of how COSMO's default parameterization behaves, as well as the dust immersion freezing parameterization recently developed by Niemand et al. (2012) and an estimation for the ice activity of bacteria.

First, base concentrations of dust and bacteria will be discussed, as well as the range of concentrations used for sensitivity tests (section 4.1). Second, changes in the model setup will be summarized shortly in section 4.2. Third, ice initialization methods and the effect of IN depletion will be discussed in sections 4.3 and 4.4.

Then, a comparison of COSMO's default parameterization by Phillips et al. (2008) and Niemand et al. (2012) is described. They will be called PH08 and NI12 hereafter.

After that, several combinations of concentrations for the two IN species will be used in two temperature regimes, one representing ISDAC conditions and one being 5°C colder. This will give an estimate on how much aerosol would be needed to reach ice number concentrations observed during the ISDAC campaign as well as "critical concentrations" which would cause the cloud's dissipation.

A final radiation sensitivity test in section 4.9 will show the correlation between the thermal heating rate calculated by the model and liquid water/ ice contents.

4.1. Concentrations Applied for Sensitivity Tests

A major component of the IN on April 26 was mineral dust (McFarquhar et al., 2011). Aerosol concentrations based on measurements during April 8-9 were derived by Liu et al. (2011). The measurements were conducted using a Passive Cavity Aerosol Spectrometer Probe (PMS PCASP-100X) for sizes from $0.11\mu\text{m}$ to $3\mu\text{m}$ and a Forward Scattering Spectrometer Probe (PMS FSSP-300) for sizes from $0.3\mu\text{m}$ to $20\mu\text{m}$. Earle et al. (2011) characterized the aerosol loading on April 8 and April 26 to be similar, finding relatively clean conditions in both cases. Also the observed clouds, namely liquid-dominated low-level single-layer stratocumulus, were similar in both cases. Therefore also the same dust concentrations and distributions are assumed for flight 31 as given by Liu et al. (2011) for April 8-9. For their simulations, they prescribed the coarse mode parameters of a lognormal distribution with $D_g = 1.1\mu\text{m}$ for the median

diameter and $\sigma_g = 2.35$ for the standard deviation. The total aerosol number in the coarse mode was $N_a = 5.0\text{cm}^{-3}$ with dust contributing 5%.

Therefore the base dust concentration in this work is 0.25cm^{-3} . Overall dust concentrations used for the sensitivity runs in this chapter are in a range from 0.025cm^{-3} to 375cm^{-3} . For comparison, the simulations of Bangert et al. (2012) yielded dust number concentrations up to an order of 100cm^{-3} during a Saharan dust event over western Europe. Therefore the maximum concentrations used for sensitivity studies may not be representative in the remote Arctic regions, since already the “dust20” run would mean that all of the coarse mode aerosol observed on April 8 2008 consisted of dust only. Nevertheless, variations in time and space are common, since the Arctic can be affected by long range dust transport originating from the North American and Eurasian continents (Curry et al., 1996). The “Arctic haze” occurring in Arctic winter is caused by the transport of aerosols originating from the midlatitudes (Barrie, 1986).

Tab. 4.1.: Aerosol concentrations in cm^{-3} and model run names explicitly mentioned in this chapter.

base dust	dust10	dust20	dust30	dust60	dust100	dust200	dust1000	dust1500
0.25	2.5	5.0	7.5	15	25	50	250	375
base bacteria	bac0.1	bac5	bac10	bac20	bac50	bac100		
0.01	0.001	0.05	0.1	0.2	0.5	1.0		

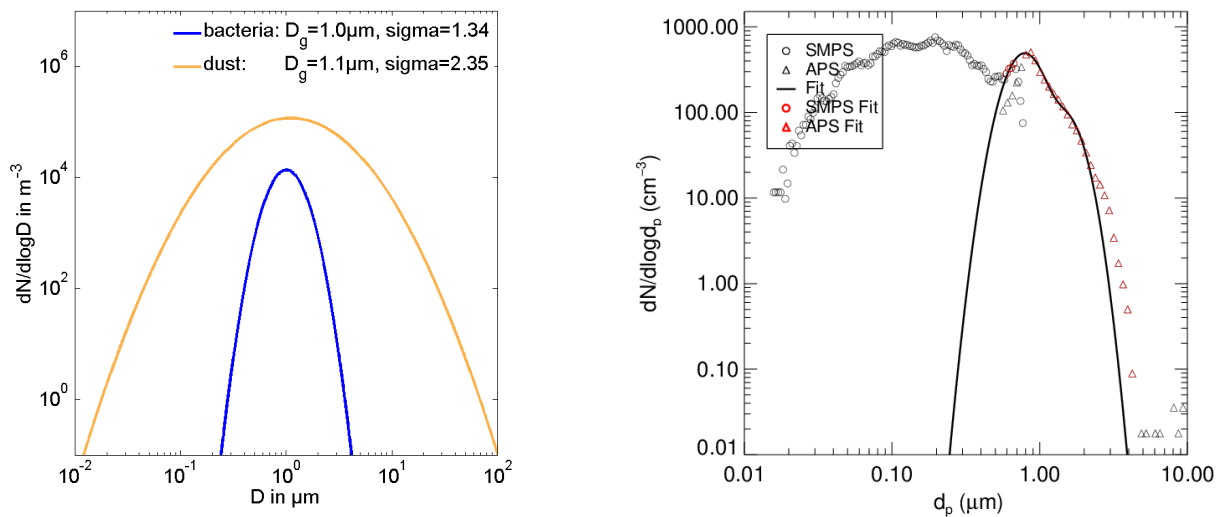


Fig. 4.1.: Left: Size distributions for ice nucleation active bacteria (0.01cm^{-3}) and mineral dust (0.25cm^{-3}). Right: typical size distribution of ice nucleation active bacteria measured in the AIDA chamber. Courtesy of Caroline Oehm.

As for dust, the size distribution of bacteria needs to be specified to be able to apply the n_s -approach. Median diameter and standard deviation are estimated by a unimodal lognormal distribution fitted to measurement data from experiments in the AIDA cloud chamber, assuming spherical particles. The median diameter $D_g = 1.0\mu m$ and a standard deviation $\sigma = 1.34$ are used in the following, which results in a relatively narrow peak compared to the dust size distribution (fig. 4.1).

Concentrations of bacteria in the atmosphere in general are not well known (Murray et al., 2012; Després et al., 2012; Burrows et al., 2009b), which is especially true for variations in time and space. For the Arctic region, measurements exist by Jayaweera and Flanagan (1982) who report the highest inside-cloud concentration of total bacterial cells to be $10l^{-1}$. Therefore, a base concentration is estimated to be $0.01cm^{-3}$, whereas concentrations described in this work are always meant in the sense of of the ice nucleation active fraction of total bacteria occurring in the atmosphere, i.e. $N_{bac} = f_{INA} N_{bac,tot}$ (see section 2.2.2). Therefore, results will be independent of f_{INA} which is only needed to relate the findings to a total amount of bacteria.

Compared to global mean values derived by modeling (fig. 4.2; Burrows et al. (2009b)), this estimation is in the range of possible values at northern Alaska, if f_{INA} was around 0.1 (Burrows et al., 2009b).

The range of bacteria concentrations used for sensitivity runs are in a range from 10^3m^{-3} to 10^6m^{-3} .

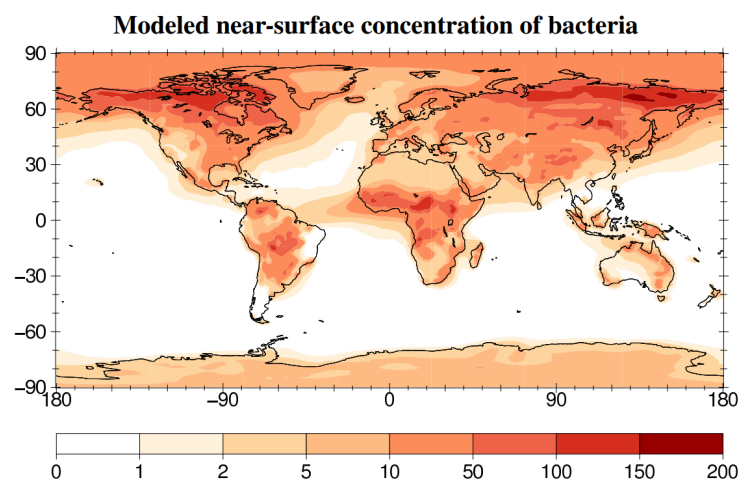


Fig. 4.2.: Bacteria concentration near surface in l^{-1} modeled by Burrows et al. (2009b). Their results suggest 10-100 l^{-1} at the North Slope of Alaska.

4.2. Model setup

The overall model setup is very close to the setup described in chapter 3 for the model intercomparison. Differences concern the following points:

- Application of an ice nucleation parameterization instead of eq. 3.10, depending on different aerosol concentrations
- Resolutions are reduced to $\Delta x = \Delta y = 100m$; $\Delta z = 15m$; $\Delta t = 2s$ with the same number of grid-points in horizontal directions in order to save computation time. Differences were found to be small when directly comparing this setup to the finer grid used in chapter 3.
- Specification of a more effective WBF process with $f_{ac\Gamma} = 1$, corresponding to a ventilation effect for crystals near cloud top (see section 3.3.1)
- Because the parameterizations tested in this work assume that heterogeneous freezing is representable by the singular hypothesis, the implementation of the stochastic freezing parameterization (Bigg, 1953b,a) is neglected for all of the sensitivity tests discussed here. It turned out that results were practically not affected when including the stochastic approach additionally.

4.3. Treatment of Ice Initialization

This section will show the influence of different ways to initialize ice processes, since the results of an idealized model setup strongly depend on the initialization procedure. Therefore, it is distinguished between two approaches here. First, simply switching on ice after spin-up is shown to be problematic especially with aerosol concentrations close to critical values leading to dissipation of the cloud. The second approach accounts for depleted IN already before ice nucleation is switched on, leading to a simulation that starts near its quasi equilibrium state.

Because during spin-up no ice may be present, neither ice nor depleted IN are present in the cloud as well as below the cloud (left part of fig. 4.3). When switching ice on after two hours of spin-up using the first approach, the behavior is similar to section 3.2.2, i.e. mixing of air without depleted IN from below the cloud causes high nucleation rates at cloud base. With time, the concentration of depleted IN below cloud base increases due to mixing and after roughly one hour their number density adjusts towards an equilibrium state adjacent to cloud base (upper left plot of fig. 4.3). This adjustment of IWP towards its equilibrium needs more time, since IWP also accounts for the amount of crystals below the cloud. As it takes some more time until the initially formed ice particles have sedimented completely, the peak of IWP reaches its equilibrium state after two hours (fig. 4.4), i.e. after four hours of total simulation time. The initial burst of ice nucleation can be interpreted as unnatural source, because this kind of initialization would correspond to infinitely steep concentration gradients if IN are assumed to be advected, so that

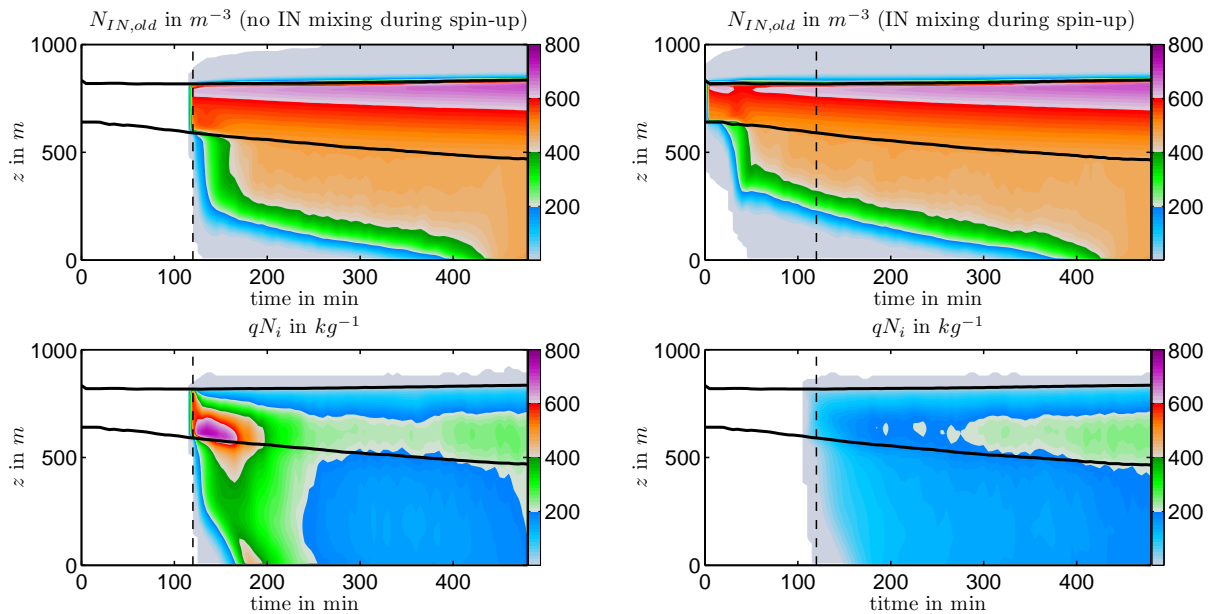


Fig. 4.3.: Differences in ice initializations with a simple treatment on the left and more realistic results on the right, where depleted IN already exist before the initialization of ice.

both, in-cloud air and below-cloud air would be filled with unactivated aerosol at once. This situation is shown on the left of fig. 4.3.

In order to avoid such behavior, depleted IN were implemented in a way that they are already mixed during spin-up. This means that ice formation is calculated in order to derive $N_{IN,old}$, but no ice is explicitly formed in the model for the first two hours. This causes the distribution of depleted IN to start closer to an equilibrium state than it does with the initialization described before, therefore avoiding the initial peak of ice formation (right part of fig. 4.3).

Figure 4.4 shows the direct comparison of the two possibilities with respect to LWP and IWP, where the upper row belongs to the situation of fig. 4.3 with low ice number concentrations. Differences in LWP are marginal in this case, but the tendency is less liquid water being conserved in the “unrealistic” treatment, as the initial ice peak consumes more water on the one hand, but also weakens dynamics by water depletion on the other hand. Therefore the difference in LWP persists until the end of the simulation. In contrast, the IWP as well as the ice crystal burden (not shown) converges after two hours, when the initial spill-over of crystals has left the boundary layer by sedimentation.

It must be pointed out that the case discussed here is a sensitivity run using the Phillips et al. (2008) parameterization and a base dust concentration of 0.25cm^{-3} . Resulting ice concentrations of 0.2l^{-1} are relatively low compared to the ones presented in chapter 3, implying that also the described ice burst has only a small effect with respect to LWP. The situation is different for amounts of IN shortly below critical concentrations as shown in the lower row of fig. 4.4. It shows sensitivity runs with the base dust concentration multiplied by a factor of 20 and 30, respectively, resulting in persistent cloud layers using the equilibrium initialization. With the finding that the initial burst yields much higher ice

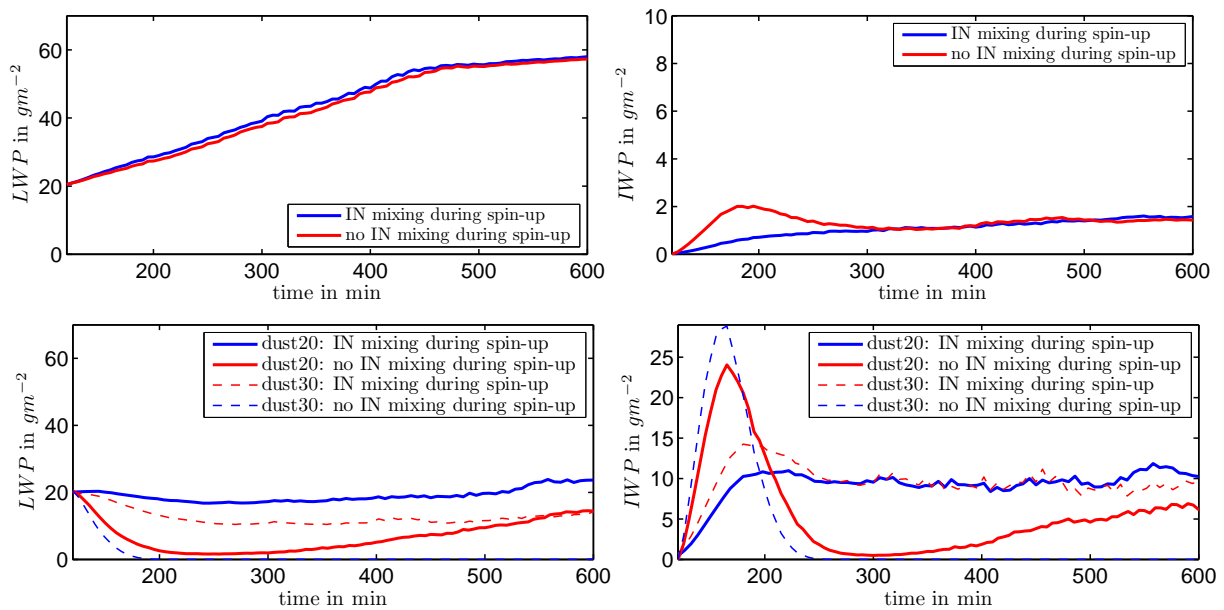


Fig. 4.4.: Results of LWP and IWP for different initialization methods.

concentrations than are present in the equilibrium state, this treatment can be expected to immediately dissipate the cloud in the beginning, although an equilibrium cloud could potentially be maintained. For “dust20”, differences in LWP and IWP are very high, with an almost complete dissipation of the cloud when using the non-equilibrium initialization method. Only after some time, dynamics are reinforced and both, LWP and IWP increase towards the equilibrium run. With “dust30”, the cloud is depleted after 1.5 hours, although equilibrium amounts of LWP and IWP of the persistent cloud average out at $15 \frac{g}{m^2}$ and $10 \frac{g}{m^2}$, respectively.

These findings justify the use of IN-mixing during spin-up for all of the further sensitivity runs. Nevertheless the question arises about the degree of mixing needed to gain results as close to nature as possible. As discussed, the more depleted IN present, the less new nucleation can occur. This means that assumptions about the mixing state have to be made, which was in this case simply defined by the spin-up period. Here, a reservoir of available IN remains in the lower half of the boundary layer which is slowly consumed during simulations depending on the strength of turbulence.

4.4. Comparison of Default Nucleation Scheme and IN Depletion Scheme

With the treatment described above, it is now possible to intercompare the nucleation scheme accounting for IN depletion and COSMO’s default treatment of the two-moment scheme (see section 2.2.3). In the default scheme it is not possible to avoid the initial ice burst, making the comparison to the results of the depletion scheme not comparable one-to-one. However, as described above, for cases with IN concentrations well below their critical values, ice number concentrations converge after two hours of ice initialization, so the comparison with respect to ice is possible despite of the initial difference. Because the parameterization of Phillips et al. (2008) is used by default in the two-moment microphysics of COSMO, it is also the basis for the comparison conducted in this section.

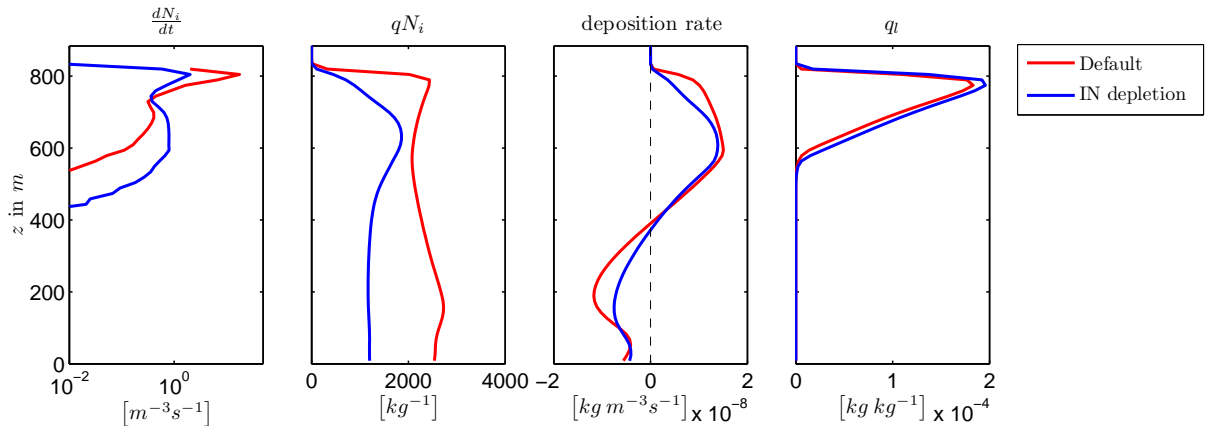


Fig. 4.5.: Mean vertical profiles averaged from hour 5 to hour 6 for the dust10 sensitivity run. Red shows the results using the depletion scheme with prognostic $N_{IN,old}$, blue results from the default scheme.

The main effects are evident from the ice nucleation rates (in the sense of ice formation rates, hereafter) depicted in fig. 4.5 which shows a case using a base dust concentration multiplied by a factor of 10, such that the resulting ice number concentration is around $2l^{-1}$, resulting in a persistent cloud. As it was pointed out in section 2.2.3, the default ice nucleation treatment produces many crystals especially near cloud top due to sedimentation, yielding rates 10 times as high as resulting from the depletion scheme. Nevertheless, also the depletion scheme shows its maximum near cloud top caused by the dependence on temperature on the one hand, and by the entrainment of unactivated IN from the free atmosphere on the other hand (see concentrations of $N_{IN,old}$ above the cloud in fig. 4.3).

Also the vertical structures below cloud top differ between the two versions. As most of the nucleation occurs at cloud top in the default scheme, calculated N_{IN} in levels below can rarely exceed the number of ice crystals present which were created at cloud top, resulting in very low nucleation rates. Accounting for $N_{IN,old}$ yields a more constant nucleation rate with height with a local maximum near cloud base which arises from the entrainment of IN from the boundary layer.

The vertically integrated ice nucleation rate is roughly two times higher when using the default scheme, although the nucleation of the depletion scheme is greater near cloud base. This results in a higher ice crystal burden which in general leads to earlier glaciation of the simulated cloud when using the default scheme. Fig. 4.5 also shows the vertical profiles of N_i . The higher amounts especially near cloud top result in higher ice mass deposition rates in these regions and finally in a lower amount of liquid water.

In the case shown here, differences in q_i are still moderate during the period of averaging between hour 5 and 6. However, the transition regime, i.e. the shift from IN concentrations resulting in a persistent cloud to concentrations resulting in a dissipated cloud, is narrower when the default scheme is applied. This is mainly caused due to the unphysical link between the sedimentation effect and nucleation which does not allow a negative feedback for nucleation, as sedimentation continuously proceeds. In contrast, with the depletion scheme, an initial ice burst is directly followed by suppressed ice formation rates, which can only be reinforced by mixing, therefore being implicitly linked to droplet growth in updrafts which allows the redevelopment of the cloud.

Whereas the cloud shown in fig. 4.5 is persistent in both schemes (dust10), the situation is different in the upper plot of fig. 4.6 (dust20). It shows the evolution of the two runs with respect to LWP and IWP. Directly after the spin-up, the LWP is $20gm^{-2}$ and the IWP increases due to ice crystal growth. In this case, the default scheme is not able to sustain the cloud, with both LWP and IWP converging to zero. In fig. 4.6 (b), a whole set of simulations is shown. For base dust concentrations, the difference between the default and the depletion scheme is close to zero, as ice does not have a big influence in this case (lower right curves). In the dust10 runs, differences in N_i (see fig. 4.5) modify the cloud significantly. Equilibrium LWPs differ by about $10gm^{-2}$, whereas no difference in the IWP exists, although more crystals are present. This indicates that the primal source of additional N_i in the default scheme is due to nucleation when crystals are smallest and therefore make only a little contribution to IWP. Differences between the schemes increase with increasing IN concentrations. The transition from persistent to a dissipated cloud

occurs in the range between dust10 and dust20 (see table 4.1) with the default scheme whereas the depletion scheme reaches its “point of no return” only when exceeding dust50. For concentrations between dust20 and dust50, it shows its characteristic reinitialization of dynamics and a growing cloud towards an equilibrium state after an initial weakening.

In order to estimate the influence of ice initialization and the initial peak which can be avoided in the depletion scheme, the results of fig. 4.4 can be used once again. Using the peak initialization there showed that the critical concentration was between dust20 and dust30, which is a factor of two higher than what was found when using the default scheme. Therefore the different results of default and depletion scheme can clearly be related to the use of prognostic $N_{IN,old}$.

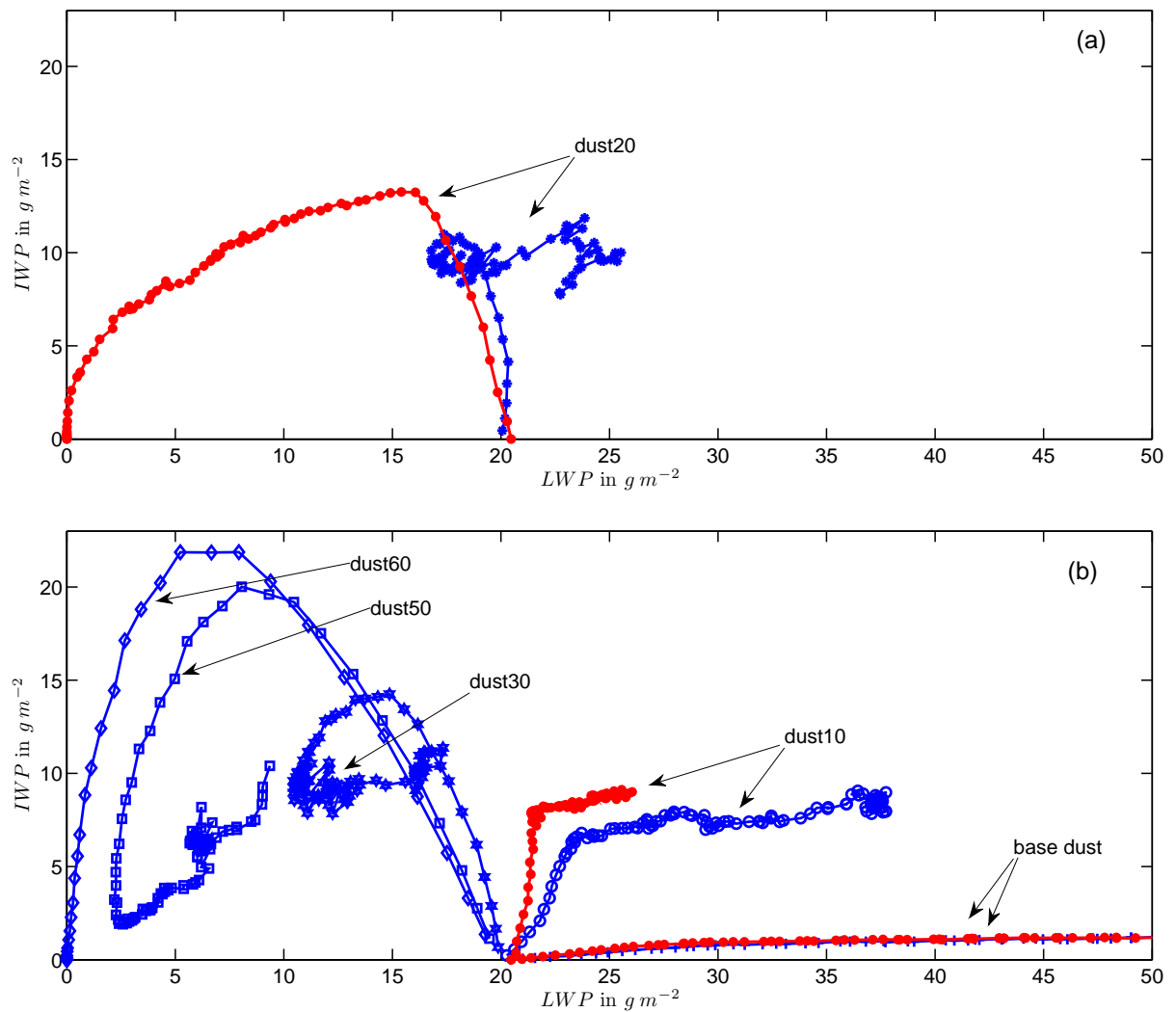


Fig. 4.6.: a) Default (dissipating) vs. depletion scheme (persistent) for the “dust20” run using the PH08 parameterization. b) Default scheme (red) for base dust, dust10, dust20. Depletion scheme for base dust, dust10, dust20, dust30, dust50, dust60. The “critical concentration” is between dust10 and dust20 with the default scheme, and between dust50 and dust60 when accounting for depletion.

For the meteorological conditions found during ISDAC flight 31, the equilibrium state can be estimated from fig. 4.6 in a range of LWP between $10 \frac{g}{m^2}$ and $20 \frac{g}{m^2}$, where the IWP ranges from $8 \frac{g}{m^2}$ to $10 \frac{g}{m^2}$. Using the depletion scheme with the nucleation parameterization by Phillips et al. (2008) and assuming immersion freezing with mineral dust as IN was the only nucleation mechanism, a dust concentration between 1 cm^{-3} and 10 cm^{-3} would be needed to maintain the equilibrium state, which is a factor of 4 to 40 higher than estimated by Liu et al. (2011). The discussion of desert dust concentrations will be given in section 4.7, where discrepancies will be even greater when using the NI12 parameterization.

4.5. Depleted Ice Nuclei with and without Transport

The intention of this section is to show that vertical mixing by advection and turbulent diffusion greatly impacts the result. Therefore it is not possible to simply use a diagnostic variable for the representation which would reduce computational costs and the complexity of the model code. Hence, in contrast to the prognostic treatment of $N_{IN,old}$ with transport, $N_{IN,old}$ without transport is not affected by advection and the turbulent diffusion.

For this comparison, also the original PH08 parameterization was used. Without transport, neither the entrainment of $N_{IN,old}$ from the boundary layer nor from the free atmosphere is possible, since its value is only changed locally by the source term in case of a freezing event. Due to the lacking entrainment, reduced ice formation rates especially near cloud base can be expected.

Figure 4.7 shows the situation for two periods of averaging, period one from hour 5 to hour 6 and period two from hour 7 to hour 8. The overall picture of smaller ice nucleation rates and smaller ice number concentrations fits the expectations. However, especially at earlier times of the simulation, there is a peak of ice production near cloud base. Considering the height of the mean cloud base as defined by

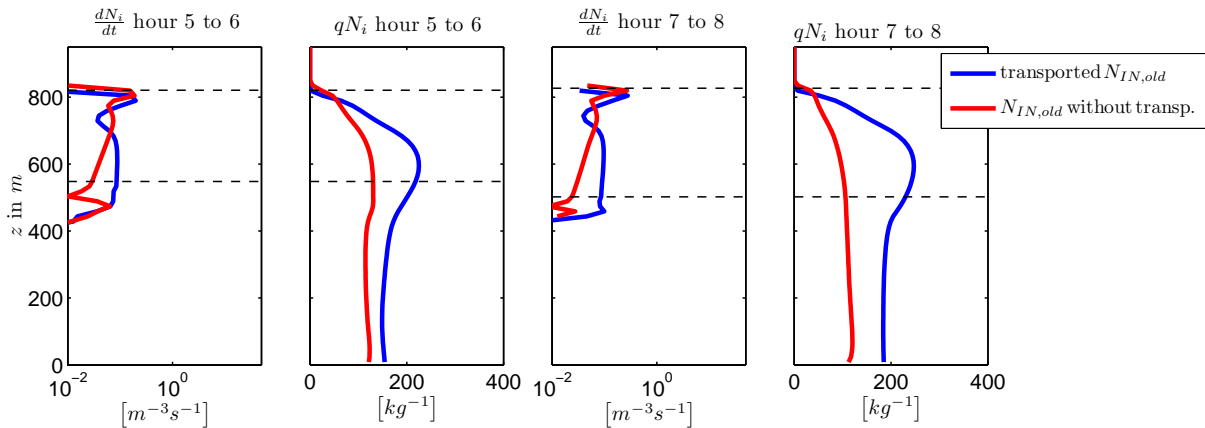


Fig. 4.7.: Comparison of ice formation rates and ice number concentrations between depleted IN with and without transport. Dashed lines indicate cloud top and cloud base, respectively.

the black lines (see fig. 4.9, for example), this peak is found even below the mean cloud base. In the end of the simulation (period two), the peak becomes negligible, resulting in even larger qN_i .

Since a spread of $N_{IN,old}$ can be ruled out, a possible explanation can be the spread of the cloud itself. The test described in this section was conducted using the base dust concentration which results in a small ice number concentration and a vertically growing cloud layer, in particular shifting the cloud base to lower levels. By definition, before being incorporated into the cloud volume, $N_{IN,old}$ is zero in such areas, resulting in large freezing events when this part of the model domain becomes part of the cloud.

With this test, it becomes apparent what is the cause of the local minimum of ice formation in case of using prognostic $N_{IN,old}$. Since this minimum is not there in the diagnostic version of $N_{IN,old}$, it must be the result from the effect of transportation, with $N_{IN,old}$ produced at cloud top suppressing ice formation in adjacent levels below.

4.6. Comparison of Phillips et al. (2008) and Niemand et al. (2012)

In this section, the curves derived for natural desert dust (NI12) and the “DM” species of PH08 (see section 2.1.4) are compared using several different dust concentrations. Figure 2.4 presents the temperature dependent active surface site densities, with a stronger temperature dependence of the NI12 function. In the temperature range relevant for ISDAC flight 31, namely from -12°C to -15°C within the cloud layer with coldest temperatures directly below the capping inversion, the function for immersion freezing of pure dusts has the lowest values. Compared to PH08, the difference is more than one order in magnitude. Since the total fraction of ice is approximately proportional to n_s (eq. 2.11), also the number of ice particles is expected to be smaller by a similar factor.

Besides absolute values of n_s , differences in the steepness of the function causes varying results. The reason is that the formation of additional crystals when cooling a parcel of air containing potential IN is determined by the difference between n_s before and after cooling, Δn_s . There are two sources of cooling. First, cooling of the total cloud layer by longwave radiation emission (see fig. 4.8). It acts on a long time scale and is only small in magnitude. Using eq. 2.12, the change of N_i with time is

$$\frac{dN_i}{dt} \approx S_{tot} \frac{dn_s}{dT} \frac{dT}{dt} . \quad [4.1]$$

For example, using NI12 in a dust200 run, the corresponding ice formation rate accounts for an order of $10^{-1} m^{-3} s^{-1}$ with $\frac{dT}{dt} \approx O(10^{-5} K s^{-1})$. The contribution to the total nucleation is small, as mean ice formation rates account for up to $10^1 m^{-3} s^{-1}$ near cloud top. Therefore, the main source of cooling is found within updrafts because of adiabatic cooling.

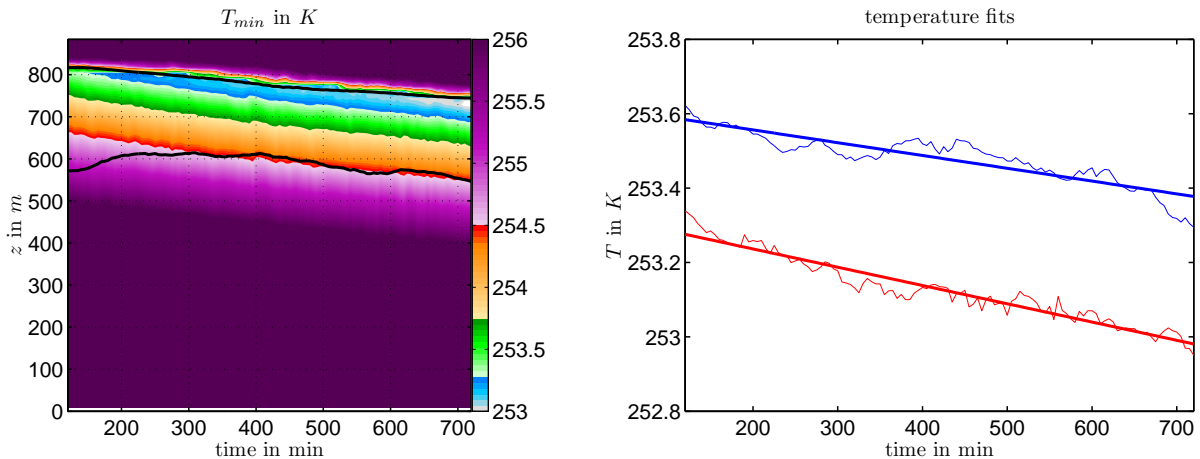


Fig. 4.8.: Left: Temporal evolution of the domain-wide minimum temperatures. Right: Mean cooling rate throughout the simulation determined by linear fits to horizontal mean and minimum temperatures within the coldest cloud layer below the capping inversion, used in eq. 4.1.

Figure 4.9 (a, b) compares the time evolution of ice production rates, with temperature dependencies manifesting in different vertical distributions. Using NI12, they are very low near cloud base at warmer temperatures and show a sharp maximum near cloud top at the minimum temperatures of the cloud layer. The time evolution of NI12 nucleation rates show a stronger decrease, resulting in nucleation which occurs only at cloud top in the end of the simulation. At this stage, cloud base entrainment is too ineffective to fulfill the condition $\Delta n_s > 0$, because on the one hand the boundary layer content of potential IN is mostly depleted and on the other hand in-cloud mixing of $N_{IN,old}$ from cloud top suppresses nucleation below cloud top. Additionally, in lower cloud layers with warmer temperatures than at higher levels, differences in n_s are higher between the levels for NI12 than for PH08 due to the different steepnesses of n_s . Over all, the only important source in this case is cloud top entrainment of IN. Compared to a realistic situation, this is a plausible scenario, as emissions of mineral dust in the vicinity of an AMPC cannot be expected, which would feed the cloud from cloud base. In contrast, long range transport of particles emitted in continental regions is needed to provide dust IN in AMPC, implying that dust is mainly entrained from the free atmosphere into the cloud.

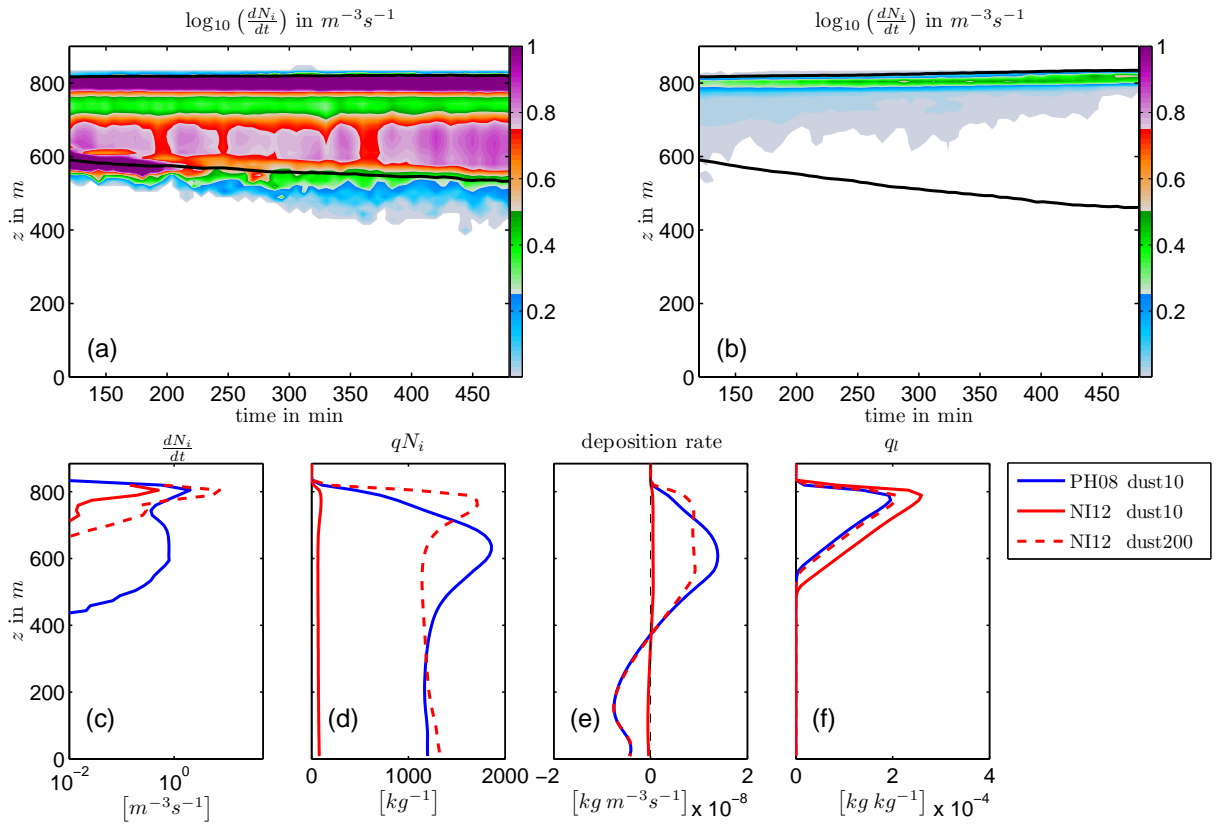


Fig. 4.9.: Nucleation rates for base dust concentrations. Top Left: Phillips et al. (2008) parameterization. Top Right: Niemand et al. (2012) parameterization. Mean vertical profiles averaged from hour 5 to hour 6 for the dust10 sensitivity runs. The blue curves are the same as in fig. 4.5 for comparison to the Niemand parameterization, which yields ice crystal numbers smaller by more than one order in magnitude.

Temporally averaged profiles in fig. 4.9 (d, e) show the resulting ice number concentrations and interactions with the liquid phase, which finally yield a thicker liquid cloud with NI12 for the same concentration of aerosols. The comparison of qN_i shows a maximum near cloud top, which is shifted upwards relative to PH08. Since the only source of new crystals is directly near cloud top in this case, concentrations below the region of ice formation are most likely diluted by mixing, so that the maximum can only be kept up due to locally concentrated ice formation. Moreover, the NI12 deposition rates are enhanced near cloud top and decrease towards cloud base relative to PH08. It might be expected that more consumption of liquid in top layers tends to dissipate the cloud more effectively, as gradients of $LWP(z)$ and therefore the magnitude of longwave radiation emission are potentially weakened to a greater extent. However, vertical mixing seems to be able to suppress this effect, resulting in a similar vertical structure of liquid water content when comparing the PH08-dust10 and NI12-dust200 runs (fig. 4.9 (f)).

It is now evident that, with less effective dust ice nuclei at warmer temperatures using NI12, the observed ice concentrations which were greater than $0.2l^{-1}$ (see section 4.7) can neither be explained with the estimated base dust concentration (see section 4.1), nor using the tenfold amount as shown in fig. 4.9. Therefore some sensitivity runs were conducted with increasing concentrations up to amounts that resulted in a dissipated cloud. For such cases, concentrations greater than $N_{dust} = 250cm^{-3}$ are necessary, corresponding to more than a factor of 1000 greater than the base dust assumption. For comparison, the total aerosol number concentration in the coarse mode as given by Liu et al. (2011) was $5cm^{-3}$ (see section 4.1). A compilation of all sensitivity runs is shown in fig. 4.10.

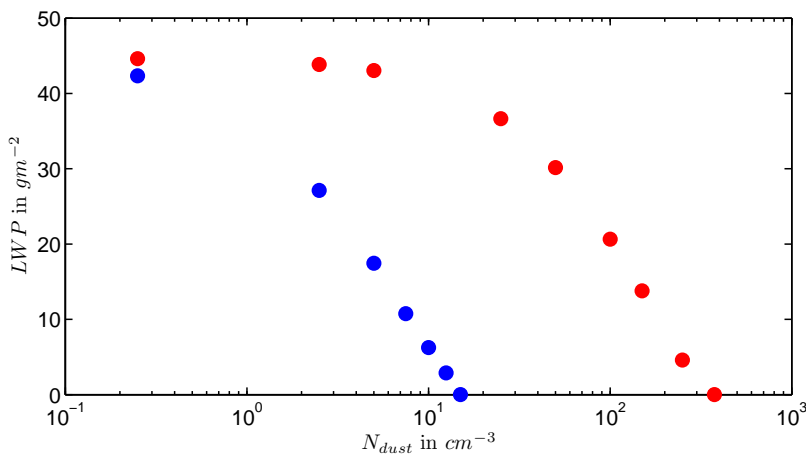


Fig. 4.10.: Mean LWP for varying dust concentrations. Blue: Phillips et al. (2008) parameterization. Red: Niemand et al. (2012) parameterization. The averaging time period is from hour 5 to hour 6, concentrations range from base dust to dust60 (PH08, blue) and dust1500 (NI12, red).

4.7. Dust vs. Bacteria as IN species

Since pure dust was identified to be not an ice nucleus efficient enough in the considered case, this section will present a number of sensitivity runs, including an additional species of IN, namely bacteria which were introduced in section 2.2.2. They are treated independently from the dust species with respect to $N_{IN,old}$, i.e. depleted IN from the bacteria species are represented by an additional prognostic variable. As for the dust-only scenario, several combinations of IN concentrations of both dust and bacteria will yield an estimate on the concentrations needed for a cloud remaining in a stable state with respect to its evolution in time.

To introduce the effect of bacteria on AMPC, vertical profiles are compared to the ones from previous sections (fig. 4.11), taking into account the shape of $n_s(T)$. As demonstrated for pure dust, also using the base concentration of bacteria results in a lower ice number concentration compared to ISDAC flight 31, but discrepancies are smaller than observed when using NI12.

Running the model with a tenfold base concentration, called “bac10”, the vertical distributions (fig. 4.11) are similar to those resulting from PH08-dust10. Because of the slightly steeper $n_s(T)$ for bacteria, the nucleation rate tends to be less near cloud base and greater in the upper half of the cloud. It has to be kept in mind, however, that absolute number concentrations are different. In numbers, absolute values of the “bac10” run (0.1cm^{-3}) are below those of “dust10” run (2.5cm^{-3}), given the greater $n_s(T)$ of bacteria between -12°C and -15°C .

Since this section is intended to derive relative importances of dust and bacterial particles, fig. 4.12 shows a whole set of simulations using different combinations of both aerosol species. For three different periods of averaging, LWP, IWP and mean in-cloud N_i are color-coded, whereas every single black dot indicates one simulation related to the specific choices of dust concentration N_{dust} and bacteria concentration N_{bac} . Thus, areas between black dots are gained by interpolation. Period 1 (first row of fig. 4.12)

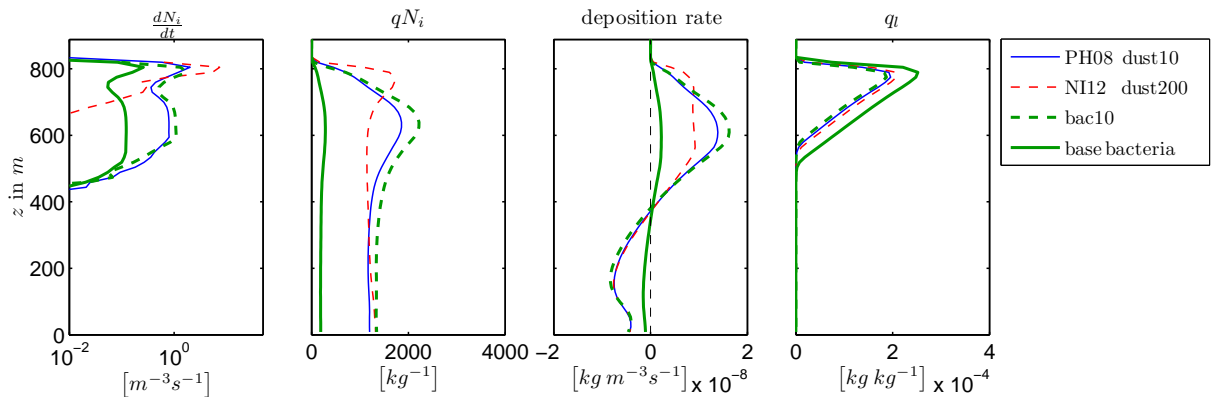


Fig. 4.11.: Vertical profiles for averaging period 2, corresponding to fig. 4.9. Sensitivity tests are shown for runs with increased IN concentrations which yield a persistent cloud.

4. Sensitivity to the Treatment of Ice Nucleation

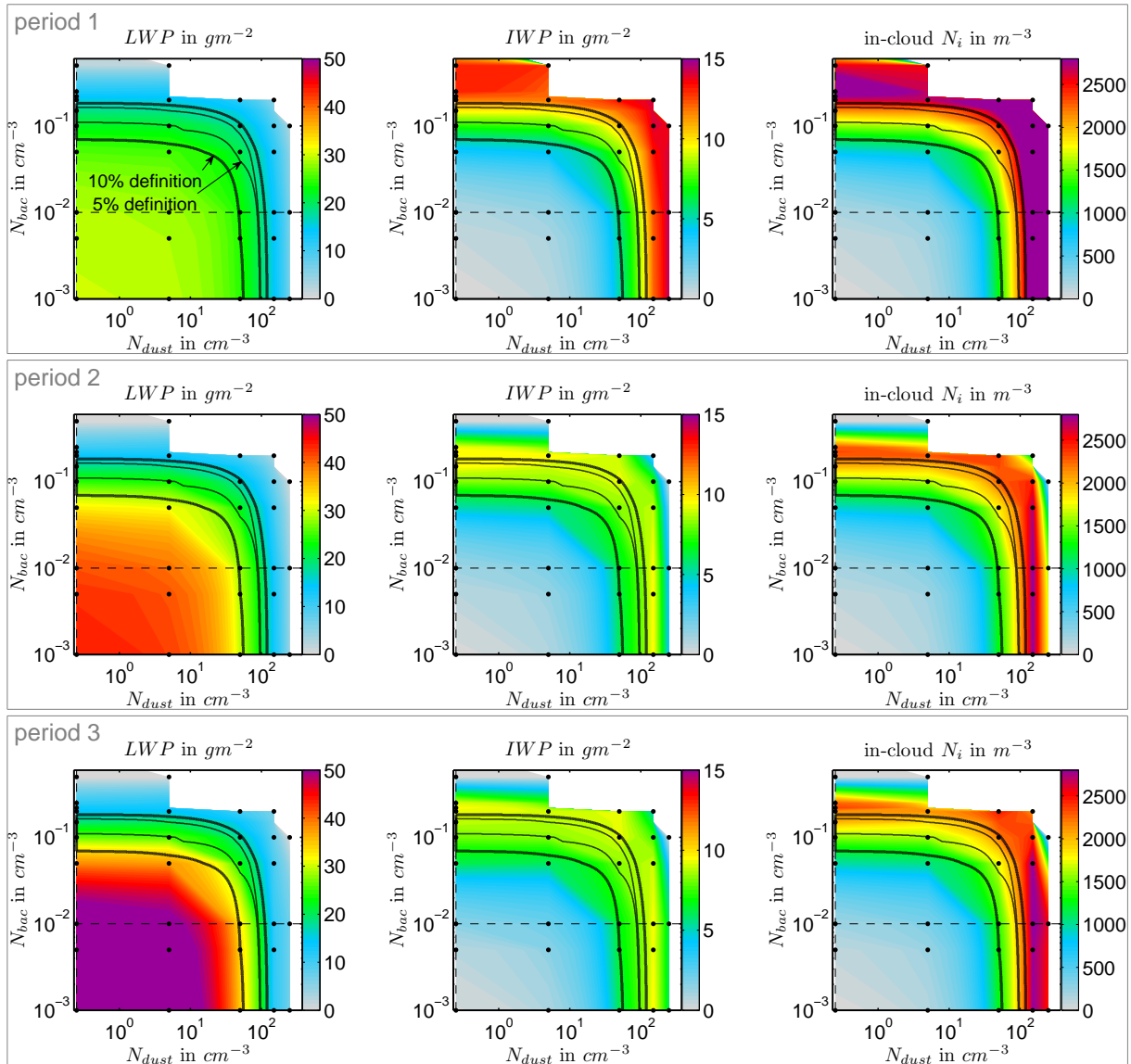


Fig. 4.12.: Summary of LWP, IWP and vertically averaged in-cloud N_i of sensitivity tests depending on different aerosol concentrations. Mean values are shown for period 1 (first row, hour 3-4), period 2 (second row, hour 5-6) and period 3 (third row, hour 7-8). Black dots indicate the single model runs, colored areas are interpolated. Black frames highlight the “transition regime” and dashed lines indicate base concentrations (base dust concentration is equal to the minimum N_{dust} . By definition, the temporal changes of LWP and IWP within the transition regime are close to zero. For this plot, relative changes of 10% are allowed (see text). In general, extensive cloud growth defines the lower concentrations of the transition regime (pink area of the lower left figure, and an initial peak in ice particles defines upper limits of concentrations (pink area of the upper right figure).

is from hour three to four, period 2 (second row) from hour 5 to 6 corresponding to the averaging method used in all previous sections, and period three (third row) shows hour seven to eight.

Growing clouds and hence large LWP are located in the lower left corner, whereas dissipated clouds with LWP approaching zero can be found for increasing N_{dust} and N_{bac} .

Additionally, areas surrounded by black lines indicate the transition area from a “growing-cloud” regime to an “oscillating-cloud” regime. The growing regime is found for small IN concentrations cor-

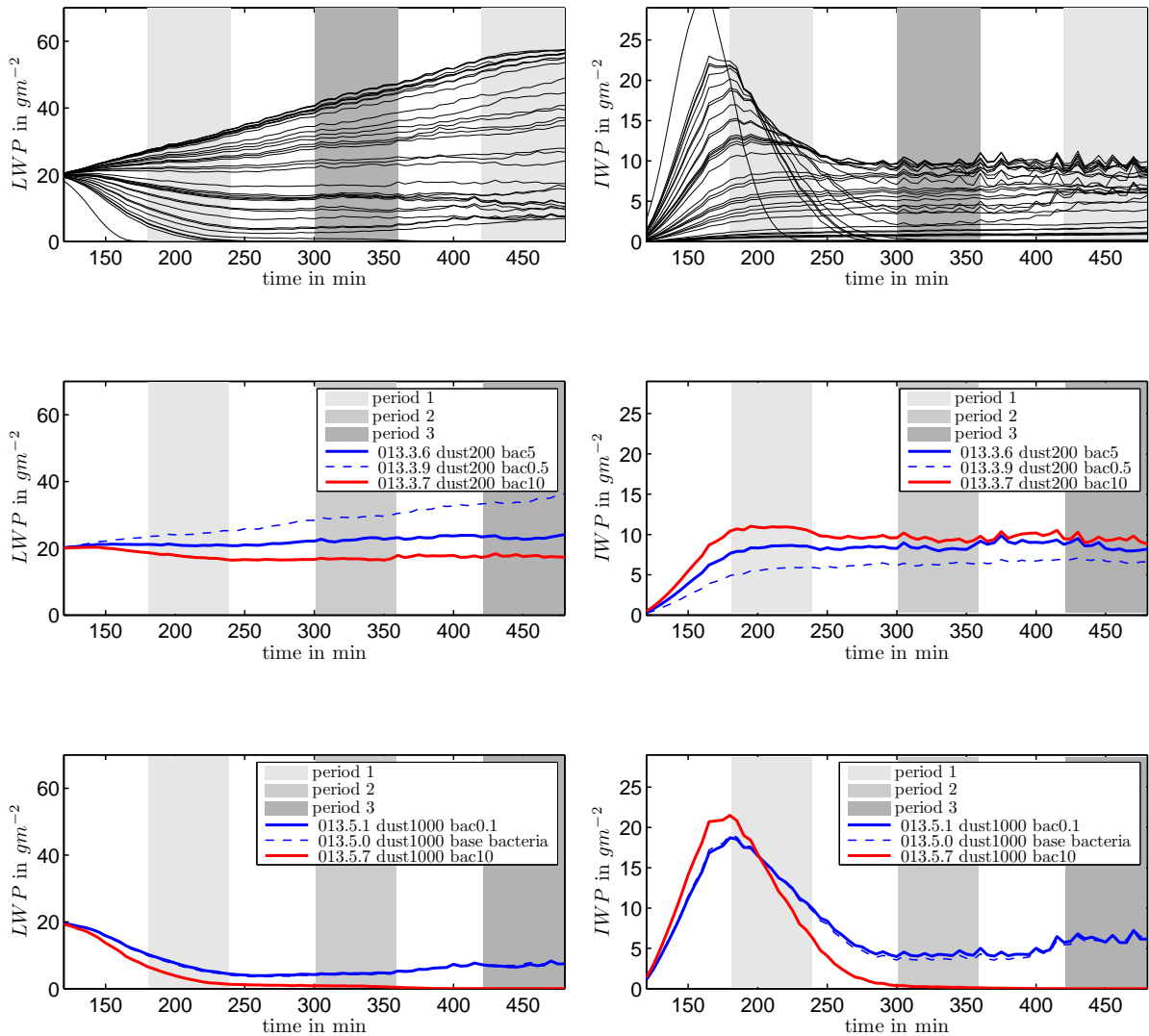


Fig. 4.13.: Top row: Spread of the sensitivity runs as shown in fig. 4.12 with respect to LWP and IWP. Mid row: dust200 runs with varying bacteria concentrations. The blue dashed is a cloud in the “growing regime” (see LWP), therefore found on the left of/below the transition regime in fig. 4.12. Thick full lines are both related to the “transition regime”. Bottom row: For dust1000, all runs are within the oscillating regime. In the bac10 run, the liquid water is consumed completely.

responding small ice number concentrations. Therefore, LWP continuously increases with time. The “oscillation” regime is identified by an initial peak of IWP and decreasing LWP, implying that the cloud is initially dissipated to a certain extent because of the WBF process. However, as presented in section 4.4, the initial dissipation of liquid water does not necessarily consume the whole cloud because of the negative feedback between nucleation and depleted IN. That is why simulations with IN concentrations beyond the transition area can still be classified as persistent in many cases. This is shown for a set of runs in fig. 4.13. In the oscillation regime both LWP and IWP mostly converge to similar values. LWP ranges from $7gm^{-2}$ to $18gm^{-2}$ in period three, whereas IWP is found between five and ten for “oscillating” clouds which are not dissipated. The transition regime can be found for runs with LWPs between $15gm^{-2}$ to $30gm^{-2}$, and IWPs between $7gm^{-2}$ and $9gm^{-2}$.

The “transition area” is derived by analyzing the evolution of LWP and IWP with time. For example, the time series in the second row of fig. 4.13 shows dust200 runs with varying bacteria concentrations. Shaded areas indicate the three periods of averaging. In order to capture the first local maximum of IWP, the period from hour three to hour four (period 1) is used for averaging. By comparison of averages of periods 1 and 2, the status “growing”, “transition” or “oscillating” results from the distinction whether the difference is less or greater than a defined threshold. Because the definition of such a threshold is relatively arbitrary, two different definitions are applied. They are 10% and 5% in magnitude relative to the maximum values of LWP ($50gm^{-2}$) and IWP ($15gm^{-2}$), as colorcoded in fig. 4.12. The 10% definition is plotted in thick black lines and covers larger areas than the 5% definition (thin black lines) in fig. 4.12. In the considered case, the 5% condition is hardly reached in simulations when dust is the dominant IN species. In contrast, the transition area becomes broader in the bacteria regime.

Another definition of the transition regime could be the derivation of a line which is located along concentrations that yield a local minimum in the change with time. This definition would not need a specific threshold. In contrast, changes with time could possibly be different in magnitude.

According to fig. 4.12, the 5% threshold indicates mean in-cloud ice number concentrations between 1.5 and $2 l^{-1}$ to be most likely for a non-growing, non-oscillating cloud. During ISDAC flight 31, measured ice number concentrations vary from $0.2l^{-1}$ to $0.4l^{-1}$ (e.g. Fan et al., 2011) However, these values cannot be compared directly, since measurements account for crystals with maximum dimensions greater than $100\mu m$ only. Simulated in-cloud averages are higher because they strongly depend on smaller crystals, as nucleated ice particles are introduced into the model domain with a diameter of $10\mu m$.

Based on fig. 4.12, the estimation of the base concentration of bacteria is closer to a non-growing regime than the base dust concentration. If the concentration regime defined by the 5% threshold is taken as a reference, called $N_{bac,transition}$, the difference to $N_{bac,base}$ is about one order of magnitude. This is true when dust is negligible, i.e. in the very left region of the plots of fig. 4.12. In regions where dust is the dominating IN species, $N_{dust,transition}$ is three orders of magnitude greater than $N_{dust,base}$. This is because

of the relatively weak ice activity of dust according to the NI12 parameterization in the considered temperature range. Table 4.2 gives a short summary.

Based on all the assumptions of base concentrations, size distributions and depositional ice particle growth rates, the relative contribution of bacterial IN is therefore found to be higher than the contribution of pure dust particles.

Tab. 4.2.: Comparison of aerosol base concentrations for species x , $N_{x,base}$, and concentrations needed to reach the non-growing regime, $N_{x,transition}$, based on simulations of ISDAC flight 31 conditions. Lines one and two are for dominant dust and bacteria concentrations, respectively. Line three gives a possible combination of both species, corresponding to the upper right corner of the the transition regime (fig. 4.12).

IN species	$N_{x,base}$	$N_{x,transition}$	$\frac{N_{x,transition}}{N_{x,base}}$
dust	$0.25cm^{-3}$	$100cm^{-3}$	400
bacteria	$0.01cm^{-3}$	$0.1cm^{-3}$	10
dust & bacteria		$50cm^{-3}$ & $0.05cm^{-3}$	200 & 5

4.8. Dust vs. Bacteria at Colder Temperatures

Given the small contribution of dust to heterogeneous ice nucleation for conditions found during ISDAC flight 31, a second temperature regime is investigated in this section. Assumptions and meteorological conditions are identical to section 4.7, except that temperatures in all levels are 5°C cooler than observed during ISDAC. Here, the relevant in-cloud temperature range is found between -17°C and -20°C .

For consistency, the initial vertical profile of the total specific humidity q_t (see section 3.1.1) has to be adjusted, too. In order to achieve a profile of liquid water content q_l equal to ISDAC flight 31, q_t is generally lower at colder temperatures because of lower saturation vapor pressures. Outside the cloud layer below saturation with respect to liquid water, relative humidities are assumed to be equal to relative humidities during ISDAC, in turn resulting in lower total specific humidities compared to original data. Resulting profiles are shown in fig. 4.14.

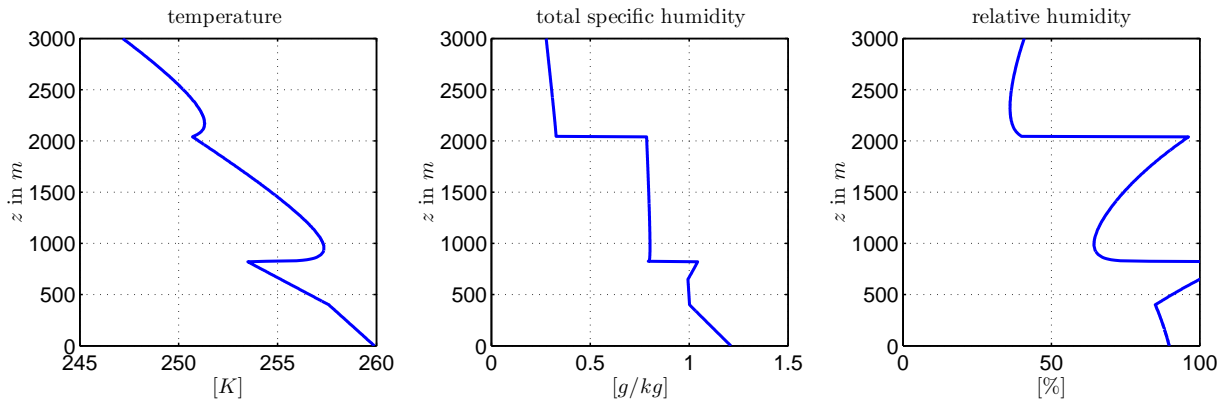


Fig. 4.14.: Modified vertical profiles based on ISDAC flight 31 with temperature shifted to a cooler temperature regime by 5°C in magnitude and adjusted moisture profiles.

Repeating the procedure of the foregoing section yields figure 4.15 for the colorcoded LWP, IWP and mean in-cloud N_i of period 3 (hour 7 to 8). When using 10% thresholds to define the transition regime (see section 4.7), the maximum LWP of non-growing clouds – i.e. within the transition regime – is around 30gm^{-2} , consistent with the warmer ISDAC case. However, an asymmetry is found for the LWP when going along the black line which separates the “transition regime” from the “oscillation regime”. This means that the oscillation begins at higher LWP, corresponding to lower IWP, when ice nucleation is dominated by bacterial IN. According to fig. 4.16, the “oscillation regime” begins at smaller IWP in cases with ice nucleation being dominated by bacteria. The reason is that the bacterial nucleation rate is predominantly related to cloud base entrainment, described later in this section. Therefore, IWP is very sensitive to the reservoir of unactivated IN below cloud, which is not constant in time. These connections give an initial peak in IWP which is responsible for the exclusion from the “transition regime”. Corresponding to these findings, also in-cloud ice number concentrations are not distributed symmetrically in

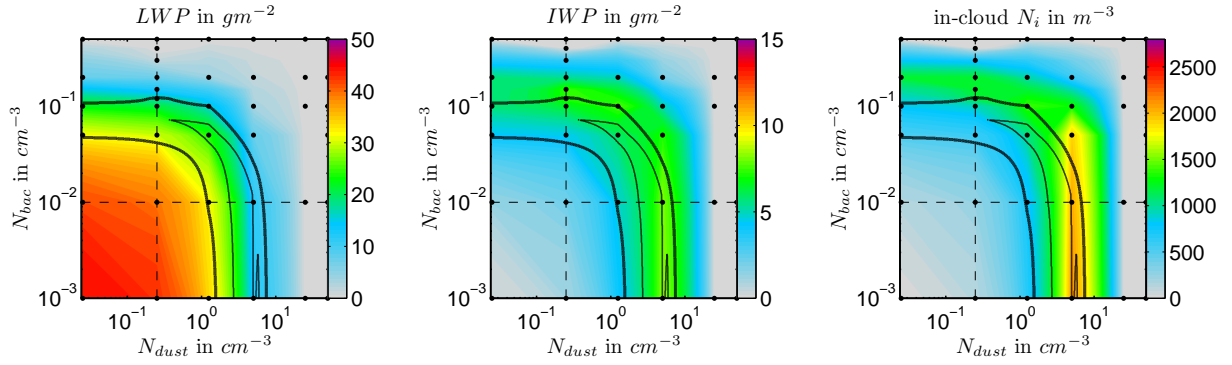


Fig. 4.15.: Results for runs with temperatures shifted 5°C downwards. Base concentrations are indicated by dashed lines. Here, only results of period 3 corresponding to a quasi equilibrium state are shown. See fig. 4.12 for further explanations.

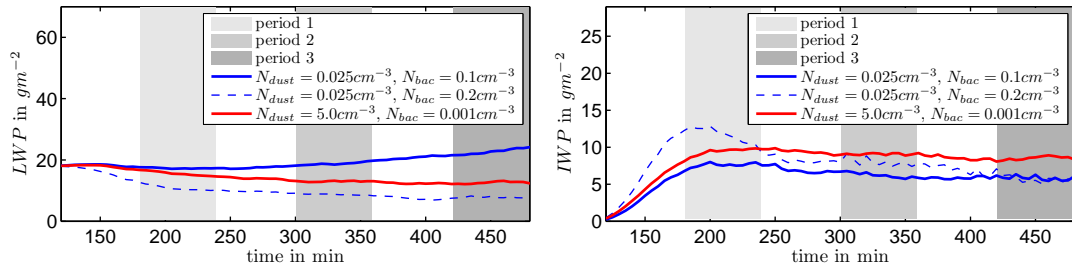


Fig. 4.16.: Comparison of two runs in the “transition regime”. Blue: nucleation dominated by bacteria . Red: nucleation dominated by dust. The IWP of the bacteria-dominated run is smaller by approximately 4gm^{-2} . Also raising the bacteria concentration into the oscillation regime cannot increase IWP to amounts which are reached by dust-dominated runs.

fig. 4.15. Therefore, differences between dust and bacteria with respect to the vertical distributions of nucleation rates will be described in the following.

Figure 4.17 shows differences in nucleation rates in both regimes, where the total ice production rate is divided up into both IN species. Red lines denote the warmer ISDAC case, blue lines the colder temperature regime introduced in this section. First, the relative importance of dust is clearly increased due to its exponential function of $n_s(T)$. That is why dust20 runs have sufficient IN concentrations available to reach the transition regime, also when the effect of additional bacteria is negligible. In contrast, the transition regime at warmer temperatures was only reached with dust400 concentrations and more. Nevertheless, vertical structures of dust nucleation do not differ in both regimes, which means that dust immersion freezing occurs close to the cloud top only.

In the colder situation, a peculiarity of the bacteria’s behavior at cold temperatures becomes apparent, namely the constant value of n_s below -18°C (see fig. 2.4). This means that adiabatic cooling within

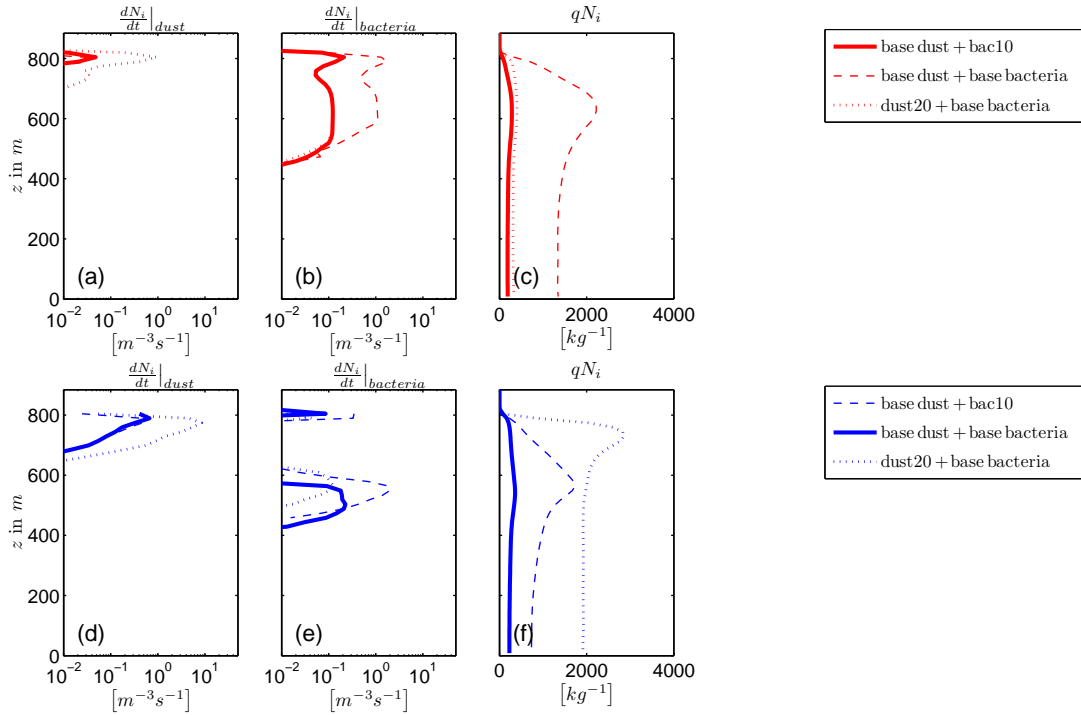


Fig. 4.17.: Comparison of nucleation rates and ice number concentrations in two different temperature regimes. Red: ISDAC flight 31 conditions. Blue: The same concentrations used at 5°C colder temperatures.

updrafts does not yield additional freezing events. That is why there is no in-cloud nucleation in fig. 4.17 e). Therefore the only source for freezing is entrainment of unactivated IN from above and below the cloud. However, cloud top entrainment makes only a small contribution to the total nucleation, since vertical velocities at the temperature inversion are close to zero, such that turbulent diffusion and largescale subsidence are dominant for the entrainment from the free atmosphere. At cloud base, vertical advection of potential IN is the cause for the high nucleation rates observed.

These differences in the locally separated nucleation events and therefore vertical distributions of ice crystals (see blue lines of fig. 4.17) are therefore responsible for the different evolutions of dust-dominated and bacteria-dominated scenarios.

The finding that bacterial nucleation in the colder regime is dominated by cloud-base entrainment causes an important feedback for the temporal evolution of bacterial nucleation rates. Figure 4.18 compares both temperature regimes in terms of vertically integrated nucleation rates which are separated into the dust species and bacteria species. Analogous to fig. 4.6, each dot in the space of nucleation rates corresponds to a single output time step and linked dots belong to one simulation. In the ISDAC regime (fig. 4.18 a)), vertically integrated nucleation rates do not vary much with time, so that the dots are close together for one simulation. Only in the “oscillation regime”, they oscillate corresponding to varying cloud depth and the strength of dynamics. In contrast, at colder temperatures there is a specific drop of the bacterial nucleation rates after some time in all of the simulations. Depending predominantly on

Tab. 4.3.: Comparison of aerosol base concentrations for species x , $N_{x,base}$, and concentrations needed to reach the non-growing regime, $N_{x,transition}$, based on simulations with temperatures being 5°C colder than ISDAC flight 31 (see table 4.2). Lines one and two are for dominant dust and bacteria concentrations, respectively. Line three gives a possible combination of both species, corresponding to the upper right corner of the the transition regime (fig. 4.15).

IN species	$N_{x,base}$	$N_{x,transition}$	$\frac{N_{x,transition}}{N_{x,base}}$
dust	0.25cm^{-3}	3cm^{-3}	12
bacteria	0.01cm^{-3}	0.07cm^{-3}	7
dust & bacteria		1cm^{-3} & 0.05cm^{-3}	4 & 5

cloud base entrainment, these decreasing nucleation rates are clearly related to the mixing process of depleted IN. Once the boundary layer is mixed with respect to the spatial distribution of depleted IN, the probability to fulfill the Δn_s condition (fig. 2.7) is reduced significantly, resulting in reduced nucleation rates.

In conclusion, this section consolidates that not only the absolute value of the ice nucleation activity of an IN species, and $(n_s S_{tot})$, respectively, is an important measure for ice nucleation. Thus, when taking into account in-cloud dynamics and vertical velocities in particular, the ice nucleation activity's change

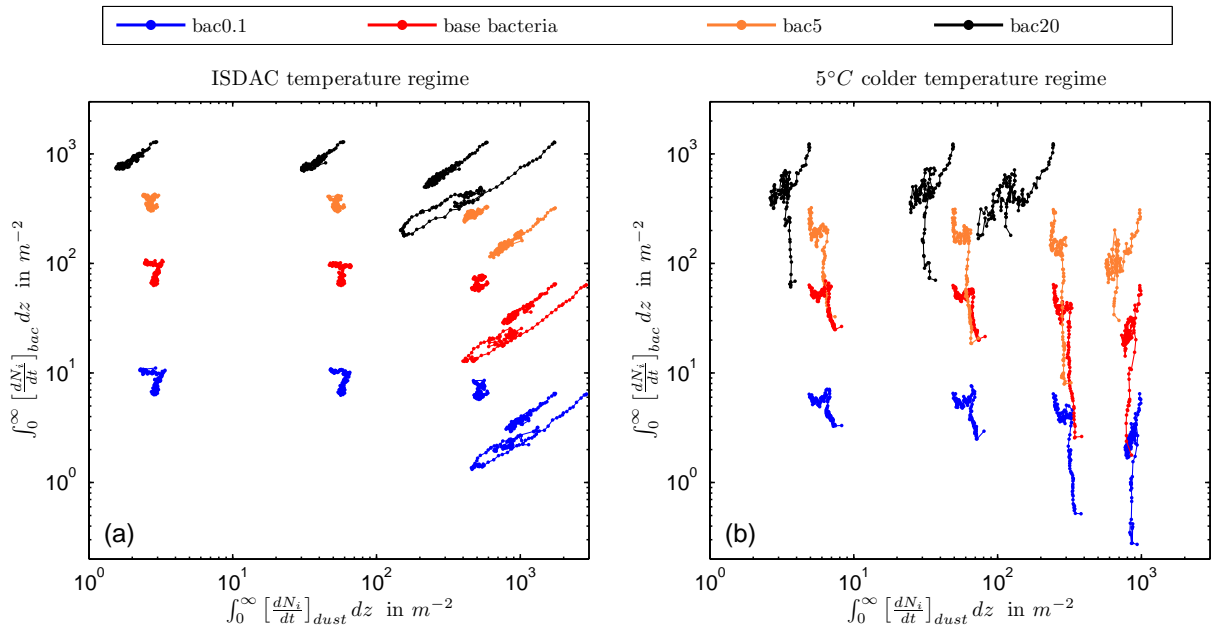


Fig. 4.18.: Comparison of nucleation rates in the ISDAC temperature regime (left) and at 5°C colder temperatures (right). Vertically integrated rates are separated into dust and bacteria. Each set of linked dots corresponds to one simulation, whereas bacteria-concentrations are colorcoded. Dust concentrations range from base dust to dust1000 in the warmer regime and from dust0.1 to dust20 in the colder regime.

with height influences the primary ice production. A saturation effect as seen for bacteria below -18°C in this case can even suppress new nucleation when cooling takes place below that threshold.

4.9. Sensitivity to Cloud Top Radiative Cooling

In fig. 4.19, the longwave radiation cooling rate $THHR$ (thermal heating rate) calculated by COSMO's δ two-stream radiation transfer scheme (Ritter and Geleyn, 1992) and the simplified version (see section 2.3.3) are compared. The latter is assumed to be valid for the considered case (Ovchinnikov et al., 2012; Stevens et al., 2005). Significant differences can be seen with values twice as large using the COSMO default scheme. The effect of a greater $THHR$ is a stronger buoyant production of turbulence and boundary layer mixing, resulting in deeper clouds (not shown).

Some additional sensitivity tests were conducted with moderately increased cooling rates calculated by the simplified radiation scheme depending on the LWP. They were simply parameterized using eq. 2.48 multiplied by fac_{rad} , i.e.

$$\frac{\partial T}{\partial t} = -fac_{rad} \frac{1}{\rho c_p} \frac{\partial F}{\partial z}. \quad [4.2]$$

Sensitivities to 5% and 25% increased cooling rates were tested, i.e. $fac_{rad} = 1.05$ and $fac_{rad} = 1.25$, respectively. Furthermore, the COSMO default ice nucleation parameterization including the depletion effect and the base dust concentration was specified. Therefore, the reference run with $fac_{rad} = 1.0$ is characterized by few ice particles (see fig. 4.3) and a liquid-dominated growing liquid layer.

The results are moderately increased vertical velocities, in general yielding increased LWP and IWP. This can be seen as a validation of the connections discussed in section 3.3.2, in which increased vertical velocities emerging from different numerical treatments could be correlated to the LWP and IWP. Table 4.4 summarizes the relative changes which are also shown in fig. 4.20.

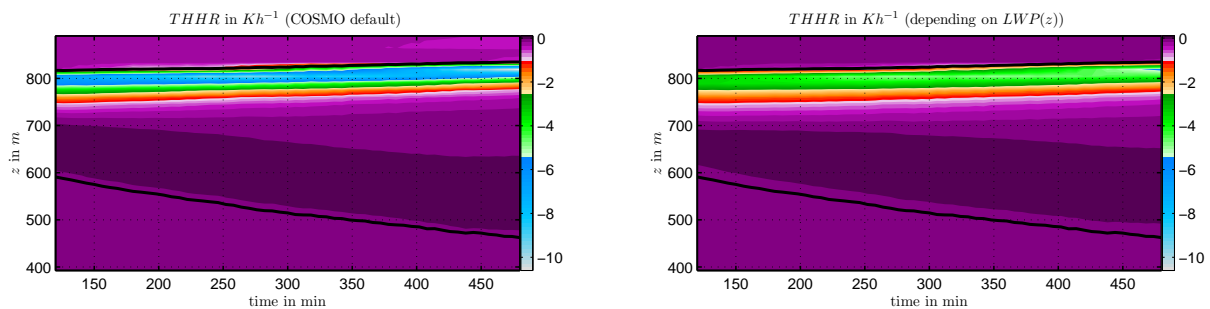


Fig. 4.19.: Comparison of original longwave radiation cooling rate (left) and the simplified parameterization (right) depending on LWP only. Both calculations shown are based on the same situation using base dust, resulting in a factor of two.

Tab. 4.4.: Relative changes of w_{max} , LWP and IWP depending on enhanced longwave radiation.

fac_{rad}	w_{max}	LWP	IWP
1.05	1.07	1.07	1.06
1.25	1.19	1.33	1.28

According to these results, already small variations in the cooling rate can modify the cloud properties significantly. Thus, the cooling rate can potentially determine the cloud's glaciation in a regime close to "critical" concentrations of ice nuclei. Consequently, the exact reason for the factor two difference in $THHR$ between the two radiation schemes is an interesting issue for further investigations.

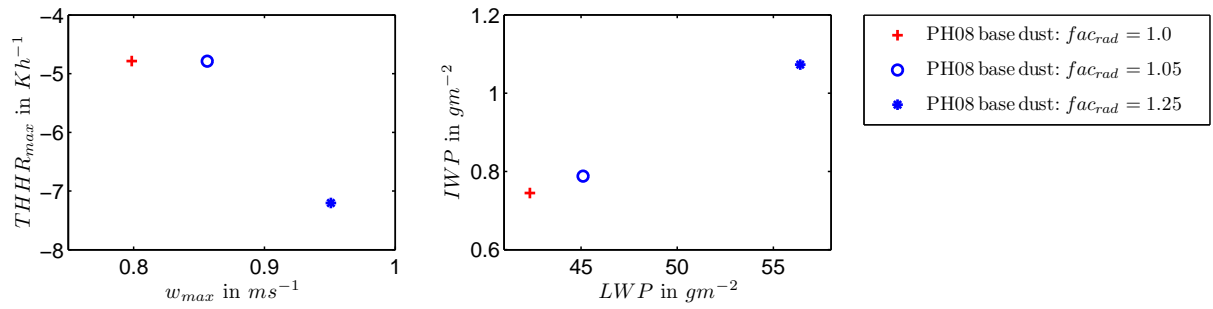


Fig. 4.20.: Sensitivities of vertical velocities, LWP and IWP to changes in the longwave radiation cooling rate.

5. Summary and Outlook

Summary and Interpretation

Motivated by the dependence of the surface cloud radiative forcing on the liquid water path, this work concentrated on the simulation of a persistent Arctic mixed-phase stratocumulus layer observed during ISDAC Flight 31 on April 26 2008. Since the liquid water path is strongly coupled to ice number concentrations, a special emphasis was the ice nucleation within the cloud.

In a first step, the COSMO model took part in a model intercomparison. Therefore, the configuration was prepared for an LES-type simulation, ensuring to capture small-scale processes. After that, a radiation scheme specifically tuned for the considered stratocumulus layer was implemented. In addition, microphysical parameters were tuned for the sake of consistency among different models.

Results suggest that COSMO is able to capture the situation well enough to use it for further studies of this type. Differences in the partitioning of LWP and IWP were identified to be related to different ice particle size distributions among the models. However, a remaining question is the source for differences in the distribution of vertical velocities. Specifically, the maximum vertical velocities reached in the COSMO model domain are generally on the lower end of the range of the participating models. Possible candidates are turbulence schemes and different numerical treatments among the models.

The second part of this work was to drop the constraint of a prescribed ice number concentration and to analyze ice nucleation instead. Therefore, immersion freezing was assumed to be the only heterogeneous nucleation mechanism which was active in this case.

The depletion of activated ice nuclei was implemented using an additional prognostic variable. The analysis of the depletion effect in the considered case showed the removal of a bias in nucleation which is caused by sedimenting ice crystals in the default microphysics scheme, in which nucleation is directly linked to existing ice crystals. Allowing for dynamic feedbacks, the depletion scheme is able to simulate a persistent mixed-phase layer in a broader range of aerosol concentrations.

Building on the singular hypothesis, two parameterizations based on the ice nucleation active surface site density were implemented for mineral dust and bacteria. Analyzing the clouds' temporal evolution yielded an estimate for the concentrations of both species needed to simulate a persistent cloud layer. In general, the ice number concentrations are less than those observed during ISDAC when using the base concentrations of aerosols. If natural desert dust was the only IN species, a dust concentration 400 times greater than the base concentration was needed in the ISDAC temperature regime. For bacteria, a factor of 10 was found. Therefore, it has to be taken into account whether additional IN species exist which

can contribute significantly to ice number concentrations. Furthermore, it can be speculated about ice forming mechanisms besides the immersion freezing mode.

Comparing COSMO's default radiation scheme and the simplified radiation parameterization tuned for this case, a factor of two in the thermal heating rate becomes apparent. Sensitivity tests showed that vertical velocities as well as LWP and IWP correlate well with increased cloud-top cooling rates.

The overall picture of the results in this work fit to the efforts of foregoing studies, finding a high sensitivity of the clouds' evolution to ice number concentrations. Morrison et al. (2011b) concluded that the influence of the WBF process was only indirect. Therefore, it was not the water vapor deposition rate itself which glaciated the cloud by consuming the liquid water, but the cycle of positive feedbacks.

Some studies came to the conclusion that the immersion freezing mode was of minor importance, suggesting contact nucleation instead (e.g. Morrison et al., 2005b). However, assumptions on the representation of heterogeneous nucleation modes differ among studies. For example, when representing the immersion freezing by the parameterization of Bigg (1953b,a) - see section 2.1.4 - results lead to the conclusion that immersion freezing is negligible (e.g. Morrison et al., 2005b). In the case considered here, nearly 90% of the particles were activated as cloud condensation nuclei within in the cloud (McFarquhar et al., 2011), thus the remaining interstitial aerosol particles were less in number concentration, but also smaller in size.

Furthermore, the depletion effect was implemented previously in other models. For example, Harrington and Olsson (2001) applied a similar implementation in their model, using the Meyers et al. (1992) ice nucleation parameterization and use the maximum ice supersaturation of an air parcel reached, corresponding to $N_{IN,old}$ in this work. In their study, they find a very strong suppression of nucleation events when using their extended nucleation scheme. Compared to that result, the suppression of nucleation is weaker in this work, since even when $N_{IN,old}$ is mixed within the boundary layer, the ice production rates remain at high levels (see fig. 4.18). However, differences in the temporal evolution of the ice production rates were caused by the varying steepnesses of $n_s(T)$. Since the scheme of Harrington and Olsson (2001) depends on $N_{IN}(S_i)$ rather than $n_s(T)$, this might possibly explain the differences, since also the vertical distribution of S_i is relevant in that case. This points at the importance of the steepness of parameterization fit functions not only for the absolute value of parameterized ice particles, but also for the effectiveness of IN depletion.

Concerning nucleation modes, Morrison et al. (2008) speculated about unknown mechanisms besides condensation/ immersion freezing, deposition nucleation and contact freezing when simulating an M-PACE case, in which modeled ice crystal concentrations were too low, too. Hypotheses were given by Fridlind et al. (2007) who were able to gain realistic results when implementing "evaporation nuclei" in their model, which were based on the residuals of evaporating droplets.

Discussion of Constraints and Possible Solutions

This final section will shortly discuss some constraining assumptions which were made for the simulations of this work and will suggest solutions that could be applied in possible follow-up studies.

Stated that in general a factor of two is found as difference between the simplified stratocumulus radiation parameterization and the more sophisticated COSMO scheme (Ritter and Geleyn, 1992), it is important to know in which range the simple version is valid. Since its parameters are tuned for the specific observations, it may possibly be not valid for modeled clouds which differ greatly from the observed cloud. Since a strong sensitivity of the cloud's properties to cloud-top radiative cooling was shown, this topic deserves attention in future work.

In section 2.2.3 it was explained that there is no sink for $N_{IN,old}$ but only a source term in case of an ice nucleation event. Given this constraint, it would be difficult to use the depletion scheme for a long term simulation, since the model domain would be filled with $N_{IN,old}$ with time, suppressing nucleation. A first effort could be an implementation which accounts for evaporating ice particles, therefore releasing their ice nuclei and acting as a sink for $N_{IN,old}$. In addition, this would be an interesting possibility to test sensitivities of preactivated IN, which were found to be possibly more ice active than first-time activated aerosols (Vali, 1999; Pruppacher and Klett, 1997). Since in this case there is subsaturation with respect to ice below the cloud layer, multiple cycles of in-cloud freezing and below-cloud evaporation might reduce the discrepancy between aerosol concentrations observed and those needed to reach the “transition regime”. However, simulations of M-PACE conditions accounting for IN recycling (Fridlind et al., 2007) showed only an effect during the first four hours of simulation, with ice number concentrations converging to the results with neglected recycling.

In sections 4.7 and 4.8, the “transition regime” was related to the clouds' development with time. For these simulations, fac_{Γ} was equal to 1 and it was also shown in section 3.3.1 that a strong sensitivity to its value exists and that $fac_{\Gamma}=1$ does not fully account for ventilation effects. Hence, to simulate clouds closer to reality, the full implementation including ventilation would be desirable. It is expected that the transition regime would therefore be shifted towards lower concentrations for both dust and bacteria. Nevertheless, the large discrepancy between base concentrations and those needed for a non-growing cloud would most likely be preserved.

The simulations conducted in this work were based on an idealized setup with periodic boundary conditions, therefore not depending on a large-scale model providing boundary conditions. With horizontal wind speeds of approximately $7 \frac{m}{s}$ and a simulation time of eight hours, the simulated conditions correspond to air parcels which have been advected by a horizontal distance of 200km. Although such horizontal extents of Arctic mixed-phase clouds are not unrealistic (see fig. 1.1), an interesting aspect could be the influence of the horizontal advection of ice nuclei. To account for this effect, a sink for

$N_{IN,old}$ could be defined by nudging towards zero, counteracting the depletion effect. In reality, this situation would occur on the horizontal edges of the cloud layer located on the windward sides. Another possibility can be a temporal change of aerosol concentrations with time.

Also concerning the spatial distribution of aerosols, the assumption in this work was a distribution which was vertically constant. Depending on the kind of aerosol, different profiles might be present. Since dust is primarily advected over large distances, it can be expected to find higher concentrations above the boundary layer than within or below the cloud. In contrast, when assuming the ocean or generally local sources to be dominant, highest concentrations can be expected within the boundary layer. Therefore, the asymmetry between dust-dominated and bacteria-dominated cases found in section 4.8 can even be enhanced, as cloud base entrainment of bacteria and cloud top entrainment of mineral dust would be increased compared to the situation with vertically constant profiles.

6. List of Model Settings, Acronyms and Symbols

Model Setting	Chapter 3	Chapter 4
N_i	constant ($0/1/4l^{-1}$)	parameterized
fac_{Γ}	0.76	1
$\Delta x/\Delta y/\Delta z$	50m/50m/10m	100m/100m/15m
Δt	1s	2s
hincrad	1s	2s
itype_turb	7	7
l3dturb	t	t
lprog_tke	t	t
itype_gscp	2403	2403

Acronym	Description
AMPC	Arctic Mixed-Phase Cloud(s)
BC	inorganic Black Carbon (PH08)
CCN	Cloud Condensation Nuclei
CFDC	Continuous Flow Diffusion Chamber
COSMO	COnsortium for Small-scale MOdeling
DM	Dust and Metallic compounds (PH08)
FIRE-ACE	First ISCCP Regional Experiment Arctic Clouds Experiment
Ice0	model run with $N_i = 0l^{-1} = const.$
Ice1	model run with $N_i = 1l^{-1} = const.$
Ice4	model run with $N_i = 4l^{-1} = const.$
IN	Ice Nuclei
ISDAC	Indirect and Semi-Direct Aerosol Campaign
LES	Large Eddy Simulation
LWP	Liquid Water Path
IWP	Ice Water Path
M-PACE	Mixed-Phase Arctic Cloud Experiment
MOR	Morrison et al. (2005a)
NI12	Niemand et al. (2012)
O	insoluble Organic aerosols (PH08)
PH08	Phillips et al. (2008)
Ps	Pseudomonas syringae
PSD	Particle Size Distribution
REFLEX	Radiation and Eddy FLux EXperiment
SHEBA	Surface Heat Budget of the Arctic Ocean
THHR	Thermal Heating Rate
WBF	Wegener-Bergeron-Findeisen
X	aerosol class in the notation of PH08 ($X \in \{DM, BC, O\}$)

6. List of Model Settings, Acronyms and Symbols

Symbol	Unit	Description
a	different	parameterization constants
a_c	m kg^{-b_c}	power law coefficient for the capacitance-mass relationship of an ice crystal
$a_{i,g}$	m	ice germ radius
a_m	kg m^{-b_m}	power law coefficient for the mass-diameter relationship of an ice crystal
a_v	m^{1-b_v}	power law coefficient for the velocity-diameter relationship of an ice crystal
A	$\text{kg}^{-(v+1)}\text{m}^{-3}$	coefficient of the generalized Γ -distribution
A_p	m^2	surface area of a particle
b	1	parameterization constants
b_c	1	power law exponent for the capacitance-mass relationship of an ice crystal
b_m	1	power law exponent for the mass-diameter relationship of an ice crystal
b_v	1	power law exponent for the velocity-diameter relationship of an ice crystal
c	kg m^{-b_m}	as a_m , in Morrison et al. (2005a)
c_p	$\text{J kg}^{-1}\text{K}^{-1}$	specific heat capacity of dry air at constant pressure
c_ϕ	s^{-1}	nudging coefficient for the prognostic variable ϕ
C	m	capacitance
CF	W m^{-2}	surface cloud radiative forcing
CF_{LW}	W m^{-2}	surface cloud longwave radiative forcing
CF_{SW}	W m^{-2}	surface cloud shortwave radiative forcing
d	1	as b_m , in Morrison et al. (2005a)
D	m	diameter of aerosol particles and hydrometeor species
D_g	m	lognormal size distribution median diameter
D_p	m	particle diameter
D_v^*	m^2s^{-1}	diffusivity of water vapor in air (corrected for gas kinetic effects)
e	Pa	water vapor pressure in moist air
e_i	Pa	saturation vapor pressure over a plane ice surface
e_s	Pa	saturation vapor pressure over a plane water surface
IWP	g m^{-2}	ice water path
$f(D)$	m^{-3}	size distribution density function
$f(m)$	m^{-3}	size distribution density function; factor depending on the contact angle θ
$f(x)$	1	probability density function
$f_i(D_p)$	1	ice fraction depending on particle diameters
f_{INA}	1	fraction of ice nucleation active bacteria
$f_{NSD}(D_p)$	m^{-3}	particle number size distribution
$F(z)$	W m^{-2}	net longwave radiative flux
F_0	W m^{-2}	constant for parameterizing $F(z)$
F_1	W m^{-2}	constant for parameterizing $F(z)$
F_{LW}	W m^{-2}	longwave radiative flux
$F^{(k)}$	$\text{kg}^k\text{m}^{-3}\text{s}^{-1}$	flux of the k^{th} moment
fac_Γ	1	prefactor of the vapor deposition rate
fac_{rad}	1	prefactor of the thermal heating rate
H_X	1	empirical function of T and S_i in PH08 for aerosol class X
$J(T)$	different	nucleation rate at constant temperature
J_c	$\text{m}^{-3}\text{s}^{-1}$	characteristic nucleation rate (Vali, 1994)
k	1	Index of a moment; constants for parameterizing $F(z)$ and $F_{LW}(z)$
$k(T)$	different	(differential) nucleus spectrum
k_a^*	$\text{J m}^{-1}\text{s}^{-1}\text{K}^{-1}$	heat conductivity of air (corrected for gas kinetic effects)
k_B	J K^{-1}	Boltzmann constant

Symbol	Unit	Description
$K(T)$	different	(cumulative) nucleus spectrum
K	$\text{cm}^{-3}\text{s}^{-1}$	constant to parameterize the freezing probability P
L_e	J kg^{-1}	latent heat of evaporation
L_s	J kg^{-1}	latent heat of sublimation
L_x	kg m^{-3}	mass density of particle species x
LWP	g m^{-2}	liquid water path
m	1	cosine of the contact angle between an ice germ and its substrate
m	kg	particle mass
\bar{m}_x	kg	mean mass of particle species x
$M^{(k)}$	1	k^{th} moment of a density function
M_W	kg	molecular weight of water
$n_s(T)$	m^{-2}	ice nucleation active surface site density
n_x	kg^{-1}	number density of species x in PH08
N_d	cm^{-3}	droplet number density
N_f	1	number of frozen droplets
$N_{i,0}$	l^{-1}	prescribed ice number density
N_{tot}	1	number of total droplets
N_u	1	number of unfrozen droplets
N_x	m^{-3}	number density of particle species x
p_c	1	Morrison et al. (2005a) PSD shape factor
P	1	freezing probability of a droplet
q_i	kg kg^{-1}	specific humidity of ice
q_l	kg kg^{-1}	specific humidity of liquid water
q_t	kg kg^{-1}	total specific humidity
q_v	kg kg^{-1}	specific humidity of vapor
qN_x	kg^{-1}	number mixing ratio of particle species x
\bar{r}_i	m	mean radius of ice crystals
\bar{r}_w	m	mean radius of liquid water droplets
R	$\text{J kg}^{-1}\text{K}^{-1}$	universal gas constant
$R(T, t)$	s^{-1}	freezing rate of droplets
s_i	1	supersaturation with respect to ice
S_i	1	supersaturation ratio with respect to ice
S_{tot}	m^2m^{-3}	total surface area of an aerosol size distribution per volume of air
t	s	time
T	K	temperature
T_c	K	characteristic temperature (Vali, 1994); characteristic cloud temperature
T_{hom}	K	homogeneous freezing temperature
T_s	$^{\circ}\text{C}$	supercooling
T_{∞}	K	temperature of the air surrounding an ice crystal
u	m s^{-1}	horizontal wind component in x-direction
v	m s^{-1}	horizontal wind component in y-direction
$v_x(m)$	m s^{-1}	sedimentation velocity of a particle with mass m of particle species x
$\bar{v}_x^{(k)}(\bar{m})$	m s^{-1}	sedimentation velocity of the k^{th} moment of particle species x
V_d	m^3	droplet volume
w_{max}	m s^{-1}	maximum vertical velocity
w_{LS}	m s^{-1}	vertical velocity due to large-scale subsidence
w^*	m s^{-1}	threshold vertical velocity (Korolev, 2007)
w^o	m s^{-1}	threshold vertical velocity (Korolev, 2007)
z	m	vertical coordinate

6. List of Model Settings, Acronyms and Symbols

Symbol	Unit	Description
α_X	1	fraction of aerosol class X relative to the total aerosol
γ_c	K s^{-1}	constant cooling rate
λ	$\text{kg}^{-\mu}$	exponent of the generalized Γ -distribution
ϕ	different	prognostic variable
μ_X	1	function of D_p , S_i and T in PH08 for aerosol class X
μ	1	exponent of the generalized Γ -distribution
ν	1	exponent of the generalized Γ -distribution
$\xi(T)$	1	empirical function of T in PH08 for all aerosol classes
σ	1	lognormal size distribution standard deviation
η	m^3s^{-1}	coefficient to determine w^* (Korolev, 2007)
χ	m^3s^{-1}	coefficient to determine w^o (Korolev, 2007)
$\sigma_{i/w}$	Nm^{-1}	surface tension between water and ice
σ_{SB}	$\text{Wm}^{-2}\text{K}^{-4}$	Stefan-Boltzmann constant
ρ	kg m^{-3}	density of air
θ_l	K	liquid water potential temperature
θ	different	potential temperature; contact angle between an ice germ and its substrate
$\Gamma(y)$	1	Eulerian Gamma function
$\Delta\phi$	different	increment for variable ϕ due to nudging
$\Delta\phi_{LS}$	different	increment for variable ϕ due to large-scale subsidence
ΔT_{CIN}	$\text{K}/^\circ\text{C}$	temperature shift for contact nucleation after PH08
Δx	m	horizontal grid spacing in x-direction
Δy	m	horizontal grid spacing in y-direction
Δz	m	vertical grid spacing
Δt	s	model time step
ΔF_g	J	work of ice germ formation
Δg^+	J	molar activation energy
Ω_X	m^2kg^{-1}	surface area mixing ratio of aerosol class X for diameters $> 0.1\mu\text{m}$ (PH08)
$\Omega_{X,1^*}$	m^2kg^{-1}	component of Ω_X for background aerosols class X with diameters between $0.1\mu\text{m}$ and $1\mu\text{m}$ (PH08)

A. Bibliography

- Abmann, R. and A. Berson (1900). *Wissenschaftl. Luftfahrten, Braunschweig* 2, 184.
- Bangert, M., A. Nenes, B. Vogel, H. Vogel, D. Barahona, V. A. Karydis, P. Kumar, C. Kottmeier and U. Blahak (2012). Saharan dust event impacts on cloud formation over western Europe. *Atmos. Chem. Phys.* 12, 4045–4063.
- Barklie, R. H. D. and N. R. Gokhale (1959). The freezing of supercooled water drops. *Scientific Report, Stormy Weather Group, McGill University, Montreal* , MW-30, 43–64.
- Barrie, L. A. (1986). Arctic air pollution: an overview of current knowledge. *Atmos. Environ.* 19, 1995–2010.
- Beard, K. V. and H. R. Pruppacher (1971). A wind tunnel investigation of the rate of evaporation of small water drops falling at terminal velocity in air. *J. Atmos. Sci.* 28, 1455–1464.
- Beheng, K. D. (1982). A numerical study on the combined action of droplet coagulation, ice particle riming and the splintering process concerning maritime cumuli. *Contrib. Atmos. Phys* 55, 201–214.
- Betts, A. K. (1973). Non-precipitating cumulus convection and its parameterization. *Q. J. Roy. Meteor. Soc.* 99, 178–196.
- Bigg, E. K. (1953a). The formation of atmospheric ice crystals by the freezing of droplets. *Q. J. Roy. Meteor. Soc.* 79, 510–519.
- Bigg, E. K. (1953b). The supercooling of water. *Proc. Phys. Soc.* 66, 688–694.
- Blanchard, D. C. (1957). The supercooling, freezing and melting of giant water drops at terminal velocity in air. *Artificial Stimulation of Rain* , 233–249.
- Bronstein, I. N., K. A. Semendjaev, G. Musiol and H. Mühlig (editors) (2008). *Taschenbuch der Mathematik*. Deutsch, Frankfurt am Main, 7th ed.
- Burrows, S. M., T. Butler, P. Jöckel, H. Tost, A. Kerkweg, U. Pöschl and M. G. Lawrence (2009b). Bacteria in the global atmosphere - Part 2: Modeling of emissions and transport between different ecosystems. *Atmos. Chem. Phys.* 9, 9281–9297.
- Burrows, S. M., W. Elbert, M. G. Lawrence and U. Pöschl (2009a). Bacteria in the global atmosphere - Part 1: Review and synthesis of literature data for different ecosystems. *Atmos. Chem. Phys.* 9, 9263–9280.

- Chen, B., D. H. Bromwich, K. M. Hines and X. Pan (1995). Simulations of the 1979-1988 polar climates by global climate models. *Ann. Glaciol.* 21, 85–90.
- Chen, J.-P., A. Hazra and Z. Levin (2008). Parameterizing ice nucleation rates using contact angle and activation energy derived from laboratory data. *Atmos. Chem. Phys.* 8, 7431–7449.
- Connolly, P. J., O. Möhler, P. R. Field, H. Saathoff, R. Burgess, T. Choularton and M. Gallagher (2009). Studies of heterogeneous freezing by three different desert dust samples. *Atmos. Chem. Phys.* 9, 2805–2824.
- Cooper, W. A. (1980). A method of detecting contact ice nuclei using filter samples. *8th Intl. Conf. on Cloud Physics, Clermont-Ferrand, France*, , 665–668.
- Curry, J. A. (1986). Interactions among turbulence, radiation and microphysics in Arctic stratus clouds. *J. Atmos. Sci.* 43, 90–106.
- Curry, J. A., P. V. Hobbs, M. D. King, D. A. Randall, P. Minnis, G. A. Isaac, J. O. Pinto, T. Uttal, A. Bucholtz, D. G. Cripe, H. Gerber, C. W. Fairall, T. J. Garrett, J. Hudson, J. M. Intrieri, C. Jakob, T. Jensen, P. Lawson, D. Marcotte, L. Nguyen, P. Pilewskie, A. Rangno, D. C. Rogers, K. B. Strawbridge, F. P. J. Valero, A. G. Williams and D. Wylie (2000). FIRE Arctic Clouds Experiment. *Bull. Am. Meteor. Soc.* 81, 5–29.
- Curry, J. A., W. B. Rossow, D. Randall and J. L. Schramm (1996). Overview of Arctic cloud and radiation characteristics. *J. Clim.* 9, 1731–1764.
- de Boer, G., T. Hashino and G. J. Tripoli (2010). Ice nucleation through immersion freezing in mixed-phase stratiform clouds: Theory and numerical simulations. *Atmos. Res.* 96, 315–324.
- Deshler, T. (1982). *Contact Ice Nucleation by Submicron Atmospheric Aerosols*. Ph.D. dissertation, Dept. Phys. Astronomy, University of Wyoming, Laramie, Wyoming.
- Després, V. R., J. A. Huffman, S. M. Burrows, C. Hoose, A. S. Safatov, G. Buryak, J. Fröhlich-Nowoisky, W. Elbert, M. O. Andreae, U. Pöschl and R. Jaenicke (2012). Primary biological aerosol particles in the atmosphere: A review. *Tellus B* 64, 15598.
- Doms, G. (2011). A description of the nonhydrostatic regional COSMO-model. Part I: Dynamics and numerics URL <http://www.cosmo-model.org>.
- Doms, G., J. Förster, E. Heise, H.-J. Herzog, D. Mironov, M. Raschendorfer, T. Reinhardt, B. Ritter, R. Schrodin, J.-P. Schulz and G. Vogel (2011). A description of the nonhydrostatic regional COSMO Model. Part II: Physical parameterization URL <http://www.cosmo-model.org>.
- Earle, M. E., P. S. K. Liu, J. W. Strapp, A. Zelenyuk, D. Imre, G. M. McFarquhar, N. C. Shantz and W. R. Leitch (2011). Factors influencing the microphysics and radiative properties of liquid-dominated

- Arctic clouds: Insight from observations of aerosol and clouds during ISDAC. *J. Geophys. Res.* *116*, D00T09.
- Fan, J., S. Ghan, M. Ovchinnikov, X. Liu, P. J. Rasch and A. Korolev (2011). Representation of Arctic mixed-phase clouds and the Wegener-Bergeron-Findeisen process in climate models: Perspectives from a cloud-resolving study. *J. Geophys. Res.* *116*, D00T07.
- Fridlind, A. M., A. S. Ackerman, G. M. McFarquhar, G. Zhang, M. R. Poellot, P. J. DeMott, A. J. Prenni and A. J. Heymsfield (2007). Ice properties of single-layer stratocumulus during the Mixed-Phase Arctic Cloud Experiment (MPACE): 2. Model results. *J. Geophys. Res.* *112*, D24202.
- Fridlind, A. M., B. van Diedenhoven, A. S. Ackerman, A. Avramov, A. Mrowiec, H. Morrison, P. Zuidema and M. D. Shupe (2012). A FIRE-ACE/SHEBA case study of mixed-phase Arctic boundary layer clouds: Entrainment rate limitations on rapid primary ice nucleation processes. *J. Atmos. Sci.* *69*, 365–389.
- Garrett, T. J. and C. Zhao (2006). Increased Arctic cloud longwave emissivity associated with pollution from mid-latitudes. *Nature* *440*, 787–789.
- Hallett, J. and S. C. Mossop (1974). Production of secondary ice particles during the riming process. *Nature* *249*, 26–28.
- Harrington, J. Y. and P. Olsson (2001). On the potential influence of ice nuclei on surface-forced marine stratocumulus cloud dynamics. *J. Geophys. Res.* *106* (D21), 27473–27484.
- Harrington, J. Y., T. Reisin, W. R. Cotton and S. M. Kreidenweis (1999). Cloud resolving simulations of Arctic stratus Part II: Transition-season clouds. *Atmos. Res.* *51*, 45–75.
- Hartmann, S., S. Augustin, T. Clauss, J. Voigtländer, D. Niedermeier, H. Wex and F. Stratmann (2012). Immersion freezing of ice nucleating active protein complexes. *Atmos. Chem. Phys. Discussions* *12*, 21321–21353.
- Herman, G. F. and J. A. Curry (1984). Observational and theoretical studies of solar radiation in Arctic stratus clouds. *J. Clim. Appl. Meteorol.* *23*, 5–24.
- Hoose, C., J. E. Kristjánsson and S. M. Burrows (2010a). How important is biological ice nucleation in clouds on a global scale? *Environ. Res. Lett.* *5*, 024009.
- Hoose, C., J. E. Kristjánsson, J.-P. Chen and A. Hazra (2010b). A classical-theory-based parameterization of heterogeneous ice nucleation by mineral dust, soot, and biological particles in a global climate model. *J. Atmos. Sci.* *67*, 2483–2503.
- Hoose, C. and O. Möhler (2012). Heterogeneous ice nucleation on atmospheric aerosols: A review of results from laboratory experiments. *Atmos. Chem. Phys. Discussions* *12*, 12531–12621.

- Intrieri, J. M., C. W. Fairall, M. D. Shupe, P. O. G. Persson, E. L. Andreas, P. S. Guest and R. E. Moritz (2002). An annual cycle of Arctic surface cloud forcing at SHEBA. *J. Geophys. Res.* *107(C10)*, 8039.
- Jayaweera, K. and P. Flanagan (1982). Investigations on biogenic ice nuclei in the Arctic atmosphere. *Geophys. Res. Lett.* *9*, 94–97.
- Jiang, H., W. R. Cotton, J. O. Pinto, J. A. Curry and M. J. Weissbluth (2000). Cloud resolving simulations of Arctic stratus observed during BASE: Sensitivity to concentration of ice crystals and large-scale heat and moisture advection. *J. Atmos. Sci.* *57*, 2105–2117.
- Kessler, E. (1969). On the distribution and continuity of water substance in the atmospheric circulations. *Meteorological Monographs* *10(32)*, 88 pp.
- Klein, S. A., R. B. McCoy, H. Morrison, A. S. Ackerman, A. Avramov, G. de Boer, M. Chen, J. N. S. Cole, A. D. Del Genio, M. Falk, M. J. Foster, A. Fridlind, J.-C. Golaz, T. Hashino, J. Y. Harrington, C. Hoose, M. F. Khairoutdinov, V. E. Larson, X. Liu, Y. Luo, G. M. McFarquhar, S. Menon, R. A. J. Neggers, S. Park, M. R. Poellot, J. M. Schmidt, I. Sednev, B. J. Shipway, M. D. Shupe, D. A. Spangenberg, Y. C. Sud, D. D. Turner, D. E. Veron, K. von Salzen, G. K. Walker, Z. Wang, A. B. Wolf, S. Xie, X.-M. Xu, F. Yang and G. Zhang (2009). Intercomparison of model simulations of mixed-phase clouds observed during the ARM Mixed-Phase Arctic Cloud Experiment. I: Single-layer cloud. *Q. J. Roy. Meteor. Soc.* *135*, 979–1002.
- Koop (2004). Homogeneous ice nucleation in water and aqueous solutions. *Z. Phys. Chem.* *218*, 1231–1258.
- Korolev, A. (2007). Limitations of the Wegener-Bergeron-Findeisen mechanism in the evolution of mixed-phase clouds. *J. Atmos. Sci.* *64*, 3372–3375.
- Korolev, A. V. and I. P. Mazin (2003). Supersaturation of water vapor in clouds. *J. Atmos. Sci.* *60*, 2957–2974.
- Kottmeier, C., J. Hartmann, C. Wamser, A. Bochert, C. Lüpkes, D. Freese and W. Cohrs (1994). Radiation and Eddy Flux Experiment 1993 (REFLEX II). *Berichte zur Polarforschung (Reports on Polar Research)*, Bremerhaven, Alfred Wegener Institute for Polar and Marine Research *133*, 62 p.
- Lindemann, J., H. A. Constantinidou, W. R. Barchet and C. D. Upper (1982). Plants as sources of airborne bacteria, including ice nucleation-active bacteria. *Appl. Env. Microbiol.* *44*, 1059–1063.
- Liu, X., S. Xie, J. Boyle, S. A. Klein, X. Shi, Z. Wang, W. Lin, S. J. Ghan, M. Earle, P. S. K. Liu and A. Zelenyuk (2011). Testing cloud microphysics parameterizations in NCAR CAM5 with ISDAC and M-PACE observations. *J. Geophys. Res.* *116*, D00T11.

- McFarquhar, G. M., S. Ghan, J. Verlinde, A. Korolev, J. W. Strapp, B. Schmid, J. M. Tomlinson, M. Wolde, S. D. Brooks, D. Cziczo, M. K. Dubey, J. Fan, C. Flynn, I. Gultepe, J. Hubbe, M. K. Gilles, A. Laskin, P. Lawson, W. R. Leaitch, P. Liu, X. Liu, D. Lubin, C. Mazzoleni, A.-M. Macdonald, R. C. Moffet, H. Morrison, M. Ovchinnikov, M. D. Shupe, D. D. Turner, S. Xie, A. Zelenyuk, K. Bae, M. Freer and A. Glen (2011). Indirect and semi-direct aerosol campaign. *Bull. Am. Meteor. Soc.* 92, 183–201.
- Meyers, M. P., P. J. DeMott and W. R. Cotton (1992). New primary ice-nucleation parameterizations in an explicit cloud model. *J. Appl. Meteorol.* 31, 708–721.
- Milbrandt, J. A. and M. K. Yau (2005). A multimoment bulk microphysics parameterization. Part II: A proposed three-moment closure and scheme description. *J. Atmos. Sci.* 62, 3065–3081.
- Möhler, O., D. G. Georgakopoulos, C. E. Morris, S. Benz, V. Ebert, S. Hunsmann, H. Saathoff, M. Schnaiter and R. Wagner (2008). Heterogeneous ice nucleation activity of bacteria: new laboratory experiments at simulated cloud conditions. *Biogeosciences* 5, 1425–1435.
- Morrison, H., J. A. Curry and V. I. Khvorostyanov (2005a). A new double-moment microphysics parameterization for application in cloud and climate models. Part I: Description. *J. Atmos. Sci.* 62, 1665–1677.
- Morrison, H., G. de Boer, G. Feingold, J. Harrington, M. D. Shupe and K. Sulia (2011a). Resilience of persistent Arctic mixed-phase clouds. *Nature Geosci.* 5, 11–17.
- Morrison, H., R. B. McCoy, S. A. Klein, S. Xie, Y. Luo, A. Avramov, M. Chen, J. N. S. Cole, M. Falk, M. J. Foster, A. D. Del Genio, J. Y. Harrington, C. Hoose, M. F. Khairoutdinov, V. E. Larson, X. Liu, G. M. McFarquhar, M. R. Poellot, K. von Salzen, B. J. Shipway, M. D. Shupe, Y. C. Sud, D. D. Turner, D. E. Veron, G. K. Walker, Z. Wang, A. B. Wolf, K.-M. Xu, F. Yang and G. Zhang (2009). Intercomparison of model simulations of mixed-phase clouds observed during the ARM Mixed-Phase Arctic Cloud Experiment. II: Multilayer cloud. *Q. J. Roy. Meteor. Soc.* 135, 1003–1019.
- Morrison, H. and J. O. Pinto (2005). Mesoscale modeling of springtime Arctic mixed-phase stratiform clouds using a new two-moment bulk microphysics scheme. *J. Atmos. Sci.* 62, 3683–3704.
- Morrison, H. and J. O. Pinto (2006). Intercomparison of bulk cloud microphysics schemes in mesoscale simulations of springtime Arctic mixed-phase stratiform clouds. *Mon. Weather Rev.* 134, 1880–1900.
- Morrison, H., J. O. Pinto, J. A. Curry and G. M. McFarquhar (2008). Sensitivity of modeled Arctic mixed-phase stratocumulus to cloud condensation and ice nuclei over regionally varying surface conditions. *J. Geophys. Res.* 113, D05203.
- Morrison, H., M. D. Shupe and J. A. Curry (2003). Modeling clouds observed at SHEBA using a bulk parameterization implemented into a single-column model. *J. Geophys. Res.* 108 (D8), 4255.

- Morrison, H., M. D. Shupe, J. O. Pinto and J. A. Curry (2005b). Possible roles of ice nucleation mode and ice nuclei depletion in the extended lifetime of Arctic mixed-phase clouds. *Geophys. Res. Lett.* 32, L18801.
- Morrison, H., P. Zuidema, A. S. Ackerman, A. Avramov, G. de Boer, J. Fan, A. M. Fridlind, T. Hashino, J. Y. Harrington, Y. Luo, M. Ovchinnikov and B. Shipway (2011b). Intercomparison of cloud model simulations of Arctic mixed-phase boundary layer clouds observed during SHEBA/FIRE-ACE. *J. Adv. Model. Earth Syst.* 3, M06003.
- Mossop, S. C., R. E. Ruskin and K. J. Heffernan (1968). Glaciation of a cumulus at approximately -4C. *J. Atmos. Sci.* 25, 889–899.
- Murray, B. J., D. O’Sullivan, J. D. Atkinson and M. E. Webb (2012). Ice nucleation by particles immersed in supercooled cloud droplets. *Chem. Soc. Rev.* 41, 6519–6554.
- Niedermeier, D., S. Hartmann, R. A. Shaw, D. Covert, T. F. Mentel, J. Schneider, L. Poulain, P. Reitz, C. Spindler, T. Clauss, A. Kiselev, E. Hallbauer, H. Wex, K. Mildenerger and F. Stratmann (2010). Heterogeneous freezing of droplets with immersed mineral dust particles - measurements and parameterization. *Atmos. Chem. Phys.* 10, 3601–3614.
- Niemand, M., O. Möhler, B. Vogel, H. Vogel, C. Hoose, P. Connolly, H. Klein, H. Bingemer, P. DeMott, J. Skrotzki and T. Leisner (2012). A particle-surface-area-based parameterization of immersion freezing on desert dust particles. *J. Atmos. Sci.* 69, 3077–3092.
- Ovchinnikov, M., A. S. Ackerman, A. Avramov, G. de Boer, A. M. Fridlind, J. Harrington, S. Ghan, A. Korolev, A. Lock, G. McFarquhar, H. Morrison and B. S. and Matt Shupe (2012). Arctic mixed-phase clouds: ISDAC flight 31. *ASR/GASS/8th International Cloud Modeling Workshop, ISDAC LES intercomparison* URL https://engineering.arm.gov/~mikhail/ISDAC_case_description.pdf.
- Ovchinnikov, M. and Y. L. Kogan (2000). An investigation of ice production mechanisms in small cumuliform clouds using a 3D model with explicit microphysics. Part I: Model description. *J. Atmos. Sci.* 57, 2989–3003.
- Ovchinnikov, M., A. Korolev and J. Fan (2011). Effects of ice number concentration on dynamics of a shallow mixed-phase stratiform cloud. *J. Geophys. Res.* 116, D00T06.
- Phillips, V. T. J., P. J. DeMott and C. Andronache (2008). An empirical parameterization of heterogeneous ice nucleation for multiple chemical species of aerosol. *J. Atmos. Sci.* 65, 9.
- Pinto, J. O. (1998). Autumnal mixed-phase cloudy boundary layers in the Arctic. *J. Atmos. Sci.* 55, 2016–2038.

- Prenni, A. J., J. Y. Harrington, M. Tjernström, P. J. DeMott, A. Avramov, C. N. Long, S. M. Kreidenweis, P. Q. Olsson and J. Verlinde (2007). Can ice-nucleating aerosols affect Arctic seasonal climate? *Bull. Am. Meteor. Soc.* 88, 541–550.
- Pruppacher (1995). A new look at homogeneous ice nucleation in supercooled water drops. *J. Atmos. Sci.* 52, 1924–1933.
- Pruppacher, H. R. and J. D. Klett (1997). *Microphysics of Clouds and Precipitation*. Atmospheric and Oceanographic Sciences Library. Kluwer Academic Publishers, Dordrecht, The Netherlands, 2nd ed.
- Randall, D., J. Curry, D. Battisti, G. Flato, R. Grumbine, S. Hakkinen, D. Martinson, R. Preller, J. Walsh and J. Weatherly (1998). Status of and outlook for large-scale modeling of atmosphere-ice-ocean interaction in the Arctic. *Bull. Am. Meteor. Soc.* 79, 197–219.
- Ritter, B. and J.-F. Geleyn (1992). A comprehensive radiation scheme for numerical weather prediction models with potential applications in climate simulations. *Mon. Weather Rev.* 120, 303–325.
- Rutledge, S. A. and P. V. Hobbs (1984). The mesoscale and microscale structure and organization of clouds and precipitation in mid latitude cyclones XII: A diagnostic modeling study of precipitation development in narrow cold-frontal rainbands. *J. Atmos. Sci.* 41.
- Schättler, U., G. Doms and C. Schraff (2009). A description of the nonhydrostatic regional COSMO-model. Part VII: User's guide URL <http://www.cosmo-model.org>.
- Seifert (2002). *Parametrisierung wolkenmikrophysikalischer Prozesse und Simulation konvektiver Mischwolken*. Ph.D. dissertation, faculty of physics at University of Karlsruhe (TH).
- Seifert, A. and K. D. Beheng (2006). A two-moment cloud microphysics parameterization for mixed-phase clouds. Part 1: Model description. *Meteorology and Atmospheric Physics* 92, 45–66.
- Seifert, A., A. Khain, A. Pokrovsky and K. D. Beheng (2006). A comparison of spectral bin and two-moment bulk mixed-phase cloud microphysics. *Atmos. Res.* 80, 46–66.
- Shantz, N. C., I. Gultepe, P. S. K. Liu, M. E. Earle and A. Zelenyuk (2012). Spatial and temporal variability of aerosol particles in Arctic spring. *Q. J. Roy. Meteor. Soc.* , 10.1002/qj.1940.
- Shaw, R. A., A. J. Durant and Y. Mi (2005). Heterogeneous surface crystallization observed in undercooled water. *J. Phys. Chem. B Lett.* 109, 9865–9868.
- Shupe and Intrieri (2004). Cloud radiative forcing of the Arctic surface: The influence of cloud properties, surface albedo, and solar zenith angle. *J. Clim.* 17, 616–628.
- Shupe, M. D. (2011). Clouds at Arctic atmospheric observatories. Part II: Thermodynamic phase characteristics. *J. Appl. Meteor. Clim.* 50, 645–661.

- Shupe, M. D., V. P. Walden, E. Eloranta, T. Uttal, J. R. Campbell, S. M. Starkweather and M. Shiobara (2011). Clouds at Arctic atmospheric observatories. Part I: Occurrence and macrophysical properties. *J. Appl. Meteor. Clim.* 50, 626–644.
- Solomon, A., M. D. Shupe, P. O. G. Persson and H. Morrison (2011). Moisture and dynamical interactions maintaining decoupled Arctic mixed-phase stratocumulus in the presence of a humidity inversion. *Atmos. Chem. Phys.* 11, 10127–10148.
- Stevens, B., C.-H. Moeng, A. S. Ackerman, C. S. Bretherton, A. Chlond, S. de Roode, J. Edwards, J.-C. Golaz, H. Jiang, M. Khairoutdinov, M. P. Kirkpatrick, D. C. Lewellen, A. Lock, F. Müller, D. E. Stevens, E. Whelan and P. Zhu (2005). Evaluation of large-eddy simulations via observations of nocturnal marine stratocumulus. *Mon. Weather Rev.* 133, 1443–1462.
- Sun, Z. and K. P. Shine (1994). Studies of the radiative properties of ice and mixed-phase clouds. *Q. J. Roy. Meteor. Soc.* 120, 111–137.
- Tao, X., J. E. Walsh and W. L. Chapman (1996). An assessment of global climate model simulations of Arctic air temperatures. *J. Clim.* 9, 1060–1076.
- Tsay, S.-C. and K. Jayaweera (1984). Physical characteristics of Arctic stratus clouds. *J. Clim. Appl. Meteorol.* 23, 584–596.
- Twohy, C. H., M. D. Petters, J. R. Snider, B. Stevens, W. Tahnk, M. Wetzel, L. Russell and F. Burnet (2005). Evaluation of the aerosol indirect effect in marine stratocumulus clouds: Droplet number, size, liquid water path, and radiative impact. *J. Geophys. Res.* 110, D08203.
- Uttal, T., J. A. Curry, M. G. McPhee, D. K. Perovich, R. E. Moritz, J. A. Maslanik, P. S. Guest, H. L. Stern, J. A. Moore, R. Turenne, A. Heiberg, M. C. Serreze, D. P. Wylie, O. G. Persson, C. A. Paulson, C. Halle, J. H. Morison, P. A. Wheeler, A. Makshtas, H. Welch, M. D. Shupe, J. M. Intrieri, K. Stamnes, R. W. Lindsey, R. Pinkel, W. S. Pegau, T. P. Stanton and T. C. Grenfeld (2002). Surface heat budget of the Arctic Ocean. *Bull. Am. Meteor. Soc.* 83, 255–275.
- Vali, G. (1971). Quantitative evaluation of experimental results on the heterogeneous freezing nucleation of supercooled liquids. *J. Atmos. Sci.* 28, 402–409.
- Vali, G. (1974). Contact ice nucleation by natural and artificial aerosols. *Conf. Cloud Physics, October 21-24, Tucson, Arizona, Amer. Meteor. Soc., Boston, Mass.* , 34–37.
- Vali, G. (1976). Contact-freezing nucleation measured by the DFC instrument. *Intl. Workshop on Ice Nucl. Meas. (G. Vali, Ed.), Univ. of Wyoming Report, Laramie* , 159–178.
- Vali, G. (1985). Nucleation terminology. *J. Aerosol Sci.* 16, 575–576.
- Vali, G. (1994). Freezing rate due to heterogeneous nucleation. *J. Atmos. Sci.* 51, 1843–1856.

- Vali, G. (1999). Ice nucleation – theory. *NCAR/ASP 1999 Summer Colloquium* URL http://www-das.uwyo.edu/~vali/nucl_th.pdf.
- Vali, G. and E. J. Stansbury (1966). Time-dependent characteristics of the heterogeneous nucleation of ice. *Can. J. Phys.* *44*, 477–502.
- Verlinde, J., J. Y. Harrington, G. M. McFarquhar, V. T. Yannuzzi, A. Avramov, S. Greenberg, N. Johnson, G. Zhang, M. R. Poellot, J. H. Mather, D. D. Turner, E. W. Eloranta, B. D. Zak, A. J. Prenni, J. S. Daniel, G. L. Kok, D. C. Tobin, R. Holz, K. Sassen, D. Spangenberg, P. Minnis, T. P. Tooman, M. D. Ivey, S. J. Richardson, C. P. Bahrman, M. Shupe, P. J. DeMott, A. J. Heymsfield and R. Schofield (2007). The Mixed-Phase Arctic Cloud Experiment. *Bull. Am. Meteor. Soc.* *88*, 205–221.
- Vogel, B., H. Vogel, D. Bäumer, M. Bangert, K. Lundgren, R. Rinke and T. Stanelle (2009). The comprehensive model system COSMO-ART – radiative impact of aerosol on the state of the atmosphere on the regional scale. *Atmos. Chem. Phys.* *9*, 8661–8680.
- Walsh, J. E., V. M. Kattsov, W. L. Chapman, V. Govorkova and T. Pavlova (2002). Comparison of Arctic climate simulations by uncoupled and coupled global models. *J. Clim.* *15*, 1429–1446.
- Wegener, A. (1911). *Thermodynamik der Atmosphäre*. Barth, Leipzig.
- Young, K. C. (1974). The role of contact nucleation in ice phase initiation in clouds. *J. Atmos. Sci.* *31*, 768–776.
- Zelenyuk, A., D. Imre, M. Earle, R. Easter, A. Korolev, R. Leaitch, P. Liu, A. M. Macdonald, M. Ovchinnikov and W. Strapp (2010). In situ characterization of cloud condensation nuclei, interstitial, and background particles using the single particle mass spectrometer SPLAT II. *Anal. Chem.* *82*, 7943–7951.
- Zobrist, B., T. Koop, B. P. Luo, C. Marcolli and T. Peter (2007). Heterogeneous ice nucleation rate coefficient of water droplets coated by a nonadecanol monolayer. *J. Phys. Chem. C* *111*, 2149–2155.
- Zuidema, P., B. Baker, Y. Han, J. Intrieri, J. Key, P. Lawson, S. Matrosov, M. Shupe, R. Stone and T. Uttal (2005). An Arctic springtime mixed-phase cloudy boundary layer observed during SHEBA. *J. Atmos. Sci.* *62*, 160–176.

Acknowledgments

First of all, I want to thank the referees, Prof. Dr. Corinna Hoose as well as Prof. Dr. Thomas Leisner - I did not regret to choose the proposed topic for my thesis.

The supervision of this work by Corinna Hoose is greatly appreciated. The dedication to the guidance during the last year was very motivating, which is also true for enabling me to attend the COSMO workshop and to travel to the International Cloud Modeling Workshop 2012 in Warsaw. In this context, the World Meteorological Organization is acknowledged for financial support.

An important contribution to this work originates from the group of Dr. Bernhard Vogel and Dr. Heike Vogel, providing the model which was used for this work. In particular, I want to thank Heike for her hints and additional parts of source code.

Thank you, Dr. Axel Seifert and Dr. Uli Blahak, for the helpful hints concerning the two-moment scheme. Furthermore, the comments by Dr. Mikhail Ovchinnikov on modeling issues are respected thankfully.

For their engagement with the correction of this thesis, I want to thank Jhony and Matthias.

For the supervision during my time as a student assistant, I want to thank Rayk, Bernhard, Heike and Corinna, permitting some insight in their topics of research.

Thanks, Mrs. Bolz, for providing support for any kind of organization.

Thanks to the AAF jogging group for reawakening my interest in running.

Thanks to the rest of the AAF crew for providing the exciting ambience of the institute.

Finally, I am much obliged to my parents for the support of any kind throughout my studies.

Erklärung

Ich versichere, dass ich die vorliegende Arbeit selbstständig verfasst und die verwendeten Hilfsmittel vollständig angegeben habe.

Ich erkläre mich damit einverstanden, dass diese Arbeit in die Bibliothek eingestellt wird und vervielfältigt werden darf.

Karlsruhe, im Januar 2013

Marco Paukert